REPUBLIC OF TÜRKİYE
YILDIZ TECHNICAL UNIVERSITY
GRADUATE SCHOOL OF SCIENCE AND ENGINEERING

PREPARATION OF METAL ORGANIC FRAMEWORK ADDED CONDUCTING POLYMER BASED MATERIALS AND THEIR SUPERCAPACITOR APPLICATIONS

Hilal YILDIRIM KALYON

DOCTOR OF PHILOSOPHY THESIS

Department of Metallurgical and Material Engineering

Material Engineering Program

Supervisor

Assoc. Prof. Dr. Metin GENÇTEN

Co-Supervisor

Assoc. Prof. Dr. Semih GÖRDÜK

July, 2024

REPUBLIC OF TÜRKİYE

YILDIZ TECHNICAL UNIVERSITY

GRADUATE SCHOOL OF SCIENCE AND ENGINEERING

PREPARATION OF METAL ORGANIC FRAMEWORK ADDED CONDUCTING POLYMER BASED MATERIALS AND THEIR SUPERCAPACITOR APPLICATIONS

A thesis submitted by Hilal YILDIRIM KALYON in partial fulfillment of the requirements for the degree of **DOCTOR OF PHILOSOPHY** is approved by the committee on 03.07.2024 in Department of Metallurgical and Material Engineering, Material Engineering Program.

Assoc. Prof. Dr. Metin GENÇTEN
Yildiz Technical University
Supervisor

Assoc. Prof. Dr. Semih GÖRDÜK
Yildiz Technical University
Co- supervisor

Approved By the Examining Committee

Assoc. Prof. Dr. Metin GENÇTEN, Supervisor
Yildiz Technical University _____

Prof. Dr. Hale BERBER, Member
Yildiz Technical University _____

Assist. Prof. Dr. Burak BİROL, Member
Yildiz Technical University _____

Prof. Dr. Nilgün KARATEPE YAVUZ, Member
Istanbul Technical University _____

Assoc. Prof. Dr. Gamzenur ÖZSİN, Member
Bilecik Şeyh Edebali University _____

I hereby declare that I have obtained the required legal permissions during data collection and exploitation procedures, that I have made the in-text citations and cited the references properly, that I haven't falsified and/or fabricated research data and results of the study and that I have abided by the principles of the scientific research and ethics during my Thesis Study under the title of "Preperation of Metal Organic Framework Added Conductıng Polymer Based Materıals and Theır Supercapacıtor Applications" supervised by my supervisor, Assoc. Prof. Dr. Metin GENÇTEN and my co-supervisor Assoc. Prof. Dr. Semih GÖRDÜK. In the case of a discovery of false statement, I am to acknowledge any legal consequence.

Hilal YILDIRIM KALYON

Signature

This work was supported by the Scientific and Technological Research Council of Turkey (TUBITAK) Scholarship: TÜBİTAK 2211-C National PhD Scholarship Program in the Priority Fields in Science and Technology (2211-C Öncelikli Alanlar Bursu 2021/2),

This work was supported by the Scientific and Technological Research Council of Turkey (TUBITAK) Scholarship: TÜBİTAK 2214-A - International Research Fellowship Programme PhD Students (2214-A Yurt Dışı Doktora Sırası Araştırma Burs Programı 2022/1),

This work was supported by the Higher Education Institution (YÖK) Scholarship:

YÖK 100/2000 Higher Priority Fields in the Energy Storage Critical Area (YÖK 100/2000 Enerji Depolama Öncelikli Alanlar Bursu),

This work was supported by Yildiz Technical University Scientific Research Council (BAP) under FBA-2021-4125 project code and FDK-2023-5233 Doctoral Project code.

Dedicated to my husband Metin
and Mirabelle.

ACKNOWLEDGEMENTS

Looking back, I am filled with deep gratitude for everyone who supported me throughout this journey.

First and foremost, to my supervisor, **Prof. Dr. Metin GENÇTEN**. He has been more than just a mentor—he has been a guide, a supporter, always encouraging me to dream bigger than I ever thought possible. From navigating complex research topics to celebrating our publications in top journals, his confidence in me never faltered. His support extended beyond the lab, offering me opportunities abroad where I explored exciting fields like lithium-ion batteries and electrophoretic deposition. His trust in my abilities, and his friendship has been a treasured part of this journey. For all, I am deeply and sincerely grateful.

To my co-supervisor, **Assoc. Prof. Dr. Semih GÖRDÜK**, whose expertise in chemistry and countless insightful discussions, often over coffee, made our research both enlightening and enjoyable. He made the complexities of our research feel accessible and fascinating; and his genuine friendship made our work together truly special. His guidance in MOFs has broadened my understanding and shaped this thesis in ways I couldn't have imagined. I have learned so much from him, and I am thankful for the bond we have built.

Yildiz Technical University was special because of the support and kindness of **Assit. Prof. Dr. Burak BİROL**. Thank you for making the lab a place of growth and for your guidance, which I will remember fondly. I am also grateful to **Assoc. Prof. Dr. Gamzenur ÖZSİN** for her expert assistance, which was crucial to my thesis progress. I deeply appreciate their involvement in my work.

To **Assoc. Prof. Dr. John Low** and my incredible colleagues at Warwick University—Dr. Barun, Dr. Gerard, Zelin, Benjamin, and others—thank you for making my research stay in the UK so fulfilling. Your support and collaboration made a significant impact on my work and my life during that time.

This work would not have been possible without the financial support of various institutions. I am sincerely thankful to the Scientific and Technological Research

Council of Turkey (TÜBİTAK) for the **TÜBİTAK 2211-C National PhD Scholarship Program in the Priority Fields in Science and Technology (2211-C Öncelikli Alanlar Bursu 2021/2)** and **TÜBİTAK 2214-A - International Research Fellowship Programme PhD Students (2214-A Yurt Dışı Doktora Sırası Araştırma Burs Programı 2022/1)** and the Higher Education Institution (YÖK) **YÖK 100/2000 Higher Priority Fields in the Energy Storage Critical Area (YÖK 100/2000 Enerji Depolama Öncelikli Alanlar Bursu)**, and Yildiz Technical University's Scientific Research Council (BAP) for their generous contributions and belief in my potential.

I also want to express my heartfelt thanks to my lab mates in the **Gençten Research Group**—Dr. Ayşe Vidat, Dr. Sezgin, Mohammad, Ziyad, Mustafa, Ozan, Aysu, and all my colleagues—for their support and for making the lab feel like a second home. Your friendship made even the toughest days enjoyable.

To my family, my parents and my special brother, thank you for your steadfast love and support, which has been the foundation of my success. You gave me the courage to pursue my dreams.

Finally, to my husband, Metin. Your love, patience, and constant encouragement, especially during our time apart in England, gave me the strength to continue. In these past few months, even as we faced our toughest days, you remained a guiding light and a source of encouragement. Your support has made each challenge easier to face. You've showed me the true meaning of how a strong family is built, and for that, I am endlessly grateful. Thanks for being my companion and for believing in me every step of the way.

To my luck Mirabelle, you have been a constant source of joy, reminding me daily of the simple, profound beauty of life. I am truly thankful for your presences in my journey.

Hilal YILDIRIM KALYON

TABLE OF CONTENTS

LIST OF SYMBOLS ıx

LIST OF ABBREVIATIONS x

LIST OF FIGURES xi

LIST OF TABLES xiv

ABSTRACT I

ÖZET xvii

1 INTRODUCTION 1

1.1 Energy Storage Systems 1

1.1.1 Batteries & Supercapacitors 2

1.1.2 EDLC, Pseudocapacitors, and Hybrid Capacitors 4

1.2 Electrode Material Design 5

1.2.1 Carbon Materials, Metal Oxides, and Conducting Polymers 6

1.2.2 Composites 11

1.3 Metal Organic Frameworks 12

1.3.1 History and General Information 13

1.3.2 Synthesis Methods and Applications 16

1.3.3 MOF5, HKUST1 and Post-Synthetic Modification 18

1.4 Electrochemical Three-Electrode System 20

1.4.1 Electrochemical Testing Methods and Elements 23

1.5 Scope of the Thesis 25

2 EXPERIMENTAL 26

2.1 Chemicals and Apparatus 26

2.2 Preparation of Metal Organic Frameworks 26

2.3 Fabrication of Electrodes 31

2.3.1 Electrochemical Cell Design 32

2.4 Characterization Methods 32

3 RESULTS AND DISCUSSION 34

3.1 Characterization of the Metal Organic Frameworks 34

3.1.1 Characterization of the M1, M2 and M3 Group 38

3.1.2 Characterization of the ED modified EM1, EM2, EM3 Group 51

3.1.3 Characterization of the M4, M5 and M6 Group 61

3.1.4 Characterization of the ED modified EM4, EM5, EM6 Group 73

3.2 Characterization of the Prepared Electrodes 80

3.2.1 Morphological Characterization of the Electrodes 80
3.2.2 Electrochemical Characterization of the Electrodes 98
3.3 Supercapacitor Application of the Electrodes 118
4 CONCLUSION **123**
REFERENCES **125**
PUBLICATIONS FROM THE THESIS **143**

LIST OF SYMBOLS

º	Degree
E	Energy Density
F	Farad
μ	Micro
mg	Miligram
mL	Mililiter
M	Molar
%	Percent
P	Power Density
S	Second
W	Watt

LIST OF ABBREVIATIONS

Ag/AgCl	Silver/ Silver Chloride
BDC	Benzenedicarboxylic Acid
BET	Surface Area Measurements by Brunauer-Emmett-Teller Study
BTC	Benzenetricarboxylic Acid
Co	Cobalt
Cu	Copper
CNT	Carbon Nano Tubes
CV	Cyclic Voltammetry
DTA	Differential Thermal Analysis
ED	Ethylenediamine
EDLC	Electrical Doluble Layer Capacitance
EIS	Electrochemical Impedance Spectroscopy
FT-IR	Fourier transform infrared spectrophotometry
GCDC	Galvanostatic Charge and Discrage Tests
HKUST – 1	Hong Kong University of Science and Technology - 1
IR-MOF	Iso Reticular MOF
IUPAC	International Union of Pure and Applied Chemistry
MOF – 5	Metal Organic Framework – 5
MOF	Metal Organic Framework
Pani	Polyaniline
PGE	Pencil Graphite Electrode
PPy	Polypyyrole
Pt	Platinum
P-XRD	Powder X-Ray Diffractometer
SEM-EDS	Scanning Electron Microscopy
TGA	Thermogravimetric Analysis
TPA	Terephtalic Acid
Zn	Zinc

LIST OF FIGURES

Figure 1.1. Ragone Graph containing different types of electrochemical energy storage devices 3

Figure 1.2. Comparison of galvanostatic charge-discharge processes for supercapacitors and battery devices 4

Figure 1.3. Structure of a EDLC supercapacitor 5

Figure 1.4. Some conductive polymers with conjugated structure 10

Figure 1.5. Conjugated double bond 10

Figure 1.6. Strategies to enhance the supercapacitor properties 11

Figure 1.7. Diverse assembly of building units 14

Figure 1.8. Hydrothermal synthesis of MOFs 16

Figure 1.9. Solvothermal synthesis of MOFs 17

Figure 1.10. Supercapacitor applications of MOFs 17

Figure 1.11. Electrochemical supercapacitor application of prepared electrodes 22

Figure 2.1. a) Metal Salt (Zinc Acetate, Zinc (II) Nitrate or Cobalt (II) Nitrate) mixing with terephtalic acid ligand (1-2 benzenedicarboxylic acid) and b) Metal Salt (Zinc Acetate, Cupper (II) Nitrate or Cobalt (II) Nitrate) mixing with trimesic acid ligand (1,3,5, Benzenetricarboxylic acid) with ethylenediamine addition into the dimethylformamide environments 27

Figure 2.2. ED was incorporated as a ligand on the MOF sites 28

Figure 2.3. a) Zn based MOF: With in situ ethylenediamine addition b) Co based MOF: The attachment of ED to the open metal sites of the water-stable, triazolate-bridged framework 29

Figure 2.4. Preparation of polypyrrole based electrodes 31

Figure 2.5. Used equivalent circuit model for fitting process of electrochemical impedance spectroscopy spectra and Gamry Interface 1010B Potenstiostat device 33

Figure 3.1. a) FTIR spectrum of the ligand terephtalic acid b) M1 c) M2 and d) M3 37

Figure 3.2. Thermal analysis of a) M1 b) M2 and c) M3 41

Figure 3.3. The XRD pattern of a) M1 b) M2 and c) M3 43

Figure 3.4. The SEM image of synthesized a) M1 b) M2 and c) M3 at 5000x magnification 44

Figure 3.5. FTIR spectrum of synthesized a) EM1 b) EM2 and c) EM3 49

Figure 3.6. Thermal analysis of synthesized a) EM1 b) EM2 and c) EM3 52

Figure 3.7. The XRD pattern of synthesized a) EM1 b) EM2 and c) EM3 54

Figure 3.8. The SEM images of synthesized a) EM1 b) EM2 and c) EM3 at 5000x magnification 56

Figure 3.9. The FTIR spectrum of ligand a)Trimesic Acid (BTC) b) M4 b) M5 and c) M6 60

Figure 3.10. The thermal analysis of synthesized a) M4 b) M5 and c) M6 63

Figure 3.11. The XRD pattern of synthesized a) M4 b) M5 and c) M6 65

Figure 3.12. The SEM image of synthesized a) M4 b) M5 and c) M6 at 10000x magnification 66

Figure 3.13. The FTIR spectrum of synthesized a) EM4 b) EM5 and c) EM6 71

Figure 3.14. The thermal analysis of synthesized a) EM4 b) EM5 and c) EM6) . 74

Figure 3.15. The XRD pattern of synthesized a) EM4 b) EM5 and c) EM6 76

Figure 3.16. The SEM image of synthesized a) EM4 b) EM5 and c) EM6 at 10000x magnification 79

Figure 3.17. The SEM image of electrode PPy/PGE from acid optimisation step: a) 0,05 M Acid PPy/PGE b) 0,1 M Acid PPy/PGE c) 0,2 M Acid PPy/PGE at 5000x magnification 81

Figure 3.18. The SEM image of electrode PPy/PGE from monomer optimisation step: a) 0,05 M Pyyrole PPy/PGE b) 0,5 M Pyyrole PPy/PGE c) 2 M Pyyrole PPy/PGE at 5000x magnification 83

Figure 3.19. The SEM image of electrode PPy/PGE from cycleoptimisation step: a) 5 cycle PPy/PGE b) 10 cycle PPy/PGE c) 30 cycle PPy/PGE d) 50 cycle PPy/PGE at 5000x magnification 84

Figure 3.20. The SEM image of the optimum electrode PPy/PGE at 10000x magnification 85

Figure 3.21. The SEM image of M1@PPY/PGEs consisting of a)3 mg , b)5 mg , c)10 mg and d) 20 mg M1 87

Figure 3.22. The SEM image of M2@PPY/PGEs consisting of a)3 mg , b)5 mg , c)10 mg and d) 20 mg M2 87

Figure 3.23. The SEM image of M3@PPY/PGEs consisting of a)3 mg , b)5 mg , c)10 mg and d) 20 mg M3 88

Figure 3.24. The SEM image of EM1@PPY/PGEs consisting of a)3 mg , b)5 mg , c)10 mg and d) 20 mg EM1 90

Figure 3.25. The SEM image of EM2@PPY/PGEs consisting of a)3 mg , b)5 mg , c)10 mg and d) 20 mg EM2 90

Figure 3.26. The SEM image of EM3@PPY/PGEs consisting of a)3 mg , b)5 mg , c)10 mg and d) 20 mg EM3 91

Figure 3.27. The SEM image of M4@PPY/PGEs consisting of a)3 mg , b)5 mg , c)10 mg and d) 20 mg M4 93

Figure 3.28. The SEM image of M5@PPY/PGEs consisting of a)3 mg , b)5 mg , c)10 mg and d) 20 mg M5 94

Figure 3.29. The SEM image of M6@PPY/PGEs consisting of a)3 mg , b)5 mg , c)10 mg and d) 20 mg M6.....94

Figure 3.30. The SEM image of EM4@PPY/PGEs consisting of a)3 mg , b)5 mg , c)10 mg and d) 20 mg EM4.....96

Figure 3.31. The SEM image of EM5@PPY/PGEs consisting of a)3 mg , b)5 mg , c)10 mg and d) 20 mg EM5.....97

Figure 3.32. The SEM image of EM6@PPY/PGEs consisting of a)3 mg , b)5 mg , c)10 mg and d) 20 mg EM6.....97

Figure 3.33. Production voltammogram of PPY/PGE.....99

Figure 3.34. a) Cyclic voltammograms and b) EIS spectrums of PPy/PGEs prepared in different concentration of pyrrole, c) cyclic voltammograms and d) EIS spectrums of PPy/PGEs prepared in different concentration of sulfuric acid, e) cyclic voltammograms and f) EIS spectrums of PPy/PGEs prepared over different cycles, and of PPy/PGEs prepared over different cycles.....101

Figure 3.35. Cyclic voltammograms and EIS spectrums of M1@PPy/PGE consisting different amounts of MOF compounds.....104

Figure 3.36. Cyclic voltammograms and EIS spectrums of M2@PPy/PGE consisting different amounts of MOF compounds.....105

Figure 3.37. Cyclic voltammograms and EIS spectrums of M3@PPy/PGE consisting different amounts of MOF compounds.....107

Figure 3.38. Cyclic voltammograms and EIS spectrums of EM1@PPy/PGE consisting different amounts of MOF compounds.....108

Figure 3.39. Cyclic voltammograms and EIS spectrums of EM2@PPy/PGE consisting different amounts of MOF compounds.....109

Figure 3.40. Cyclic voltammograms and EIS spectrums of EM3@PPy/PGE consisting different amounts of MOF compounds.....110

Figure 3.41. Cyclic voltammograms and EIS spectrums of M4@PPy/PGE consisting different amounts of MOF compounds.....112

Figure 3.42. Cyclic voltammograms and EIS spectrums of M5@PPy/PGE consisting different amounts of MOF compounds.....113

Figure 3.43. Cyclic voltammograms and EIS spectrums of M6@PPy/PGE consisting different amounts of MOF compounds.....114

Figure 3.44. Cyclic voltammograms and EIS spectrums of EM4@PPy/PGE consisting different amounts of MOF compounds.....116

Figure 3.45. Cyclic voltammograms and EIS spectrums of EM5@PPy/PGE consisting different amounts of MOF compounds.....117

Figure 3.46. Cyclic voltammograms and EIS spectrums of EM6@PPy/PGE consisting different amounts of MOF compounds.....118

Figure 3.47. Comparison of the areal capacitance of all synthesized MOF based electrodes for 1000 cycle.....120

LIST OF TABLES

Table 2.1 All Synthesized MOFs 30

Table 3.2. EDS analysis results of M1, M2 and M3 Group 45

Table 3.3. Theoretical calculated value of the M1, M2 and M3 Group 47

Table 3.4. BET Surface area results of the M1, M2 and M3 Group 50

Table 3.5. EDS analysis results of EM1, EM2 and EM3 Group 56

Table 3.6. Theoretical calculated value of the EM1, EM2 and EM3 Group 56

Table 3.7. BET Surface area results of the EM1, EM2 and EM3 Group 60

Table 3.8. EDS analysis results of the M4, M5 and M6 Group 67

Table 3.9. Theoretical calculated value of the M4, M5 and M6 Group 68

Table 3.10. BET Surface area results of the of the M4, M5 and M6 Group 72

Table 3.11. EDS analysis results of the EM4, EM5 and EM6 Group 79

Table 3.12. Rs, Rct, Cdl and Warburg impedance values of the electrodes prepared in the solution consisting different concentration of pyrrole and 0.1 M sulfuric acid 102

Table 3.13. Rs, Rct, Cdl and Warburg impedance values of the electrodes prepared in the solution consisting different concentration of sulfuric acid and 0.5 M pyrrole 102

Table 3.14. Rs, Rct, Cdl and Warburg impedance values of the electrodes prepared in the solution consisting of 0.5 M pyrrole and 1.0 M sulfuric acid over different voltammetric cycles 103

Table 3.15. GCD values comparison of all electrodes 121

ABSTRACT

Preparation of Metal Organic Framework Added Conducting Polymer Based Materials and Their Supercapacitor Applications

Hilal YILDIRIM KALYON

Department of Metallurgical and Material Engineering

Material Engineering Program

Doctor of Philosophy Thesis

Supervisor: Assoc. Prof. Dr. Metin GENÇTEN

Co- supervisor: Assoc. Prof. Dr. Semih GÖRDÜK

Materials obtained from Metal Organic Frameworks (MOFs) offer an important alternative to current methods for powering supercapacitors due to their high surface areas, large and adjustable pore volumes. Electrochemical composite formation of conductive polymers with metal organic frameworks has not been studied sufficiently in the literature. In addition, no binder is required by the electrochemical production of metal organic framework and carbon composite electrode material. For this purpose, within the scope of this thesis, metal organic frameworks were synthesized electrochemically together with conductive polymers on carbon materials; a new generation high-performance, high specific capacitance and high surface area composite supercapacitor electrode material was produced.

This Ph.D. thesis involved the individual synthesis of MOFs with various metal ions and ligands through chemical techniques, followed by their structural characterization using FT-IR, elemental analysis, P-XRD, BET study for surface

area measurements, and analysis of properties through SEM-EDS and TGA techniques. The electrochemically synthesized conducting polymer materials include MOFs which have been added through electrochemical processes, resulting in the creation of novel composite supercapacitor electrode materials. Analysis of these materials was conducted through spectroscopic techniques (FT-IR), microscopic techniques (SEM-EDS), and electrochemical techniques (CV, EIS, charge-discharge tests). M1@PPy/PGE and EM6@PPy/PGE are the best performers within their respective groups based on the provided data exhibits the highest capacitance of has the highest capacitance of 575.2 mF cm^{-2} and 570 mF cm^{-2} at 1 $mA.cm^{-2}$ charge/discharge current density, respectively.

Keywords: Metal organic frameworks, conducting polymers, energy storage, supercapacitors

ÖZET

Metal Organik Kafes Yapısı Katkılanmış İletken Polimer Esaslı Malzemelerin Üretimi ve Süperkapasitör Uygulamaları

Hilal YILDIRIM KALYON

Metalurji ve Malzeme Mühendisliği Bölümü

Malzeme Mühendisliği Programı

Doktora Tezi

Danışman: Doç. Dr. Metin GENÇTEN

Eş-Danışman: Doç. Dr. Semih GÖRDÜK

Metal-Organik Kafeslerden (MOF'lar) elde edilen malzemeler, yüksek yüzey alanları, geniş ve ayarlanabilir gözenek hacmi sayesinde süperkapasitörlere güç sağlamak için mevcut yöntemlere önemli bir alternatif sunar. İletken polimerlerin metal organik kafes ile elektrokimyasal kompozit oluşumu literatürde yeterince çalışılmamıştır. Ayrıca metal organik kafes ve karbon kompozit elektrot malzemesinin elektrokimyasal yöntemlerle üretilmesi ile herhangi bir bağlayıcıya ihtiyaç duyulmamaktadır. Bu amaçla bu tez kapsamında metal organik kafesler, karbon malzemeler üzerinde iletken polimerle birlikte elektrokimyasal yöntemle sentezlenerek; yeni nesil yüksek performanslı, yüksek özgül kapasitanslı ve yüksek yüzey alanına sahip bir kompozit süperkapasitör elektrot malzemesi üretilmiştir.

Bu doktora tezinde, farklı metal iyonları ve çeşitli ligandlar içeren MOF'lar kimyasal yöntemler kullanılarak ayrı ayrı sentezlenmiş, daha sonra bu bileşiklerin yapısal karakterizasyonu Fourier dönüşümü kızılötesi spektrofotometresi (FT-IR), element analizi, toz X-ışını difraktometresi (P-XRD), yüzey alanı ölçümleri BET

(Brunauer-Emmett-Teller) çalışması ile belirlenmiş ve taramalı electron mikroskobu (SEM-EDS) ile termogravimetrik analiz (TGA) teknikleri ile özellikleri analiz edilmiştir. Bu MOF'lar, aynı anda üretilen polimer malzemelere elektrokimyasal olarak dahil edilmiş ve yeni tip kompozit süperkapasitör elektrot malzemeleri üretilmiştir. Bu malzemelerin karakterizasyonu spektroskopik yöntemler (FT-IR), mikroskobik yöntemler (SEM-EDS) ve elektrokimyasal yöntemler (CV, EIS, şarj-deşarj testleri) kullanılarak gerçekleştirilmiştir. Sağlanan verilere göre kendi grupları içinde en iyi performansı gösterenler M1@PPy/PGE ve EM6@PPy/PGE olup sırasıyla at 1 mA.cm^{-2} şarj/deşarj akım yoğunluğunda 575,2 mF cm^{-2} ve 570 mF cm^{-2}'lik en yüksek kapasitansa sahiptir.

Anahtar Kelimeler: İletken polimerler, metal organik kafesler, enerji depolama, süperkapasitörler

1
INTRODUCTION

1.1 Energy Storage Systems

As technology develops, the complexity of human life increases, depending on the requirement for access to electricity and its storage [1]. Energy consumption is a key development plan worldwide because it generates economic activity [2]. The need for electrical power is becoming more crucial due to the growth of population and industrialization. Efficient energy storage systems from both renewable and non-renewable sources will meet this demand [3].

The modern life of humans heavily relies on critical energy storage devices primarily based on battery systems [4]. Since the industrial revolution, rapid technological developments and population growth have increased energy demand. In this globalizing world, environmentally friendly technologies are needed to reduce the environmental impacts of human activities [5]. Sustainable energy sources are being investigated to overcome the limited consumption provided by renewable energy sources.

The importance of energy storage systems has grown as the popularity of hybrid electric vehicles continues to rise. The need for efficient and sustainable energy storage systems is prompted by the exhaustion of fossil fuel resources and its negative impact on the environment. [6], [7]. To meet the rising demand for lightweight electronic devices, compact, lightweight, and high-performance energy storage systems are imperative. Cleaner and safer energy storage devices have become the research target to evolve the next-gen of electronics [8].

In the domain of energy storage; the pursuit of effective and sustainable solutions drives researchers to explore innovative materials poised to revolutionize energy storage devices [9].

1.1.1 Batteries & Supercapacitors

In today's world, energy storage relies heavily on battery systems, driven by the push for cleaner, sustainable energy sources. This push comes from both environmental concerns and technological advancements, which have led to decreased battery costs and increased reliance on renewable energy [5]. Consequently, there's a growing need for energy storage solutions that are efficient and environmentally friendly.

Traditional battery systems, however, have significant drawbacks, including short lifespans, slow charging times, and environmental hazards from their components [10], [11]. This has prompted a shift towards alternative energy storage technologies like supercapacitors, offering rapid charging, long cycle lives, and improved safety [12].

Supercapacitors bridge the gap between conventional capacitors and batteries, operating on electrostatic principles instead of chemical reactions [13]–[15]. While they have lower energy densities compared to batteries, ongoing research aims to enhance their capabilities to effectively meet diverse energy storage needs.

One crucial difference between supercapacitors and batteries lies in their charging and discharging mechanisms [11], [16]. Supercapacitors rely on the separation of charges at the electrode-electrolyte interface, allowing for quick energy transfer in short bursts. In contrast, batteries use reversible redox processes within their electrodes to chemically store energy, resulting in slower charge and discharge rates [17]–[19].

In the 21st century, where rapid charging is essential for electronic devices, electric vehicles, and critical military applications, supercapacitors emerge as promising candidates for high-performance energy storage [20]. By focusing on improving electrode materials and energy densities, researchers strive to unlock the full potential of supercapacitors in meeting the evolving demands of modern energy storage systems.

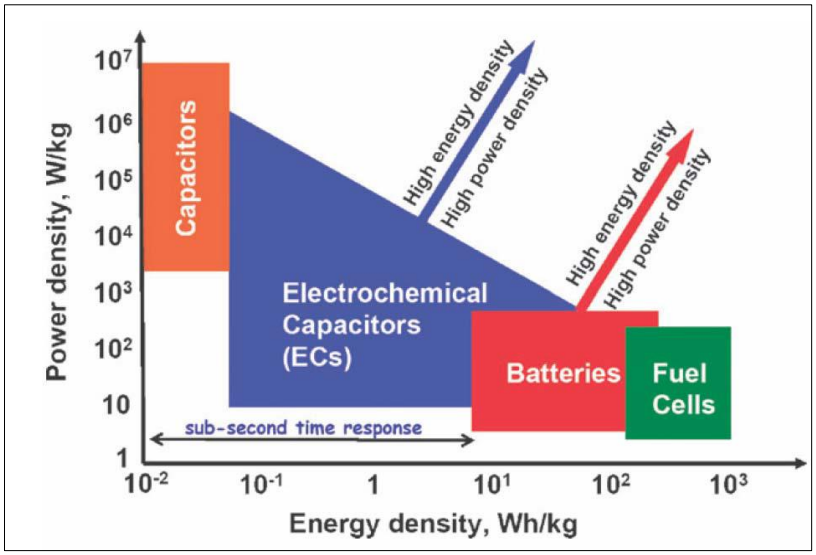


Figure 1.1. Ragone graph containing different types of electrochemical energy storage devices [15][21]

Figure 1.1 reveals that batteries and fuel cells can provide very high energy at a low power. In contrast, conventional capacitors, which exhibit high power due to the fast mobility of electrons in the conductive plates, are not capable of delivering high energy to meet long term applications [22]. Thus, it is clear that supercapacitors fill the gap in the ragone plot between the two types of devices mentioned. Supercapacitors provide a much higher power density than conventional batteries and fuel cells, while also exhibiting a higher energy density than conventional capacitors. Supercapacitors, which are unique with these features, additionally maintain their durability even with almost unlimited cycles [15], [23], [24].

Supercapacitors are an application where 2D materials can greatly improve performance and efficiency [25]. Due to electronic devices becoming miniature, the demand for tiny power supplies has risen, and supercapacitors made from 2D materials have fulfilled this need by offering high specific capacitances for small sizes and weights [26]–[28].

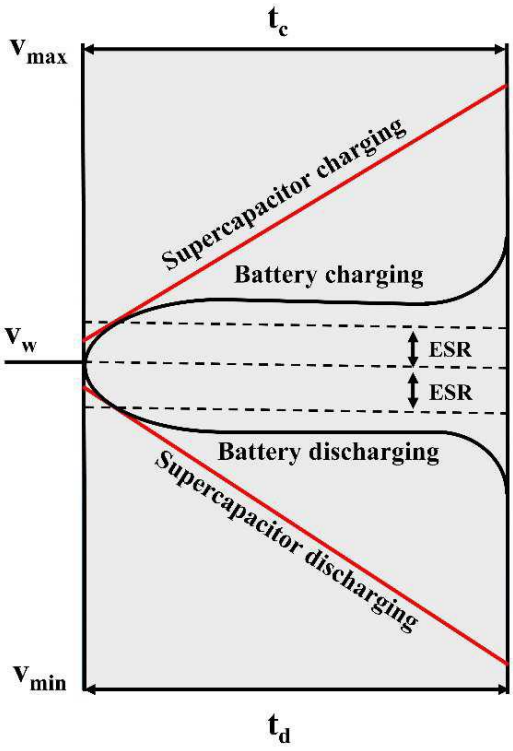


Figure 1.2. Comparison of galvanostatic charge-discharge processes for supercapacitors and battery devices [21]

Figure 1.2 shows a graph comparing the behavior of supercapacitors and batteries during charge and discharge times. When batteries are used to provide power, the voltage stays steady for an extended period of time, producing a flat profile during galvanostatic charge-discharge cycles. [29]. Conversely, when working with ideal supercapacitors, a linear change in voltage is seen during these processes.

1.1.2 EDLC, Pseudocapacitors, and Hybrid Capacitors

Manufacturers are urged to focus on supercapacitors capable of charging devices within seconds, ensuring safety and environmental friendliness while offering high performance and long cycle lives [30]. Supercapacitors, with their ability to discharge energy much faster than batteries, hold promise for load balancing and grid stabilization. They store energy on an electric double layer via ion adsorption, offering rapid charge and discharge properties without relying on the slower Faradaic process[31], [32].

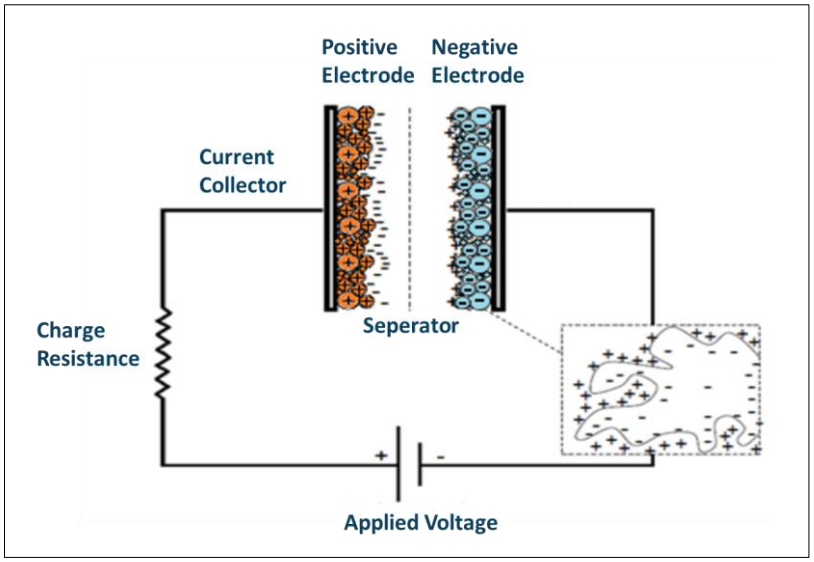


Figure 1.3. Structure of a EDLC supercapacitor [33]

Supercapacitors come in various designs, including electrochemical double-layer capacitors (EDLC) and pseudocapacitors, each with distinct mechanisms for storing electrical charge. EDLC, for instance, stores energy through carbon-based electrodes and an electrolytic liquid, while pseudocapacitors utilize redox chemical reactions at the electrode surface for storage as shown in **Fig.1.3.** [34]–[36]. Additionally, hybrid capacitors combine different electrode materials and energy storage methods, offering versatility in energy storage solutions.

Studies increasingly focus on electrode structural design as a crucial factor in supercapacitor performance, with various materials like metal oxides, conducting polymers, and carbon materials being explored [25]. Developing new electrode materials that balance high energy density and power density is essential for advancing supercapacitor technology and supporting their implementation.

1.2 Electrode Material Design

The performance and general advancement of supercapacitors are greatly influenced by electrode development. A supercapacitor's electrodes are in charge of storing and discharging electrical energy by allowing ions to collect and desorb on their surfaces. The quantity of charge that may be stored directly depends on the

surface area of the electrode [37], [38]. The electrode's capacitance is improved with increased surface area, increasing the amount of energy it can store. High porosity electrode materials, like carbon nanotubes or activated carbon, offer increased surface area and room for ions to gather, increasing capacitance [23].

To enable the quick flow of ions during both charging and discharging cycles, electrode materials must have high electrical conductivity. Enhancing the electrode materials' conductivity reduces internal resistance, allowing for more effective energy transmission and increased power density [24]. Carbon-based materials, like CNTs or 2D graphene, are commonly used for their excellent conductivity.

1.2.1 Carbon Materials, Metal Oxides, and Conducting Polymers

Electrodes should maintain their structural integrity and electrochemical performance over numerous charge and discharge cycles. Electrode materials must be stable in the electrolyte environment and resist degradation, such as physical changes, surface reactions, or electrolyte decomposition [22]. Researchers focus on developing electrode materials with enhanced stability to prolong the lifespan of supercapacitors. Reversible faradaic reactions can occur in electrode materials with redox-active species, like transition metal oxides or conducting polymers, allowing for extra charge storage above and beyond double-layer capacitance[39].

The energy density of supercapacitors can be considerably increased by creating electrode materials with high pseudocapacitance [40]. Advances in electrode materials may result in more effective and adaptable energy storage options, allowing supercapacitors to be widely used in a variety of applications.

Activated carbon possesses a heightened specific surface area, allowing for increased charge storage space and enhancing the device's overall capacitance. Activated carbon's low density is a major drawback that has restricted its use due to these unfavorable characteristics [35]. Co_3O_4, NiO, RuO_2, MnO_2, and V_2O_5 are the primary transition metal oxides under investigation for electrodes in pseudo-capacitors. The capacitance increases as metal oxides experience various oxidation states at specific potentials [41]. Those that are based on metal oxides, like RuO_2, are uncommon, whereas others suffer from their expansiveness [42]. To be developed, conductive polymer-based supercapacitors (such as polypyrrole,

polyaniline, and polystyrene) must possess a wide surface area and not exhibit any issues with their mechanical stability because it is a drawback of conducting polymers that limits their performance is the low power densities, which result from the sow ion diffusion rates within the material [43], [44]. Reduction and oxidation processes that occur during mechanical pressure this better electrode material's stability and charging and discharging cycles. By incorporating a metal oxide (like MOF) to increase the surface area and porosity, as well as by using a metal additive to raise the yield of the conductive polymer to an acceptable level, this issue can be minimised by forming a two-component compound [45], [46].

- **Conducting Mechanism of Conducting Polymers**

Polymers have traditionally been seen as good insulating materials and have found applications based on these insulating properties. However, many studies up to three decades ago showed that some classes of polymers exhibit semiconducting properties. Early studies revealed that polypyrroles show signs of conductivity. Shirakawa, MacDiarmid, and Heeger, who were awarded the Nobel Prize in Chemistry in 2000 for their discoveries on the conductivity properties of polyacetylene, made conductive polymers very popular in the field of science [47], [48].

Conductive polymers are polymers of organic nature that behave as a semiconductor or a conductor [29], [49]. These polymers are conjugated, that is, they have a structure that allows electron movement along the polymer chain, so they show unique optical and electrical properties. In **Figure 1.4** an example of known important conductive polymers is given [50]. Compared to other organic compounds, they have attracted great attention due to their good electrical conductivity, stability, easy and low-cost availability, redox properties, and they have found many applications as a result of their mechanical, magnetic and microwave absorbing properties [51].

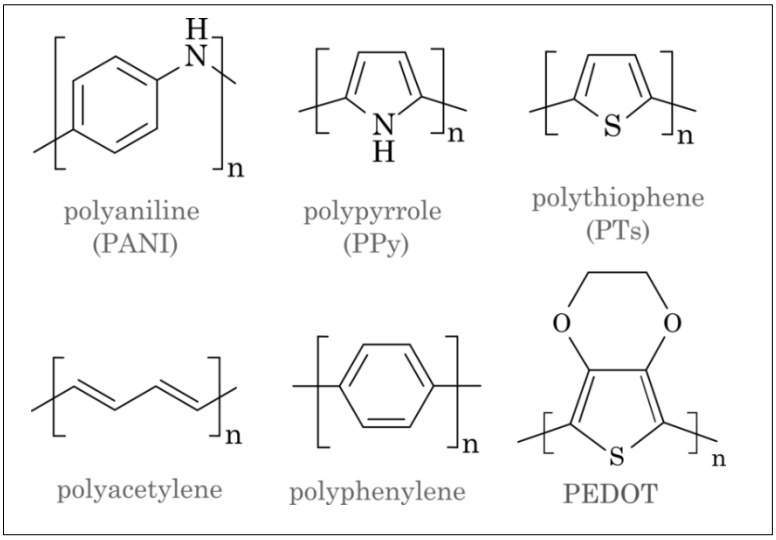


Figure 1.4. Some conductive polymers with conjugated structure [52]

There must be specific places inside the polymer lattice that allow electrons to go down the chain for polymers to display electrical conductivity (**Figure 1.5**) [53] This condition is met by polymers containing conjugated double bonds in the main chain.[54]



Figure 1.5. Conjugated double bond

While conducting polymers have many benefits as supercapacitor electrode materials, they also have certain drawbacks. Comparing conducting polymers with different electrode materials like activated carbon or transition metal oxides, they generally possess lower specific capacitance [55]. Because of this, they have a lower density of energy because they can store less charge per unit of mass or volume. They are less suited for purposes that need substantial energy storage because of this constraint [45].

During charge and discharge cycles, conducting polymers may experience poor stability during cycling [56]. The polymer structure may deteriorate with time and use, which will lower capacitance and overall performance. The polymer's expansion and contraction, variations in its oxidation state, or adverse interactions with the electrolyte can all contribute to its deterioration [57]. Comparative to some other electrode components, conducting polymers frequently have slower charge

and discharge rates. It is possible for the ionic and electronic mobility inside the polymer matrix to be restricted which will slow down the storage and release of energy [58]. Their utility in situations requiring a quick power supply may be constrained by this constraint. The decreased conductivity may result in more internal resistance and a lower power density, which would restrict the supercapacitor's overall performance [59], [60].

Scientists are exploring new approaches and strategies to address these limitations and enhance the performance of conducting polymer-based electrodes [61], [62]. By improving the specific capacitance, cycling stability, charge and discharge rates, conductivity, and environmental robustness, conducting polymers may become more competitive in supercapacitor applications in the future.

1.2.2 Composites

Conductive polymers have many advantages due to their easy synthesis, stability, reasonable price, high electrical conductivity, and doping characteristic. However, some properties of this substance limit the production of efficient products. Some of these disadvantages are poor solubility, mechanical properties, and poor reactivity [63]. To make the conductive polymers more soluble and easier to enter the reaction process, the conductive polymers are mixed with other chemical substances or conductive composites are synthesized from the reaction of commercial polymers with conductive polymers. These composite materials are used in energy storage, batteries, electronic devices manufacturing, heating elements, electricity distribution, conductive adhesive, corrosion inhibitor, fuel cells, sensor manufacturing [64], [65].

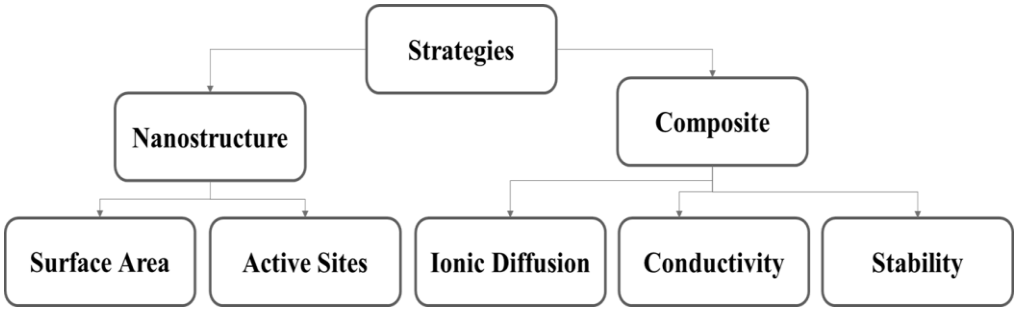


Figure 1.6. Strategies to enhance the supercapacitor properties [66]

This problem can be reduced by increasing the surface area and porosity by adding a MOF as well as by employing a metal additive to improve the yield of the conductive polymer to a suitable level, i.e., by creating a dual-component composite [62], [67]. Thus, it is proposed that supercapacitors can obtain a number of advantages and features by forming a conductive polymer composite in which the MOF is one of the primary constituents as shown in **Fig. 1.6.** [68]. This part exhibits improved porosity and surface area when made as a carbon composite based on MOFs. Furthermore, adding a metal additive greatly increases the system's efficiency [69]. To allow for this two-component mixture to exhibit remarkable properties.

1.3 Metal Organic Frameworks

In order to create polymer-based composites with excellent mechanical stability and enhance the charge journey as well as to improve the conductivity, specific capacity, and other electrochemical performance of Polypyrrole, various materials, including metal oxides, carbon nanotubes, zeolites, and metal organic frameworks (MOFs), have been incorporated into the polymeric matrix [70], [71]. MOF/PPy composites are utilized to apply for supercapacitors to solve the issue.

MOFs created by metal ions and an organic linker at the same time frequently have unique structural architectures [72]. Additionally, MOFs feature well-ordered, stable complex, high surface areas, and customized characteristics, which distinguish their composites for the creation of superior membranes. Conducting polymers are known for their electrical conductivity, while MOFs generally have low conductivity [73]. Incorporating conducting polymers into MOFs as a composite can improve the overall conductivity of the material. This enhanced conductivity allows for better electron transport throughout the electrode, reducing internal resistance and enabling faster charge and discharge rates [74]. The improved conductivity also helps mitigate the limitations associated with MOFs' poor electrical conductivity when used alone [62].

Accordingly, when the MOF is created as a conductive polymer composite, it is suggested that significant benefits and advantages can be obtained in the production

of supercapacitors due to the electrode being a crucial element [68]. When produced as a coordination polymer-based carbon composite, this part will possess an enhanced surface area and porosity. Furthermore, the system's effectiveness greatly improves with the addition of a metal. [71]. The composite design provides a framework for overcoming individual material limits and effectively enhancing the overall performance of supercapacitors by combining the benefits of MOFs with conducting polymers. The composite strategy is a promising way to advance supercapacitor technology since it has the potential to offer increased energy storage capacity, greater conductivity, structural stability, and customised features.

1.3.1 History and General Information

Werner found that coordination polymers can be created by using di- and tetratopic carboxylic acid linkers coordinated with di-, tri- or tetravalent metals [75]. he researchers studied the thermal stability of these polymers and linked it to the valence of the metal employed and the amount of potential coordination sites on the binder [76]. Following this, scientists imagined that numerous materials with endless 3D structures could be easily accessed, adjusted, and potentially beneficial **(Figure 1.7)** [77]. Yaghi created the term MOF a couple of years later by using hydrothermal synthesis to produce a 3D crystalline and transparent material [78]. Kitagawa [75] also studied the application of MOFs for storing methane. In 1999, MOF-5 became the first lattice structure to exhibit lasting porosity and structural stability after the guest solvent molecules were extracted from the Yaghi pores, as documented in the literature [79]. Soon after, Ferey utilized computational predictions and rational design to create a highly stable MOF with very large pores (30-34 Å) and a high surface area [72], [80]. Currently, the Cambridge Structural Database contains numerous MOF structures that have densities as low as 0.13 g/cm^3, up to 90% free pore volume, and a BET area exceeding 6000 m^2/g.

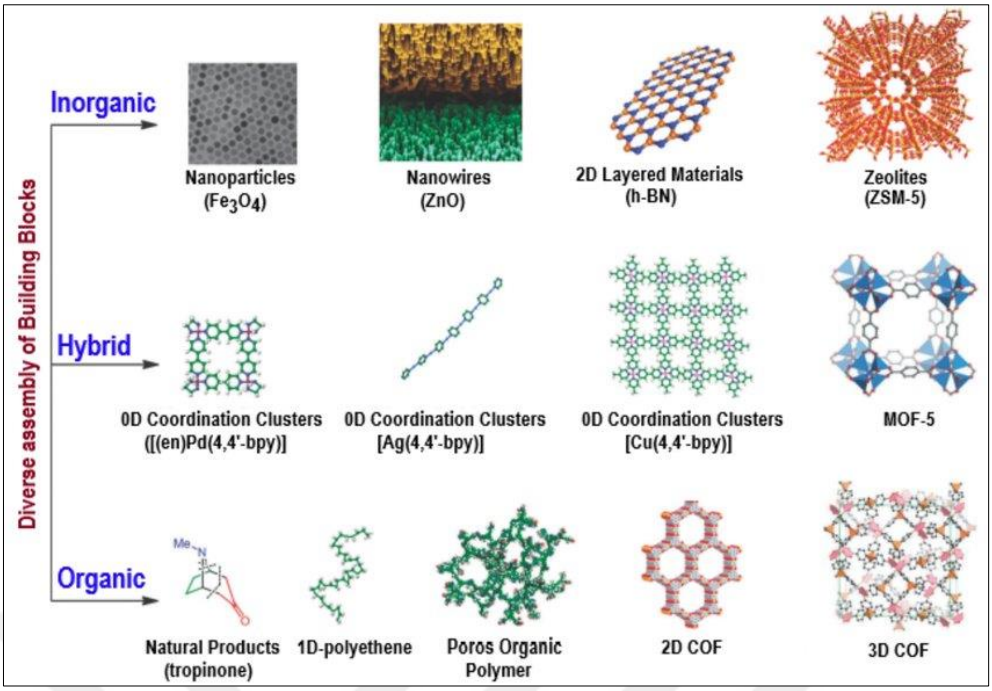


Figure 1.7. Diverse assembly of building units [81]

Metal organic frameworks containing metal or metal clusters and organic ligands can be obtained in different crystal structures [82]. Molecular crystals can form, consisting of coordinated groups around metals or metal clusters, associated with bonds such as hydrogen bonding and van der Waals forces [83]. In addition, one, two or three-dimensional crystal structures can be formed by the formation of covalent bonds between molecules, and such structures are defined as metal organic framework (MOF) structured compounds according to IUPAC. The term MOF, which was first used by Yaghi et al, has been used or rearranged by researchers. Reticulate MOF structures [84]. (IR-MOF; iso reticular MOF) can be expressed with additive for metal-modified Me-MOF (eg Pt loaded Pt-MOF) [85] and composites (e.g. CNT@MOF-5). Fe(II), Cu(II) and Zn(II) compounds [86] with MOF structure are widely used in applications such as catalyst, gas storage, gas purification [87].

Metal organic frameworks, referred to as porous organic-inorganic hybrid coordination polymers, belong to a family of crystalline and organized materials with distinct porosity [88]. These substances combine elements from the frequently distinct fields of organic and inorganic chemistry, and they do so by using appropriate organic ligands to connect metal ion clusters [89]. This well-coordinated structure leads to the creation of a highly porous material with one of

the largest surface areas among all known materials, offering advantages in terms of versatility and structural manipulation. Many MOFs have been created, providing a diverse selection of architectures and adjustable porosities [72], [90], [91]. The focus on moving MOF particles to higher dimensions has become more prevalent recently, such as by applying MOFs onto moldable and chemically resistant materials like polymers [92], [93]. The electrolyte ions can quickly interface with MOF particles owing to the rapid growth of MOFs and their notable electrochemical characteristics throughout diffusion. Additionally, it is clear that electrolytes can move freely through pores [94]. MOFs have a high electrochemical double-layer capacitance (EDLC) value as a result of these phenomena. Its ion-exchange properties have drawn a lot of attention in relation to the absorption of different cationic and anionic species. Moreover, open metal patches, or unsaturated metal centres, are known to function as Lewis acids that strongly polarise organic solvents.[95]. The characteristics of MOFs can be improved by either adding functional groups to metal complexes or ligands after synthesis, or by utilizing precursors in the design and synthesis process. [96].

There has been a growing interest in using metal organic frameworks (MOFs) as possible materials for supercapacitor electrodes. MOFs, which are a type of porous materials, consist of metal ions and organic ligands. MOFs may have extremely large surface areas because of their porous structure.; and this feature offers a spacious contact area for electrolyte ions, enabling effective charge storage [97]. It is possible to create MOFs with precise manipulation of pore dimensions, structure, and properties [98]. This ability to be adjusted allows for the creation of MOFs with better pore structures for ion diffusion and increased capacitance. Certain metal organic frameworks display redox capability, enabling them to retain charge via double-layer capacitance and faradaic mechanisms [99]. This extra pseudocapacitance has the potential to increase the overall energy storage capability [100]. MOFs provide a variety of options for combining metals and ligands, allowing for flexibility in creating materials with specific characteristics. This adaptability enables customization according to specific needs, like cycling stability, conductivity, or ion selectivity. The majority of MOFs exhibit insulating properties or low electrical conductivity, which can limit their effectiveness as electrode materials [62]. Improving the conductivity of MOFs is a crucial obstacle

for their effective use. Creating MOFs can be challenging and often involves complex procedures [68]. The aim of ongoing research is to raise production of MOF at a low cost while maintaining its appealing characteristics.

1.3.2 Synthesis Methods and Applications

The synthesis of MOFs can be difficult and frequently includes complicated steps. The goal of continuing research is to increase MOF manufacturing at an affordable cost while preserving its attractive features [101]. It has been determined that compounds with MOF structure can be synthesized by different methods in the literature. While the solvothermal synthesis methods based on the dissolution of the starting materials at room temperature and different temperatures, which are mostly carried out under normal conditions, are preferred, electrochemical, ionothermal, hydrothermal, mechanochemical synthesis methods are also preferred by the researchers [85], [88], [102]

In the room temperature synthesis method, the organic ligands that bind the metal complexes together and the substances containing the metal ion are dissolved in separate solvents, and the metal complex solution is slowly added onto the organic solution [103], [104]. The mixture is stirred for a while and a precipitate is dried, washed and the substance is obtained as represented in **Figure 1.8.**



Figure 1.8. Hydrothermal synthesis of MOFs [104]

Hydrothermal synthesis method, in which solution-phase reactions are carried out in closed pressure reactors (autoclaves) at high pressure and high temperature, is widely used especially in the synthesis of polymeric structures [105], [106]. In this method, the synthesis is generally carried out at a temperature above the boiling point of the solvent phase and under the vapor pressure at this temperature, with and/or without stirring **(Figure 1.9)**.



Figure 1.9. Solvothermal synthesis of MOFs [106]

MOFs show great potential as electrode materials in electrochemical energy storage devices because of their shape, functional binders, large specific surface area, and metal sites. It is also anticipated that MOF structures contribute to the formation of an improved electrode material when combined with carbon materials [107].

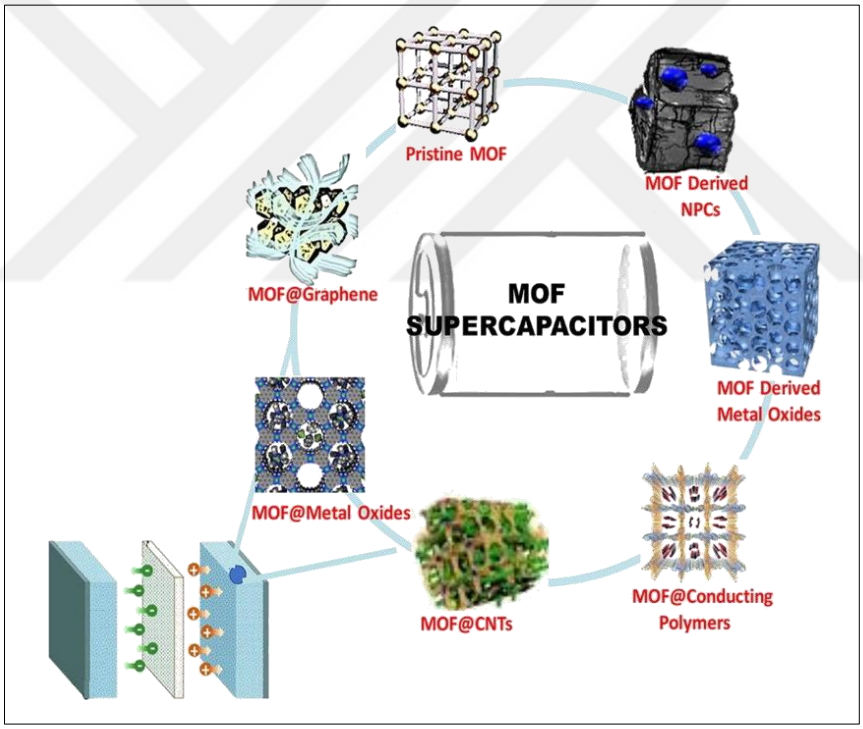


Figure 1.10. Supercapacitor applications of MOFs [71]

In addition, as can be seen in **Figure 1.10**, with the production of MOF@Carbon composite electrode by electrochemical methods, no binder is required. In this way, an electrode material with high performance, high specific capacitance, and high surface area is produced [71].

1.3.3 MOF5, HKUST1 and Post-Synthetic Modification

MOF-5 is composed of zinc oxide (Zn_4O) clusters connected by benzene-1,4-dicarboxylate (BDC) organic linkers. MOF-5 has a three-dimensional porous structure with regular hexagonal channels [85], [98]. Its framework forms a diamond-like topology, with ZnO clusters at the corners of the diamond and BDC linkers connecting them. MOF-5 exhibits a high surface area and large pore volume, making it suitable for gas storage and separation applications. Its pore size can be tuned by adjusting the length of the organic linkers [108], [109].

HKUST-1 is composed of copper (Cu) ions coordinated with 1,3,5-benzenetricarboxylate (BTC) organic linkers. HKUST-1 has a three-dimensional structure with a cubic topology [62], [110]. The Cu ions are connected by BTC linkers, forming paddlewheel units. These paddlewheel units are further linked to form a porous framework. HKUST-1 exhibits a high surface area and tunable pore size [111]. Its unique structure allows for the presence of open metal sites (Cu sites), which can interact with guest molecules or ions [99].

With their distinct characteristics, high porosity, and prospective uses in gas storage and separation, MOF-5 and HKUST-1 have both attracted a lot of interest. These MOFs have been closely studied throughout scientific areas, including catalysis and energy storage [112]. They are interesting materials for a variety of scientific and technological fields because of the customizable structures and porosity, which enables customisation and optimisation for particular purposes [62].

Modifications to the framework have a significant impact on how well MOFs perform in comparison to unmodified MOFs [113]. Amines can alter MOF structures to enhance their resistance to oxidation from outside substances such as water [108]. Although alkyl groups, like the ethylene bridge in ethylenediamine, may contribute to the MOF structure hydrophobia, which decreases the absorption of water, the fundamental nature of the unbound amine groups bonding onto the free-standing metal spots strengthens the Framework stability [100], [114]. For instance, the MOF architecture can be preserved via impregnation, which encapsulates active species inside the MOF pores.

Direct one-pot synthesis is the primary method for producing amino-functionalized MOFs. In this method, amine-containing ligands are employed as organic linkers

to coordinate metal ions to create crystalline MOF structures, or post-synthetic methods that covalently adjust a bridging ligand onto a coordinatively unsaturated metal center.

Ethylenediamine (ED) is a coordination agent that contains two amine binding sites [115]. Compounds with ED functionality has been employed extensively in water and gas pollutant removal, among other purposes. In a number of experiments, the lower molecular weight functionalizing ligand ethylenediamine, which has terminal amino groups and a tiny kinetic width and can engage with open metal sites, was employed [116]. The amine of a diamine compound can either stay open as a chemically reactive adsorption site or can attach to a metal cation as a Lewis base in highly strong metal organic frameworks including well-separated open metal spots [117]. Meanwhile, the diamine is integrated as a co-ligand into the MOF cation sites that can be reachable on the framework pores' interface. Since the diamines appeared smaller than the gap between two neighbouring metal positions, it was suggested that amine was permitted to interact with guest molecules after framework engagement [118], [119]

Ethylenediamine or additional functional groups are occasionally added to metal organic frameworks to improve their characteristics for use in storage of energy. According to the specific objectives of the usage, the modification using ED fulfills a variety of functions. ED modification can introduce amine functionalities into the MOF structure. Some MOFs modified with ED can exhibit redox activity, contributing to their pseudocapacitive behavior [100]. The redox-active ED groups within the MOF structure can undergo reversible redox reactions, enabling additional charge storage beyond the typical double-layer capacitance [117]. This pseudocapacitance can enhance the overall energy storage capacity of the MOF-based electrode. It is important to note that the specific modification of MOFs with ED depends on the targeted application and desired properties. It is still difficult to achieve cycling stability for ED-MOFs used as electrode materials in energy storage systems. When MOFs undergo repeated charge-discharge cycles, their structural integrity may deteriorate and reorganize, resulting in decreased performance and capacity loss. Further research is required to determine the best ways to increase the stability and toughness of ED-MOFs for long-term energy storage applications. Despite these difficulties, ED-MOFs and their potential use in energy storage

devices are still being researched [113], [120]. To improve the performance of ED-MOF-based electrodes, researchers are looking into novel strategies including hybrid composites with conducting polymers or other electrochemically active materials. ED-MOFs could be used as energy storage materials by addressing conductivity difficulties, enhancing cycling stability, and optimizing electrode design [68]. Both MOF-5 and HKUST-1 have been modified with ethylenediamine in various studies to introduce specific functionalities or enhance their properties for different applications. In certain studies, MOF-5 has been modified by incorporating ED molecules during the synthesis process. ED can be introduced as additional ligands, replacing some of the original benzene-1,4-dicarboxylate (BDC) linkers in MOF-5 [116], [121]. The incorporation of ED can introduce amine functionalities into MOF-5, allowing for interactions with specific molecules or ions. HKUST-1 has also been modified with ED through post-synthetic routes or in situ synthesis methods. ED molecules can be introduced onto the copper ions or as additional ligands in the HKUST-1 framework. The incorporation of ED can introduce amine functionalities to HKUST-1, providing additional interaction sites for target molecules or ions [122]. The modification of MOFs with ED aims to enhance the electrochemical performance and energy storage capabilities of the electrodes. ED-modified MOFs have been combined with conducting polymers or carbon materials to form composite electrodes for supercapacitors [108], [116], [123] The ED-modified MOFs can provide additional capacitance through redox pseudocapacitive behavior, while the conducting polymers or carbon materials improve the electrical conductivity and mechanical stability of the electrode [113].

1.4 Electrochemical Three-Electrode System

Supercapacitor electrode manufacture and characterization frequently use the electrochemical three-electrode system. It enables the effectiveness of the electrode materials to be tested and evaluated electrochemically. A working electrode, a counter electrode, and a reference electrode comprise the system's three primary parts as illustrated in **Fig. 1.11.** [124]. Usually, the material under examination for supercapacitor electrodes serves as the working electrode. During the supercapacitor's operation, it controls electrochemical processes and charge storage

[125]. The process of making the working electrode usually involves depositing or constructing the electrode material onto a conductor substrate [126]. The working electrode in a three-electrode system is connected to the potentiostat's positive port, which regulates the potential that is applied and records the electrochemical output [127]. The counter electrode serves as the counterpart to the working electrode. It provides a conducting surface for the electrical current to flow and completes the circuit in the electrochemical cell. The counter electrode is typically made of a conductive material, such as platinum (Pt) or stainless steel, that does not undergo significant electrochemical reactions during the experiments [128]. It is connected to the negative terminal of the potentiostat and maintains a constant potential with respect to the reference electrode. The reference electrode is used as a reference point to measure and control the potential of the working electrode. It consists of a stable electrode with a well-defined and known potential, allowing for accurate potential measurements. Commonly used reference electrode is the silver/silver chloride electrode (Ag/AgCl) [129]. The reference electrode is connected to the reference terminal of the potentiostat, which helps maintain a constant potential difference between the working and reference electrodes. The three-electrode system allows precise control of the potential applied to the working electrode and accurate measurement of the resulting current [130]. This setup enables the determination of key electrochemical properties of supercapacitor electrodes, such as capacitance, charge/discharge rates, cycling stability, and electrochemical behavior. By applying different potential waveforms and measuring the resulting current response, researchers can obtain data on the electrochemical performance of the supercapacitor electrodes. These measurements help in assessing the energy storage capacity, power density, and overall efficiency of the electrode materials, aiding in the optimization and development of high-performance supercapacitors [131]. It is a cost-effective method compared to coin cell production, which involves more complex assembly and requires larger quantities of materials. Once optimized, the electrode materials identified using the three-electrode system can be further scaled up for coin cell or larger-scale supercapacitor fabrication[132].

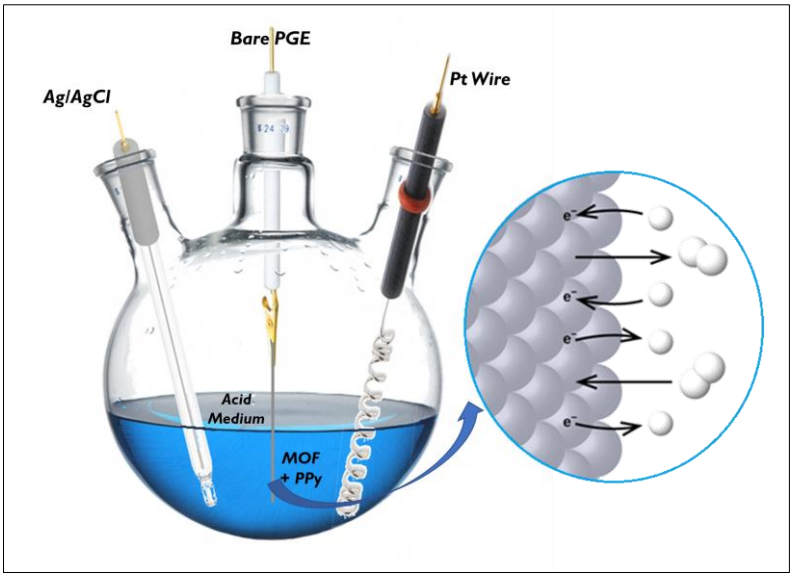


Figure 1.11. Electrochemical supercapacitor application of prepared electrodes

Pencil graphite electrodes are easily obtained, inexpensive, and conveniently reachable. They can be sourced from standard graphite pencils, providing a budget-friendly choice for making and testing electrodes. Graphite is an incredibly conductive substance, enabling effective transfer of charge in electrochemical reactions [56], [128], [133]. Pencil graphite electrodes (PGEs) show excellent electrical conductivity, a key factor for creating top-performing supercapacitors.

The process of creating supercapacitor electrodes on a PGE without the need for a binder material is known as binder-free synthesis. Usually, polymer binders are employed to bind the active electrode material and enhance its attachment to the current collector. Nevertheless, in the synthesis process without using a binder, the active substance is directly coated onto the graphite electrode [134].

Porous structures in PGEs enable close interaction with the active electrode material [135]. When the active substance is applied directly onto the graphite electrode surface, it can seep into the pores of the graphite and create a strong connection. This close contact improves the electrical conductivity and the speed of charge transfer at the interface between the electrode and electrolyte. The active substance sticks to the graphite surface by means of mechanical locking. When the active material is pressed against the graphite electrode, it is able to penetrate the uneven surface of the graphite and establish interconnected links [73]. This mechanical interlocking enhances stability and retains the electrode's integrity during electrochemical cycling. Van der Waals forces are involved in attaching the active

substance to the graphite electrode. Van der Waals forces are low-strength intermolecular forces that result from the interactions between electron clouds of neighboring molecules. These forces help stick the active material particles to the graphite surface, making sure they are firmly attached. The graphite electrode serves as a conductive base, creating routes for electron movement across the substrate. Because the active material is directly touching the graphite surface, it can take advantage of graphite's high electrical conductivity to help with efficient transportation of electrons while charging and discharging [136].

The synthesis and testing of materials using an electrochemical three-electrode system with a pencil graphite electrode involves preparing the material of interest, such as modified metal organic frameworks (MOFs), conducting polymers, or composite materials. This process aims to tailor the material's structure, composition, and surface properties for optimal electrochemical performance in energy storage devices like supercapacitors. Synthesis ensures controlled fabrication conditions to achieve reproducibility and consistency in material properties. It involves various methods such as electrodeposition, chemical modification, or surface functionalization to impart specific characteristics to the material [87]. The three-electrode system allows for comprehensive electrochemical characterization of the synthesized materials [68]. This system enables the evaluation of key parameters such as specific capacitance, charge-discharge kinetics, cyclic stability, and impedance characteristics. These measurements provide insights into the material's electrochemical behavior and suitability for energy storage applications.

1.4.1 Electrochemical Testing Methods and Elements

Various electrochemical testing techniques are frequently employed to investigate the performance of supercapacitor electrode materials. These techniques offer important information on the electrochemical behavior, mechanisms of charge storage, and energy storage potential of the electrodes.

- Voltammetry is the name given to a group of electroanalytical methods in which information about the analyte is obtained by utilizing the measurement of current as a function of applied voltage under conditions where an indicator or working electrode is polarized. In cyclic voltammetry,

the applied voltage is scanned at a certain range starting from a point and returns to the starting point again [137]. Meanwhile, the current formed as the applied voltage is measured and recorded. The variation of the voltage used with time is usually triangular. How long this time will be depending on the scanning speed being worked. With the cyclic voltammetry method, many important data can be obtained about the reaction occurring on the electrode surface. It is among the information that can be reached with the obtained voltammograms that the reaction is fully reversible, semi-reversible and irreversible [138]. Again, the number of electrons transferred during an oxidation-reduction reaction can also be determined by the analysis of the voltammograms obtained in the relevant method. CV is a commonly employed method for studying the redox performance and capacitance characteristics of supercapacitor electrodes. During CV, an electrode is subjected to a voltage while the resulting current response is measured. The voltage is cyclically varied between two limits, usually at a set scan rate. A CV gives details on the electrode material's electrochemical activity, redox reactions, and capacitive properties. It produces the voltammogram, showing the current in relation to the applied voltage.

- Electrochemical impedance spectroscopy, also known as AC impedance, is a widely used method today, from measuring double layer capacitance to determining many processes and examining complex surfaces. The basis of the method is based on the principle of measuring the response corresponding to a small amplitude AC signal applied to the system[139]. The analysis performed by measuring the amphitheater AC signal applied over a wide range is called electrochemical impedance spectroscopy. The obtained results give information about the interfaces, the structures of these surfaces and the reactions that take place there. EIS is a strong tool for studying the electrical characteristics and impedance patterns of supercapacitor electrodes [140]. EIS entails administering a slight sinusoidal voltage disturbance to the electrode as the corresponding current reaction is measured at various frequencies. EIS offers details about resistive, capacitive, and diffusion processes at the electrode-electrolyte interface through impedance spectra analysis. Assisting in assessing the

electrode's charge transfer kinetics, ion diffusion, and interfacial behavior is important.

- Galvanostatic Charge-Discharge (GCDC) is a method employed to assess the charge storage and discharge properties of supercapacitor electrodes. In the cyclic charge-discharge method, a sequential charge and discharge applied to the developed secondary battery system is defined as a single cycle [110]. In this method, together with the charges and discharges applied to the battery, the cycle life of the system, the discharge capacity and its performance in this process can be determined [141]. During cyclic charge-discharge tests for supercapacitors based on metal organic frameworks, various factors are typically considered. These criteria assist in assessing the storage efficiency of energy, as well as the charging and discharging patterns, and the long-term stability of the electrodes made from MOFs.

Noting that the parameters for cyclic charge-discharge tests may differ based on the MOF material, electrode setup, electrolyte system, and performance goals is crucial. Selecting the best parameters for MOF-based supercapacitors usually requires systematically optimizing and comparing various conditions to attain the desired electrochemical performance and cycling stability.

1.5 Scope of the Thesis

The high concentration of unsaturated metal centers and circular pore geometry of the MOF class provide easily accessible specific binding spots. Our main goal is to assess how well these composites perform as electrodes for energy storage applications by taking advantage of the large internal surface area of MOFs to support the widely used pseudocapacitive polymer, Polypyyrole.

To achieve this goal, diverse metal ions and various ligands were incorporated into MOFs through chemical processes, followed by structural characterization using FT-IR, elemental analysis, P-XRD, BET surface area measurements, and analysis of properties using SEM-EDS and TG-DTA techniques. The MOFs were added to the polymer materials through an electrochemical process, resulting in the creation of novel composite supercapacitor electrode materials. These materials were characterized using microscopic (SEM), and electrochemical (CV, EIS, galvanostatic charge-discharge tests) methods.

2
EXPERIMENTAL

2.1 Chemicals and Apparatus

Sigma-Aldrich provided pyrrole, sulfuric acid, 1,4-benzene dicarboxylic acid (terephthalic acid) ligand, 1,2-benzenedicarboxylic acid (phthalic acid) ligand and 1,3,5- benzene tricarboxylic acid (trimesic acid) ligand, zinc(II) acetate, and copper (II)nitrate and cobalt(III) nitrate. Merck was the source for ethylenediamine (≥99%) and N,N-dimethylformamide (≥99%). The deionized double-distilled water was purified using 18 $M\Omega cm^{-1}$ ultrapure water from aMillipore Milli-Q Direct 16.

The experiment utilized glass cells with five necks. Graphite from a pencil was utilized as the working electrode. Ag/AgCl (in 3.0 M KCl) along with a platinium wire were utilized as reference and counter electrodes, respectively. Pieces of pencil leads (Tombow, HB, D: 0.5 mm) measuring 3 cm were cut and 0.5 cm of each piece (with a surface area of 0.1 cm^2) was submerged in the solution. All electrochemical experiments were conducted using the Gamry 1010B Potentiostat/ Galvanostat.

2.2 Preparation of Metal Organic Frameworks

Various MOFs were prepared individually following the literature by using copper, cobalt, and zinc ions as the metal supplier and carboxylic acid groups like 1,4-benzenedicarboxylic acid, 1,2-benzenedicarboxylic acid, and 1,3,5-benzenetricarboxylic acid as the ligand source, as illustrated in **Fig. 2.1** [69], [85]. Additionally, metal ions coordinated with ligand organic linkers with ethylenediamine addition [68]. To create the complexes, ethyl alcohol, dimethylformamide, and water are utilized as solvents. To make the MOFs, a mixture of 6 mL of MeOH and 3 mL of DMF with 0.1 mmol of metal salt in a 1:1 ratio is stirred for 20 minutes at room temperature. Then, 0.1 mmol of a ligand derived from carboxylic acid was added to a separate container along with a solvent mixture comprising 10 mL of organic solvent. This combination is slowly added to the initial mixture that has metal in it. This experiment, conducted under reflux

conditions, involves gradually raising the temperature over 24 hours to allow the mixture to combine.

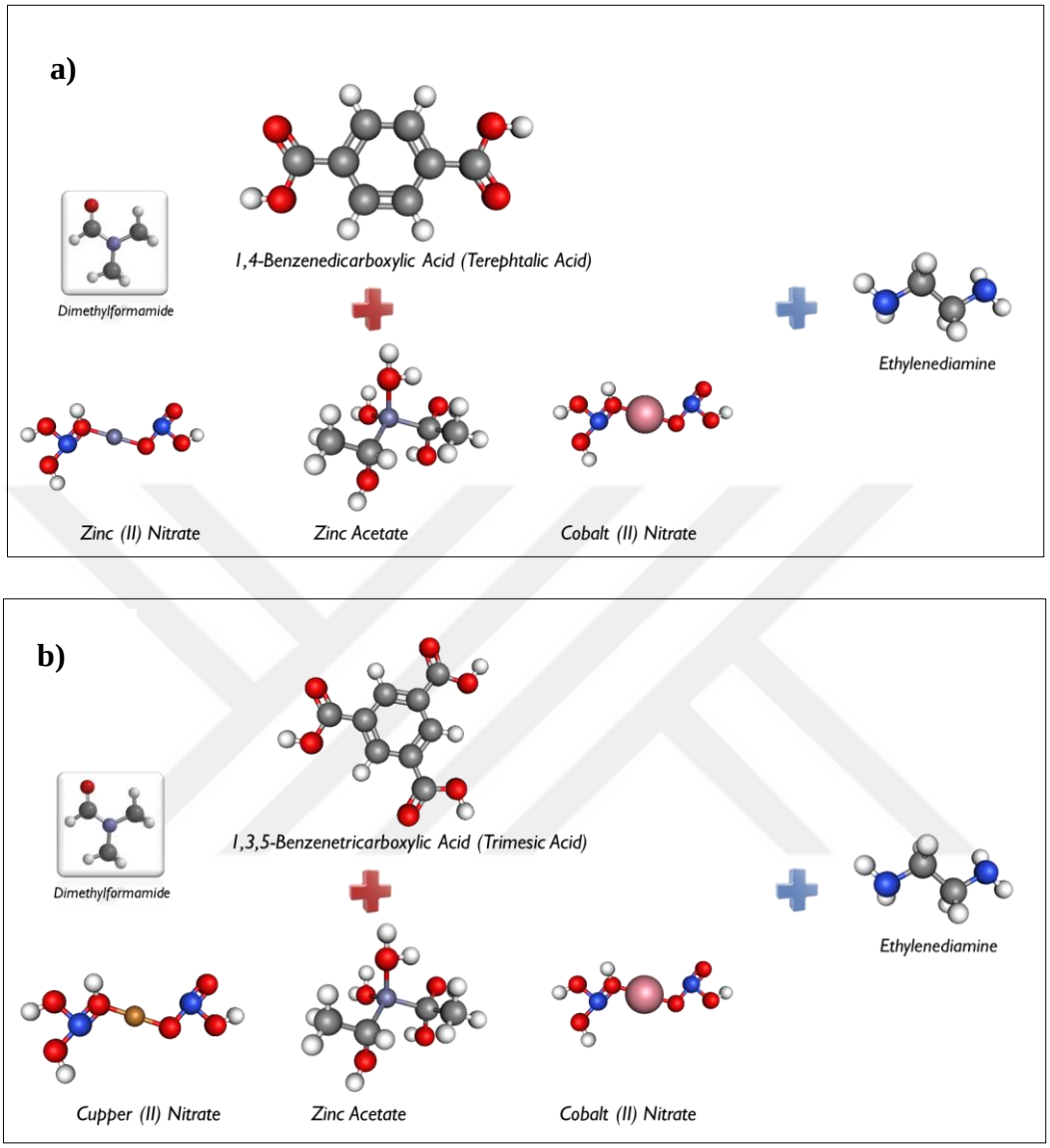


Figure 2.1. a) Metal Salt (Zinc(II) Acetate, Zinc(II) Nitrate or Cobalt(II) Nitrate) mixing with terephtalic acid ligand (1-2 benzenedicarboxylic acid) and **b)** Metal Salt (Zinc(II) Acetate, Cupper(II) Nitrate or Cobalt(II) Nitrate) mixing with trimesic acid ligand (1,3,5, Benzenetricarboxylic acid) with ethylenediamine addition into the dimethylformamide environments

One day later, the mixture is left to crystallise inside an ice bath; the solid mass that forms is filtered and washed with methanol, which the solvent used to prepare the compounds. Via vacuum drying, the organic material was dehydrated and preserved

for later use. The identical experimental procedures were executed in the coordination compound which includes metal.

M1 (Metal: Zinc(II) Nitrate), **M2** (Metal: Zinc(II) Acetate) and **M3** (Cobalt(III) Nitrate) was synthesized together with 1,4-Benzenedicarboxylic Acid based ligand following this procedure. On the other hand; **M4** (Metal: Copper(II) Nitrate), **M5** (Metal: Zinc(II) Acetate) and **M6** (Metal:Cobalt(III) Nitrate) was synthesized together with 1,3,5-Benzenetricarboxylic Acid based ligand following the same procedure.

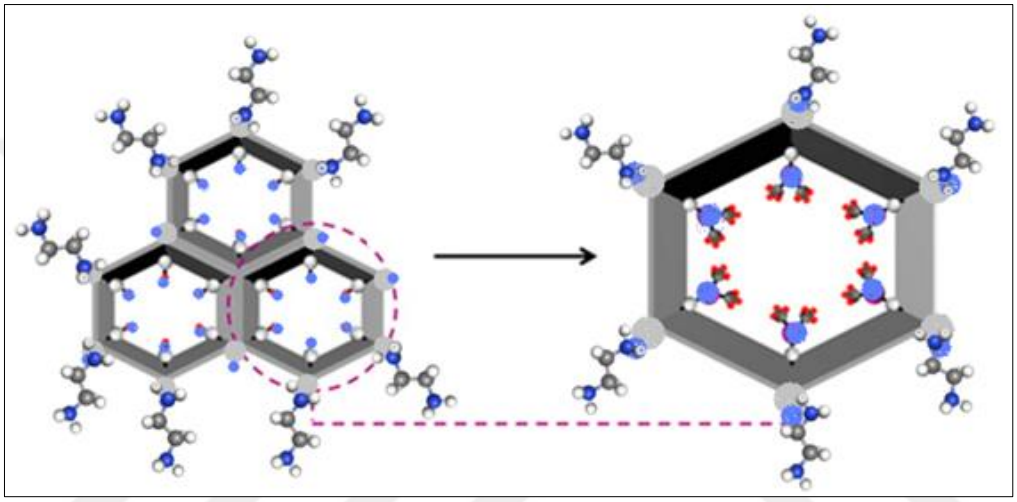


Figure 2.2. ED was incorporated as a ligand on the MOF sites

Solution-based synthesis method was used in the formation of ED modified MOFs. 4,4 mmol TPA, 0,42 mL ED, 44,41 mL DMF, and 3,82 mmol Zinc Acetate was mixed at 80°C. The mixture was allowed to crystallise in an ice bath for four hours. The solid white precipitate that developed was then separated by filtering and cleaned with DMF, which was utilised as a solvent in the complex production process. The resultant organic material was vacuum-dried for further use.

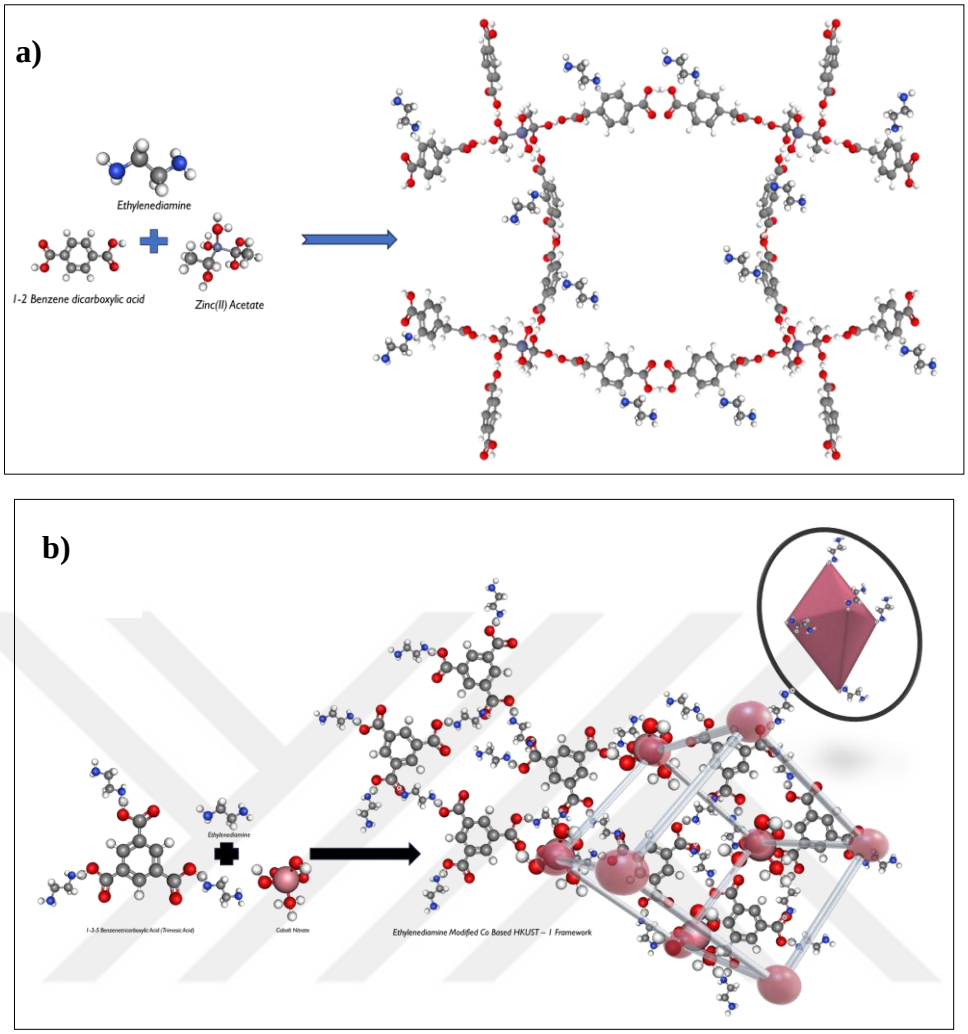


Figure 2.3. a) Zn based MOF: *With in situ ethylenediamine addition* **b)** Co based MOF: *The attachment of ED to the open metal sites of the water-stable, triazolate-bridged framework*

The other products were prepared hydrothermal method in teflon autoclave. After 6 hours of autoclave synthesis, the solid white precipitate formed then collected by filtration and washed with DMF used as a solvent in the preparation of the complexes. The organic solid obtained dried under vacuum for later use.

EM1 (Metal: Zinc(II) Nitrate Hexahydrate), **EM2** (Metal: Zinc(II) Acetate) and **EM3** (Cobalt(II) Nitrate Hexahydrate) was synthesized together with 1,4-Benzenedicarboxylic Acid based ligand following this procedure. On the other hand; **EM4** (Metal: Copper(II) Nitrate Hexahydrate), **EM5** (Metal: Zinc(II) Acetate) and **EM6** Cobalt(II) Nitrate Hexahydrate was synthesized together with 1,3,5-Benzenetricarboxylic Acid based ligand and Ethylenediamine addition following the same procedure as shown in **Table 2.1.**

Table 2.1. All synthesized MOFs

Produced MOF Name	***Metal Salt***	***Ligand + Functional Group***	***Solvent***
M1	$Zn(NO_3)_2$	1,4-Benzenedicarboxylic Acid	Dimethylformamide
M2	$Zn(O_2CCH_3)_2$	1,2-Benzenedicarboxylic Acid	Methanol + Dimethylformamide
M3	$Co(NO_3)_2$	1,4-Benzenedicarboxylic Acid	Methanol + Dimethylformamide
EM1	$Zn(NO_3)_2$	1,4-Benzenedicarboxylic Acid + Ethylenediamine	Methanol + Dimethylformamide
EM2	$Zn(O_2CCH_3)_2$	1,4-Benzenedicarboxylic Acid + Ethylenediamine	Methanol + Dimethylformamide
EM3	$Co(NO_3)_2$	1,4-Benzenedicarboxylic Acid + Ethylenediamine	Methanol + Dimethylformamide
M4	$Cu(NO_3)_2$	1,3,5-Benzenetricarboxylic Acid	Dimethylformamide
M5	$Zn(O_2CCH_3)_2$	1,3,5-Benzenetricarboxylic Acid	Methanol + Dimethylformamide
M6	$Co(NO_3)_2$	1,3,5-Benzenetricarboxylic Acid	Methanol + Dimethylformamide
EM4	$Cu(NO_3)_2$	1,3,5-Benzenetricarboxylic Acid + Ethylenediamine	Methanol + Dimethylformamide
EM5	$Zn(O_2CCH_3)_2$	1,3,5-Benzenetricarboxylic Acid + Ethylenediamine	Methanol + Dimethylformamide
EM6	$Co(NO_3)_2$	1,3,5-Benzenetricarboxylic Acid + Ethylenediamine	Methanol + Dimethylformamide

2.3 Fabrication of Electrodes

The synthesis involved the concurrent incorporation of metal organic frameworks (MOFs) into the matrix of a conductive polymer, specifically polypyrrole, through an electrochemical process, resulting in the creation of novel composite materials for supercapacitor electrodes[68], [69].

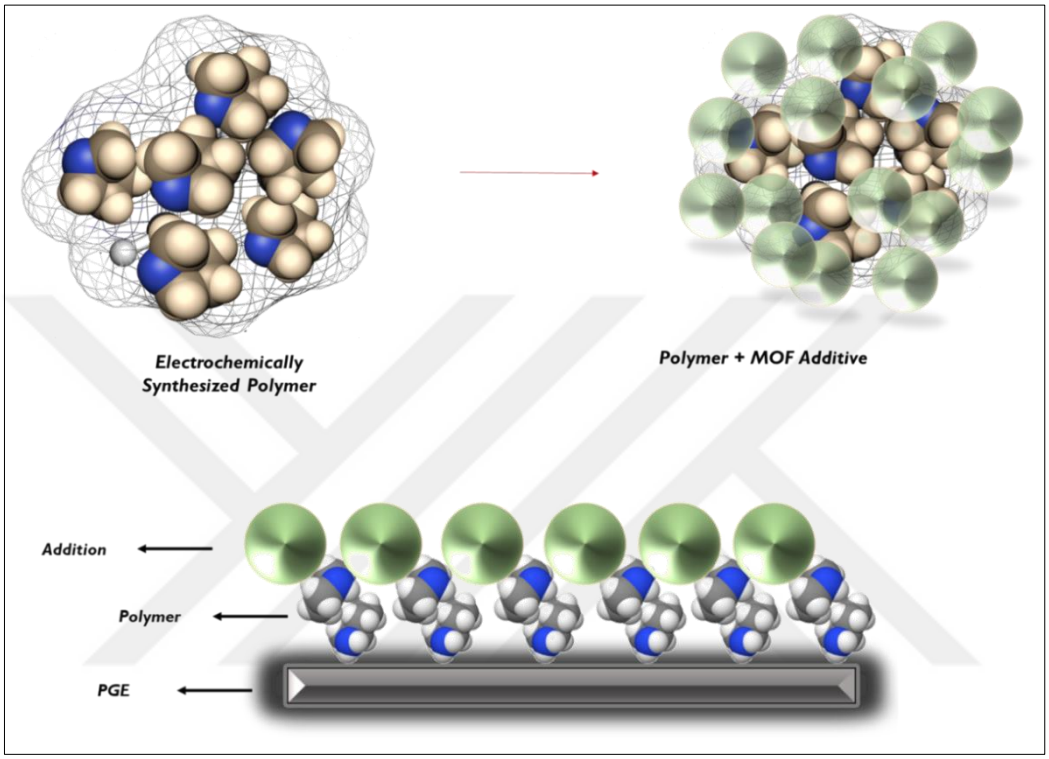


Figure 2.4. Preparation of polypyrrole based electrodes

The MOFs synthesized in the thesis were incorporated into the electrochemically produced conductive polymer (polypyrrole) structure, resulting in the production of new composite supercapacitor electrode materials **(Fig. 2.4.)**. The electrolysis solution consists of 0.1 M sulfuric acid and 0.1 M pyrrole, with electrochemical polymerization of pyrrole taking place within a potential range of -0,3 V to 1 V (in 3 M KCl referencing Ag/AgCl) at a scanning rate of 50 $mV.s^{-1}$ for 10, 20, 30, 40, and 50 cycles. Pt wire will be utilized as the counter electrode. After characterizing the polypyrrole based electrodes, different amounts of the prepared coordination compound (5 mg, 10 mg, 15 mg, 20 mg, and 25 mg) were incorporated into the polymerization solution to create polypyrrole based composite materials containing MOFs, as depicted in **Table 2.1** and **Fig. 2.4.**

2.3.1 Electrochemical Cell Design

In the investigations pertaining to energy, electrochemical characterisation of the surface changes is crucial [142]. The idea behind this work was to use cyclic voltammetry to measure the produced electrodes' capacitive behaviours [143].

Using CV and EIS analysis, the research's initial phase examined the factors—such as acid concentration, monomer concentration, and cycle number—that affect the electrodes' capacitive behaviors [69], [144], [145]. In this setup, the working electrode consisted of HB-grade Tombow pencil graphite with a diameter of 0.5 mm. The electrodes were cut into 3 cm lengths, with 1 cm of each piece submerged in the solution to achieve a surface area of 0.1 cm^2. However, the specific capacitance values that are achieved may be affected by variables such as the selection of electrolyte, electrode structure, and operational parameters.

2.4 Characterization Methods

Phase composition assessed using a Powder X-ray diffractometer. Cu Kα radiation with a wavelength of 1.54 Å was employed at 40 kV and 15 mA. The diffraction patterns were gathered between 10 and 90 degrees with an increment of 0.02 degrees. The analysis of the results was conducted using PDXL software by comparing them to the data in the library. The Zeiss EVO LS 10 instrument Scanning Electron Microscope (SEM) with an energy-dispersive spectrometer (EDS) was used to analyze the morphology, composition, and structure of the samples at various magnifications. The Quantachrome Corporation's Autosorb-6 device was used for BET analysis to calculate surface areas while the Perkin Elmer Spectrum One model equipment was used to record the chemical structure of electrodes with FT-IR spectra using the ATR technique. Elemental analyses were performed using a Perkin-Elmer 240C elemental analyser. Data from Thermogravimetric analysis (TGA) was gathered in a nitrogen environment, ranging from 21°C to 850°C, using a DTG thermo-analyser and a heating rate of 10 C/min. The Entek Electronic FPP470 model instrument was used to measure the electrical conductivity of electrodes using a 4-point method. Quantachrome Instrument was used to perform Brunauer-Emmett-Teller (BET) analyses.

The electrochemical tests were carried out using a three-electrode system, with a pencil graphite electrode as the working electrode, an Ag/AgCl electrode (in 3 M KCl) as the reference electrode, and a Pt wire electrode as the counter electrode. The evaluation of electrochemical properties involved conducting cyclic voltammetry (CV) at a speed of 50 mV/s across 0.0 to 1.0 V in a solution containing 1.0 M H_2SO_4. Furthermore, EIS tests were conducted with an Interface 1010B Potentiostat at different potentials, across a frequency range of 0.01 to 20,000 Hz, using a 5 mV potential in a 1.0 M H_2SO_4 solution.

The galvanostatic charge-discharge experiments included cycling from 0.0 to 0.7 V, using charge and discharge current densities of 1 $mA.cm^{-2}$ for 1000 cycles in a 1.0 M sulfuric acid solution. Every EIS spectrum was analyzed using an equivalent circuit model, shown in **Figure 2.5.**, with a fitting error rate below 5% for each.

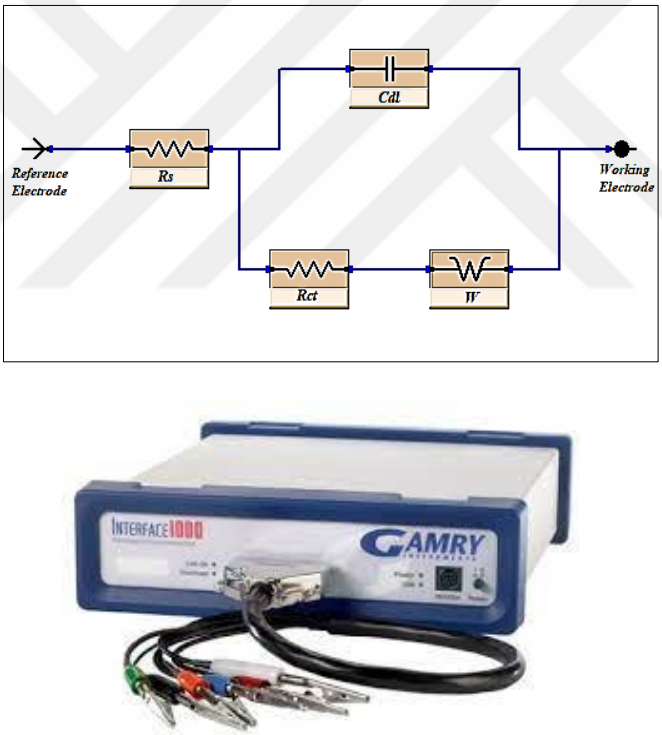


Figure 2.5. Used equivalent circuit model for fitting process of electrochemical impedance spectroscopy spectra and Gamry Interface 1010B Potenstiostat device.

3
RESULTS AND DISCUSSION

3.1 Characterization of the Metal Organic Frameworks

The synthesis of MOFs with various metal ions and ligands through chemical techniques, followed by their structural characterization using FT-IR, elemental analysis, P-XRD, BET study for surface area measurements, and analysis of properties through SEM-EDS and TGA techniques.

3.1.1 Characterization of the M1, M2 and M3 Group

- **Elemental Analysis of the M1, M2 and M3 Group**

The elemental analysis of M1, M2, and M3 MOFs generally shows good agreement between the theoretical and experimental values for carbon and hydrogen, confirming the successful synthesis of the frameworks.

As it can be seen from the **Table 3.1**, the carbon content shows a slight deviation from the theoretical value (36.19% experimental), which can be attributed to the presence of residual solvent molecules or incomplete incorporation of the organic linker. The minor difference in hydrogen content (1.45% experimental) suggests successful framework formation with minimal impurities. The absence of nitrogen in both the theoretical and experimental results is consistent with the lack of nitrogen-containing ligands or solvents in this MOF.

The theoretical values for the elemental analysis of M2 ($C_{11}H_{13}Zn_2NO_6$) align closely with the experimental findings, showing only small variations **(Table 3.1).** The carbon (C) level in the experiment is a bit higher at 35.28% compared to 34.23%. This could be due to the partial retention of the DMF guest molecules within the framework pores, which contributes to the increased carbon content. While the hydrogen (H) level is decreased at 2.13% instead of 3.39%, possibly indicating incomplete coordination or removal of DMF [133]. And the nitrogen (N) level is a bit higher at 4.09% compared to 3.63%. The elevated nitrogen content (3.63% theoretical) supports this hypothesis, as DMF contains nitrogen atoms, suggesting incomplete solvent exchange or guest molecule retention.

Table 3.1. shows that the experimental carbon and hydrogen contents for M3 are slightly lower than the theoretical values (C: 45.84%, H: 3.43%), which may indicate some loss of the organic ligand during synthesis or post-synthetic treatment. However, the experimental nitrogen content (3.01%) is higher than expected, possibly due to incomplete removal of DMF or partial framework decomposition.

Table 3.1 Theoretical calculated value of the M1, M2 and M3 group

Produced MOF	***Molecular formula***	***Molecular Weight (g/mol)***	***Theoretical (%) C, (%) H, (%) N***	***Experimental (%) C, (%) H, (%) N***
M1	$C_{24}H_{12}O_{13}Zn_4$ $Zn_4O(BDC)_3$	769.90	C:37.44% H:1.57%	C: 36.19% H: 1.45%
M2	$(Zn_2(PA).DMF)H_2O$	385.984	C, 34.23; H, 3.39; N, 3,63	C, 35.28; H, 2,13; N, 4.09%.
M3	$Co_2C_{24}H_{18}O_{12}C_3H_7NO$ $Co_2(BDC)_3.DMF$	689.357	C:47.04% H:3.66% N:2.03%	C: 45.84% H:3.43% N: 3.01%

- **Spectroscopic Analysis (FT-IR) of the MOF5, Zn-MOF5 and Co-MOF5 Group**

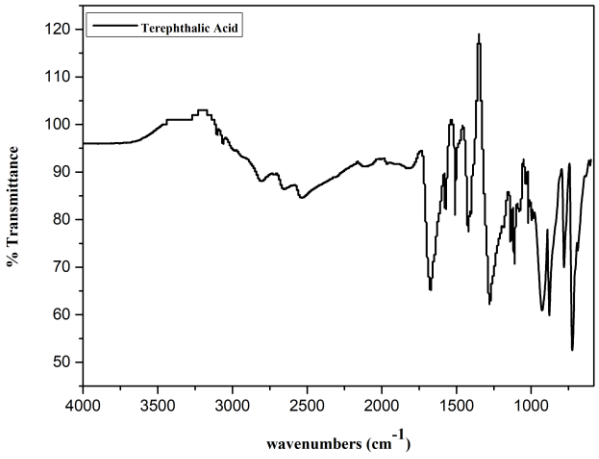
The FT-IR spectroscopy was used to determine the chemical structure of M1, M2 and M3. The complex's FT-IR spectrum from **Figure 3.1.** displayed distinct peaks resulting from the binding of carboxylate. The peaks observed at approximately 1663 cm^{-1} indicate the presence of the carbonyil group in ligand. As shoen in **Fig. 3.1.a**, peaks at approximately 2500 cm^{-1} and 3500 cm^{-1} correspond to stretching of the υ (COOH) group. The stretching of υ (C-O) in -COOH is also evident at 1230 cm^{-1}. Some υ(O-H) peaks vanished, suggesting the formation of a complex between

Zn and phthalic acid. The absence of the 2500 cm^{-1} bands of ligand in the complex's spectra is a result of the elimination of two hydrogens from the ligand's structure during the complex formation [146].

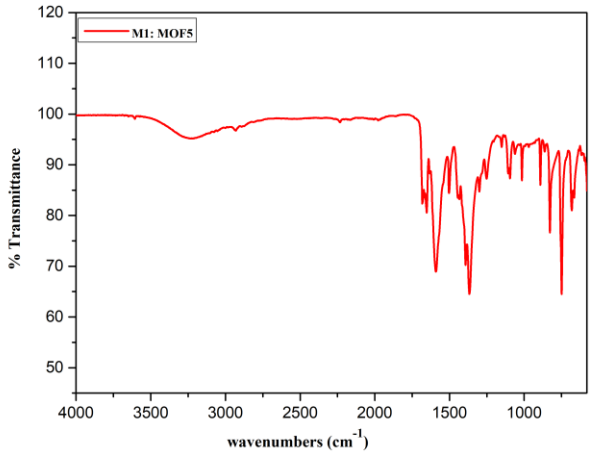
Moreover **Fig. 3.1.b** indicates that, υ(C=O) stretc vibration peaks at a decreased energy frequency. The appearance of the intense υ(C=O) stretching vibration indicates that the ligand is coordinating to the metal through the oxygen atoms in the carboxyl group. The M1 and M2 have υ (C=O) stretch vibrate ranging from 1659 cm^{-1} to 1606 cm^{-1} [147]. In M3, the peaks at approximately 633 cm^{-1} and 654 cm^{-1} represent the metal-oxygen bands (**Figure 3.1.c)**. The identified specific peaks confirmed the creation of an intricate arrangement of metals with ligand. The movement of the remaining peaks was detected in M3. It also aids in the creation of MOF.

The FTIR spectrum show characteristic bands for the BDC ligand, specifically C=O stretching of the carboxylate groups around 1650-1600 cm^{-1}, O-H stretching bands due to residual moisture or carboxylate groups around 3500-3400 cm^{-1}, Aromatic C-H bending vibrations appear near 1400-1500 cm^{-1}. Additionally **Fig 3.1.d** shows that DMF presence can be confirmed by the N–C=O stretching band near 1650-1620 cm^{-1}. Shifts in the carboxylate band compared to free BDC can confirm successful coordination to the cobalt metal centers. The disappearance or weakening of the free ligand's carboxylic acid (C=O) band near 1720 cm^{-1} also supports this[147].

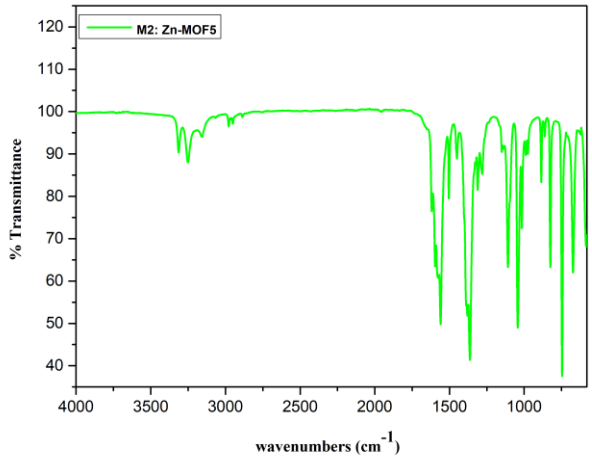
a)



b)



c)



d)

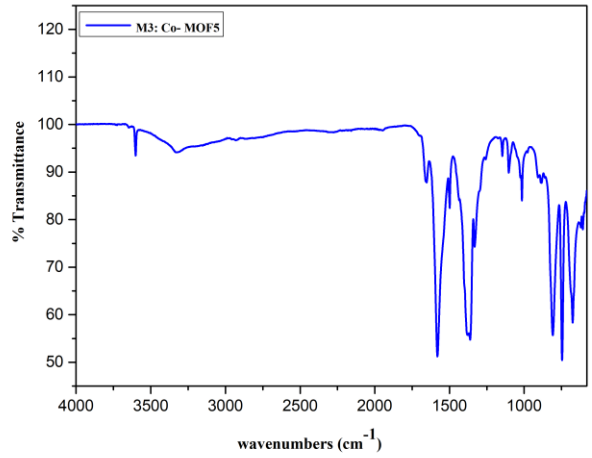


Figure 3.1. a) FTIR spectrum of the **a)** ligand terephtalic acid **b)** M1 **c)** M2 and **d)** M3

- **Surface Area Calculations (BET) of the M1, M2 and M3 Group**

The BET model in **Table 3.2** was used to assess the surface areas of the Zn based MOF that was synthesized. The MOFs' BET surface area was measured using the standard volumetric method with nitrogen gas adsorption at specific relative pressures and liquid nitrogen temperature (77 K). Degassing was carried out before the analysis by vacuum for thirty minutes.

The **Table 3.2** shows that surface area of M1 is moderate but significantly smaller compared to similar Zn-BDC MOFs reported in the literature. (BET Surface Area: 79.98 m^2/g and Pore Diameter: 1.16 nm). This could be attributed to incomplete activation of the framework, residual solvent molecules trapped in the pores, or partial pore collapse during synthesis. The relatively small pore diameter suggests that the MOF structure is more compact, which could limit access to the internal surface area.

The BET analysis revealed that the M2 has a specific surface area of 0.8195 m^2/g. The pore size of M2 was determined to be 1.1603 nm based on the BJH adsorption average pore diameter measurement (**Table 3.2**). As per BJH Adsorption findings, the cumulative volume of pores within the diameter range of 0.3600 nm to 300.0000 nm in M2 is determined to be 0.011600 cm^3/g. In the supercapacitor applications section, it is analyzed how the surface area impacts the supercapacitor properties. The relatively low surface area of M2 might be due to insufficient framework activation or the presence of defects within the structure that reduce the available surface. The small pore size, similar to M1, indicates a dense structure that could limit molecular diffusion.

As it can be seen from the **Table 3.2**, M3 shows a significantly higher surface area compared to M1 and M2, which is consistent with its cobalt-based framework (BET Surface Area: 353.10 m^2/g and Pore Diameter: 2.43 nm). The larger pore diameter of 2.43 nm suggests an open and accessible structure, which may improve its ability to adsorb larger molecules. The higher surface area and larger pore size make M3 an excellent candidate for applications such as gas adsorption, catalysis, or even drug delivery, where higher surface accessibility is critical.

Table 3.2 BET Surface area results of the MOF5 (M1), Zn-MOF5 (M2) and Co-MOF5 (M3) group

Produced MOF	***BET Surface Area***	***Single point adsorption total pore volume***	***Adsorption average pore diameter***	***BJH Adsorption average pore width***	***Average Particle Size***
M1	79,984 m^2/g	0,1160cm^3/g	1,1603 nm	*	*
M2	47,726 m^2/g	0,1411 cm^3/g	1,1808 nm	*	*
M3	353,1036 m^2/g	0,2147 cm^3/g	2,4329 nm	4,8451 nm	16,9922 nm

*: The device being analyzed does not support this feature.

- **Thermal Analysis (TG-DTA) of the M1, M2 and M3 Group**

The thermogravimetric analysis curve of M1, M2 and M3 weight loss was noticed between temperatures of 50 °C and 500 °C when examining the material's thermogram, indicating its that stable thermally up to 50 °C **(Fig.3.2.).** All the materials underwent four primary weight losess. The initial weight loss between 50-90 °C is due to water (H_2O) being released, while the second weight loss at approximately 160 °C is caused by the elimination of DMF solvent from the pore. As a general comment for **Fig. 3.2,** the third significant decrease in weight occurs when the temperature ranges between 200 °C and 350 °C due to the organic matrials linker in the MOF breaking down. After 360 °C, the TGA curve showed residual weight, indicating the formation of a crystalline phase and complete removal of guest molecules for weight loss [148].

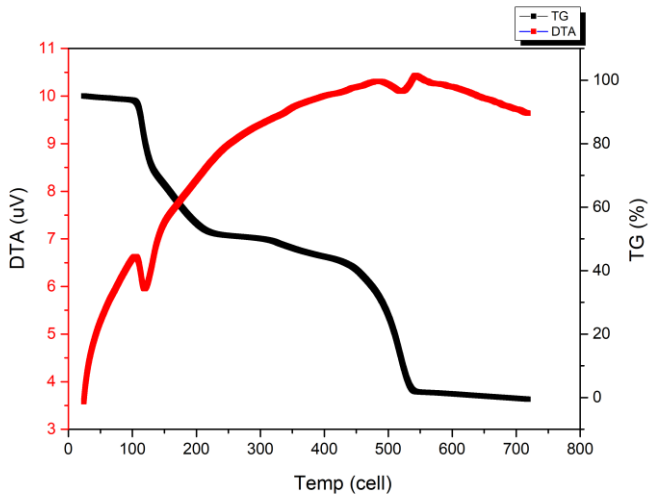
Fig 3.2.a shows that M1 exhibits a TGA profile with two main weight loss regions. The first significant weight loss, occurring up to around 200°C, is likely attributed to the loss of solvent molecules or coordinated water. The second stage of weight loss corresponds to the decomposition of the organic linker (1,4-Benzenedicarboxylic Acid) and the collapse of the MOF framework. It is supported

by the elemental analysis reulsts of **Table 3.1**. The experimental carbon content is slightly lower than the theoretical value, suggesting some degree of decomposition or loss of organic components during heating. This slight discrepancy aligns with the observed weight loss stages, indicating that while the MOF retains much of its structure, some organic content may be lost before complete degradation.

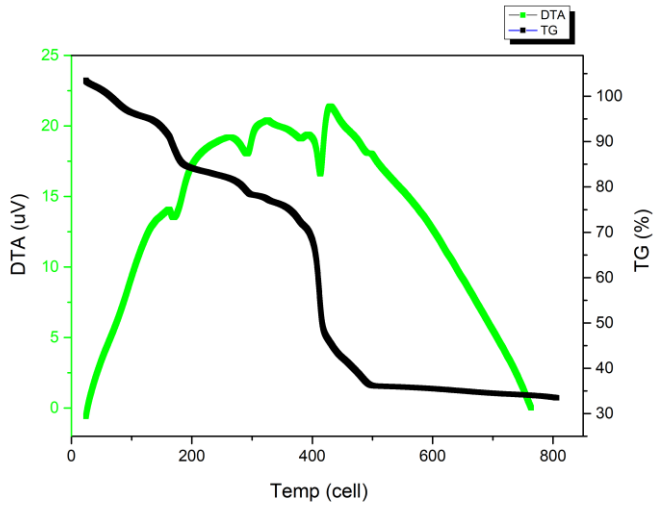
For M2, the TGA results show a distinct profile with weight loss stages reflecting the removal of solvents and decomposition of the organic linker **(Fig.3.2.b).** The profile show less pronounced weight loss compared to M1 **(Fig.3.2.a)**, potentially indicating a more stable structure or different interaction with solvents. When it compared by the elemental analysis results by **Table 3.1**., the experimental carbon content suggesting that the framework composition is well-maintained with minimal loss of organic components. The TGA results align with this, showing that while there is some decomposition.

M3 displays significant weight loss in four main stages in **Fig. 3.2.c**. The first stage, up to approximately 200°C, may correspond to the loss of solvent or coordinated water molecules, while the other stages indicate decomposition of the organic linker or collapse of the framework. The experimental elemental analysis from **Table 3.1.** suggesting possible incomplete combustion of the organic components or partial decomposition of the framework. The observed stability before complete degradation aligns with the expected behavior of cobalt-based MOFs.

a)



b)



c)

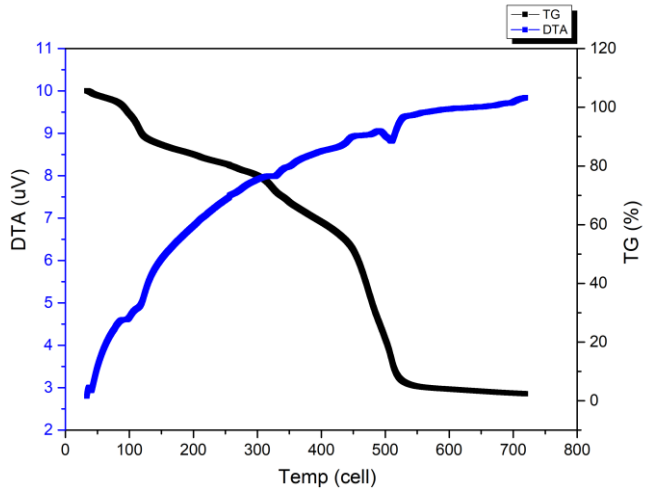


Figure 3.2. a) Thermal analysis of M1 **b)** M2 and **c)** M3

- **Structural Analysis (XRD) of the M1, M2 and M3 Group**

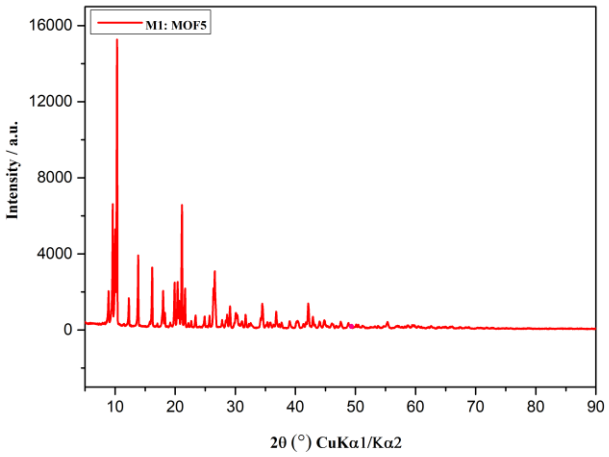
XRD analysis was conducted to identify the crystal structure of M1, M2 and M3 **(Fig.3.3.)**. The XRD pattern for M1 display well-defined peaks corresponding to the phase purity and crystalline nature of the MOF **(Fig.3.3.a)**. The presence of distinct peaks indicates that M1 maintains a crystalline structure, consistent with the expected pattern for Zn-based MOFs with 1,4-Benzenedicarboxylic Acid. The sharp and intense peaks is in line with the typical structural framework of $Zn_4O(BDC)_3$, reflecting successful synthesis and stability of the MOF under the experimental conditions.

In the **Fig. 3.3.b**, the crystal peaks of M2 are displayed. The crystal structure of the M2 compound is revealed by the X-ray powder diffraction pattern. The goal is to demonstrate that the MOF does not have an amorphous structure solely based on

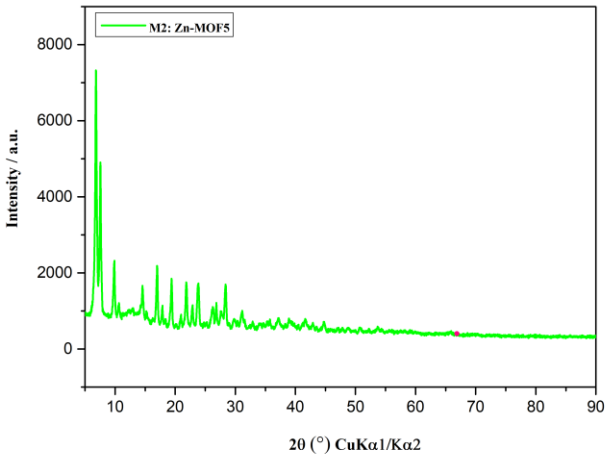
the presence of a diffraction pattern. This peak corresponds well with SEM resulst, indicating the proof of a composite caretion, with enhancements in specific peak intensities.

XRD pattern of M3 from the **Fig. 3.3.c** also show well-defined peaks, indicative of its crystalline nature. The observed peaks match the characteristic pattern for $Co_2(BDC)_3$, suggesting successful incorporation of cobalt into the MOF structure. The presence of sharp peaks confirms good crystallinity and phase purity.

a)



b)



c)

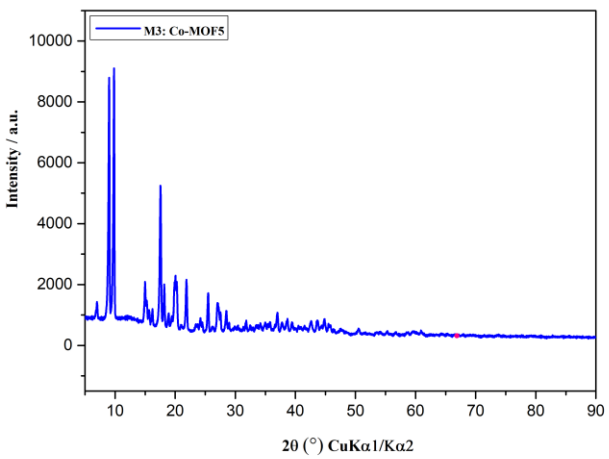


Figure 3.3. The XRD pattern of **a)** M1, **b)** M2 and **c)** M3

- **Morphological Analysis (SEM and EDS) of the M1, M2 and M3**

The SEM images of M1, produced using zinc nitrate, deviate from the typical MOF-5 structure **(Fig. 3.4.a).** However, the existence of a crystalline and extremely porous framework signifies successful formation. The variations in morphology could be due to the synthesis conditions or the type of zinc(II) nitrate used as a precursor [147]. Significantly, the arrangement continues to exhibit a tetrahedral shape akin to regular MOF-5.

The contrast in structure seen in **Fig. 3.4.b**, M2 made with zinc acetate versus zinc nitrate is due to the type of starting salt used. Zinc(II) acetate could cause a change in the nucleation and growth process when synthesizing, leading to different crystal shapes and sizes [133]. In spite of these morphological distinctions, the substance still maintains a high level of porosity, which is beneficial for use in electrochemical supercapacitors. The porous arrangement aids ion movement and boosts the available surface area for storing charge, improving the supercapacitor's effectiveness [148]. Furthermore, the incorporation of zinc(II) acetate might lead to the development of more advantageous electrochemical characteristics, ultimately enhancing the effectiveness of the material for energy storage purposes [149]. The structures still show the characteristic tetrahedral geometry of MOF-5.

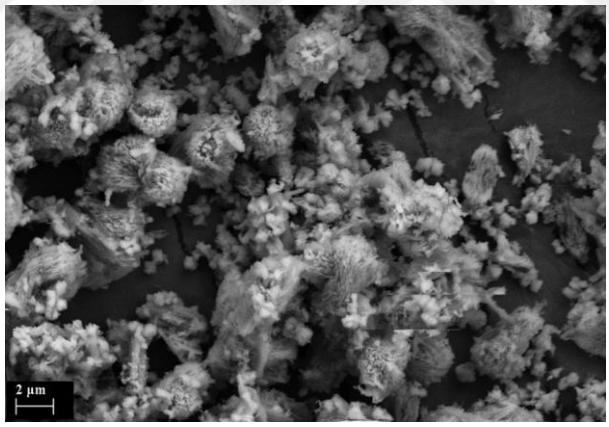
The morphology of M3 synthesized with cobalt nitrate in SEM images closely resembles that of M2 (**Fig. 3.4.c**). The reason for this resemblance is the similar

metal centers (zinc and cobalt) that create comparable coordination environments in the MOF-5 structure. Both metals can take on alike shapes and coordination numbers, resulting in similar crystal structures. The significant porosity seen in M3 matches the qualities of M2 **(Fig.3.4.b),** indicating that replacing zinc with cobalt doesn't greatly change the overall framework structure [150]. This permeability is advantageous for multiple uses, including catalysis, gas adsorption, and energy storage. Moreover, it seems that the arrangements follow the tetrahedral shape commonly found in MOF-5, preserving the overall structure [151]

a)



b)



c)

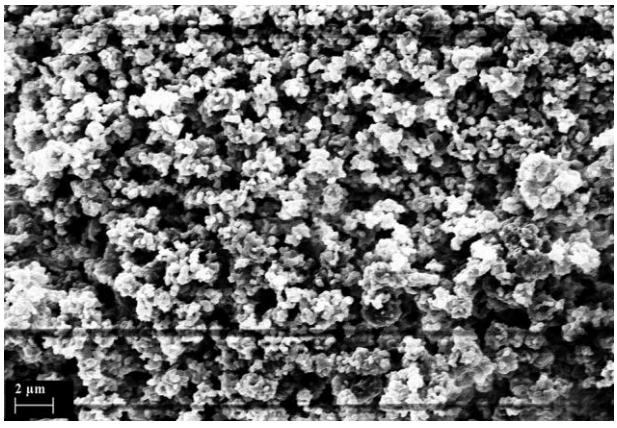


Figure 3.4. The SEM image of synthesized **a)** M1 at 5000x magnification **b)** M2 at 5000x magnification and **c)** M3 at 5000x magnification.

Table 3.2. EDS analysis results of M1, M2 and M3 group

Produced MOF	***C (%)***	***N (%)***	***O (%)***	***Zn (%)***	***Co%***
M1	30,80	02,84	30,19	36,93	-
M2	31,94	03,12	31,67	33,27	-
M3	31,41	02,04	36,15	-	36,01

The EDS analysis of M1 from the **Table 3.2.** shows that it is mainly composed of zinc, carbon, and oxygen, with some nitrogen present in smaller quantities. The substantial zinc concentration aligns with the metal organic framework design, with zinc serving as the central metal [96]. In M3, the elemental composition revealed by EDS is comparable to that of M1, but cobalt is substituted for zinc as the metallic core **(Table 3.2)**. The levels of carbon and oxygen are similar in both samples due to their matching organic connectors and overall framework configuration. The small difference in nitrogen levels could result from variations in the coordination setting or the synthesis process [68]. The fact that cobalt makes up 36.01% of the composition confirms the successful addition of cobalt to the M1 framework, leading to a structure that resembles the M2 composition and maintains the structural geometry. These findings from **Table 3.2.** show that the synthesis of M2 and M3 was successful, with both maintaining their elemental integrity and expected distribution, confirming the substitution of zinc with cobalt in the framework.

3.1.2 Characterization of the ED modified EM1, EM2 and EM3 Group

- **Elemental Analysis of the ED modified EM1, EM2 and EM3 Group**

In accordance with the elemental results, the introduction of amine led to an augmentation of the nitrogen content within the elemental composition by 15%. This increase is analogous to a substantial level of ethylenediamine grafting onto the network. Theoretical elemental analysis results, as shown in **Table 3.3**, were computed using JASPER V2 (Javascript Percentage Elemental Results Calculator).

The anticipated molecular structure formula was predicted to encompass 2 zinc atoms, 3 ethylenediamine (ED) molecules, 3 N,N-dimethylformamide (DMF) molecules, and 1 terephthalic acid ligand, represented as $C_{29}H_{55}N_9O_{15}Zn_2$. These theoretical outcomes were in concordance with the experimental elemental analysis data presented in **Table 3.3**, exhibiting a discrepancy of less than two percent. This alignment strongly suggests the successful formation of the desired MOF and ethylenediamine (ED) molecules within the structure [68].

For the ethylene modified EM1, the experimental nitrogen content (15.46%) is notably higher, indicating successful incorporation of ethylenediamine into the framework. This observation is supported by the elevated carbon content (41.42%), suggesting that ethylenediamine is well-coordinated within the pores or as part of the framework structure. However, the lower hydrogen content (5.07%) could imply some loss of solvent or partial decomposition during analysis, affecting the overall composition.

Similar to EM1, the nitrogen content is higher than the theoretical value (15.29%) confirming the incorporation of ethylenediamine. The slight increase in carbon content (36.55%) is consistent with the presence of DMF or residual ethylenediamine in the framework. The reduced hydrogen content (3.07%) again indicate partial solvent loss or framework modification during synthesis.

For EM3, the experimental nitrogen content (7.86%) is slightly lower than expected, which may suggest partial incorporation of ethylenediamine or loss during synthesis. The slight reduction in carbon content (44.59%) could be due to minor structural changes during synthesis or guest molecule loss. The hydrogen content (4.86%) shows only a small variation, indicating relatively stable framework formation with ethylenediamine incorporation.

The ethylenediamine-modified MOFs (EM1, EM2, and EM3) exhibit significant differences between theoretical and experimental values, particularly in nitrogen content as shown in **Table 3.3**. These variations highlight the influence of ethylenediamine on the framework composition. The fundamental results shows that 15% more nitrogen was present in the structure of elements after the addition of amine. This increase corresponds to an important portion of ethylenediamine binding to the framework.

Table 3.3. Theoretical calculated value of the EM1, EM2 and EM3 group

Produced MOF	***Molecular Formula***	***Molecular Weight (g/mol)***	***Theoretical (%) C, (%) H, (%) N***	***Experimental (%) C, (%) H, (%) N***
EM1	$Zn_2C_{24}H_{18}O_{12}C_3H_7NOC_4H_{16}N_4$ $Zn_2(BDC)_3.DMF.(ED)_2$	822.45	C:39.92% H:6.81% N:13.52%	C:41.42% H: 5.07% N:15.46%
EM2	$Zn_4C_{24}H_{18}O_{12}C_3H_7NOC_4H_{16}N_4$ $Zn_4(BDC)3.DMF.(ED)_2$	953.21	C:35.77% H:5.03% N:13.65%	C:36.55% H: 3.07% N:15.29%
EM3	$Co_2C_{24}H_{18}O_{12}C_3H_7NOC_4H_{16}N_4$ $Co_2(BDC)_3.DMF.(ED)_2$	809.557	C:45.99% H:5.11% N:8.65%	C:44.59% H: 4.86% N:7.86%

- **Spectroscopic Analysis (FT-IR) of the ED modified EM1, EM2 and EM3 Group**

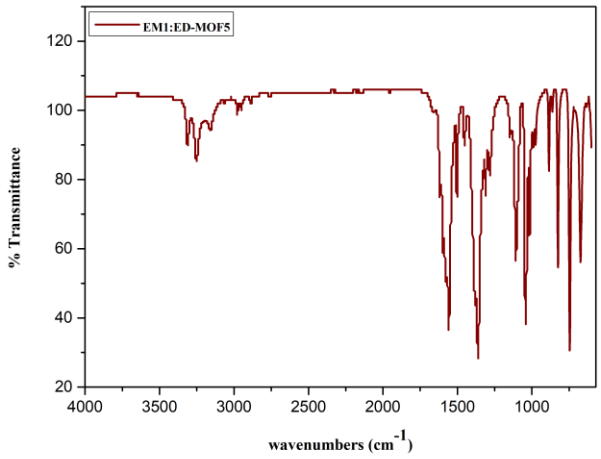
This method confirmed the effective attachment of ED onto MOF. The spectra we collected showed that peaks linked to the MOFs matched those found in previous studies, confirming their placement in the chemical structure. The characteristics of the ethylenediamine-modified material EM1 from **Fig. 3.5.a** show distinctive traits in the range of 3050-2900 cm^{-1}, indicating the stretching of bonds in the aliphatic CH_2 group's C-H and aromatic C-H [152].

For EM2, a zinc-based MOF modified with ethylenediamine (ED), In addition to the typical BDC and DMF bands (as seen in M2), the ethylenediamine modification will introduce N-H stretching vibrations of ethylenediamine around 3300-3200 cm^{-1}, C-N stretching around 1250-1350 cm^{-1} from the ethylenediamine. Coordination of ethylenediamine to zinc shift the carboxylate peaks slightly due to additional interaction with the metal center **(Fig.3.5.b).** The presence of new peaks corresponding to N-H and C-N stretching confirm the incorporation of

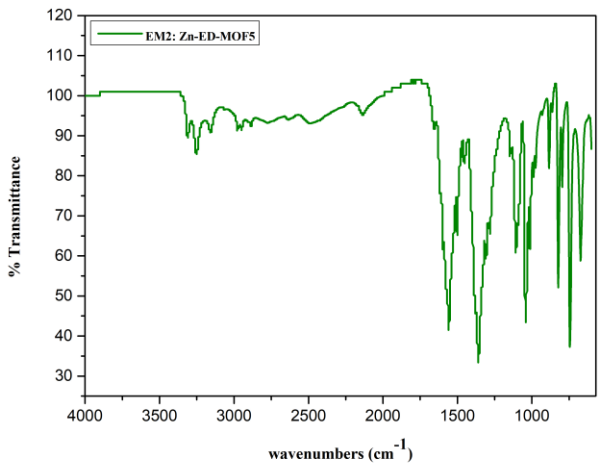
ethylenediamine. A comparison with unmodified MOFs (like M2) show these additional peaks.

EM3 from **Fig.3.5.c** Similar to EM2, expect to see BDC bands for C=O, O-H, and C-H stretching and Ethylenediamine N-H stretching around 3200-3300 cm^{-1} and C-N stretching around 1250-1350 cm^{-1}. Additionally, DMF presence with the N-C=O stretching around 1620 cm^{-1}. Coordination shifts in the carboxylate peaks due to ethylenediamine interaction with cobalt. The introduction of ethylenediamine caused additional bands in the FTIR, particularly in the N-H and C-N regions. Comparison with M3 (without ethylenediamine) will highlight the changes induced by the modification.

a)



b)



c)

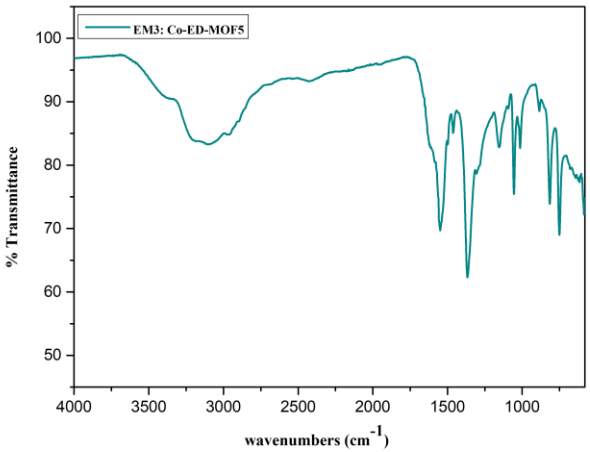


Figure 3.5. FTIR spectrum of synthesized **a)** EM1 **b)** EM2 and **c)** EM3

- **Surface Area Calculations (BET) of the ED Modified EM1, EM2 and EM3 Group**

The surface area of the EM1 was estimated using the Brunauer-Emmett-Teller method. It is expected that the capacitance of EM1 (0.049 cm^3/g) will exceed that of EM2 (0.016 cm^3/g) due to the reduction in average micropore size, even though the former is created using a simple solution-based method and the latter is made through hydrothermal synthesis among these various synthesis methods. It is acknowledged that ions are able to enter smaller pores than their size, which results in improved capacitance formation [153].

Similar to EM1, EM2's surface area decreases upon modification with ethylenediamine **(Table 3.4).** This is likely due to pore blockage, which restricts the available surface area. However, the pore diameter increases to 4.88 nm, indicating a more open structure compared to the unmodified M2. This increase in pore size could enable EM2 to accommodate larger molecules, making it a potential candidate for applications like heterogeneous catalysis, where pore size plays a key role.

For the surface area reulsts of EM3, the reduction in surface area can be attributed to the ethylenediamine modification, which likely causes pore blocking or partial structural collapse. Despite this, the avrg particle size provided in **Table 3.4** remains relatively large (80 nm), allowing for potential applications is important.

Table 3.4. BET Surface area results of the EM1, EM2 and EM3 group

Produced MOF	***BET Surface Ara***	***Single point adsorption total pore volume***	***Adsorption average pore diameter***	***BJH Adsorption average pore width***	***Average Particle Size***
EM1	46,528 m^2/g	0,049303 cm^3/g	8,4851 nm	14,35722 nm	*
EM2	26,188 m^2/g	0,015501 cm^3/g	4,8768 nm	12,04709 nm	*
EM3	74,7351 m^2/g	0,085117 cm^3/g	4,5557 nm	4,6205 nm	80,2836 nm

*: The device being analyzed does not support this feature.

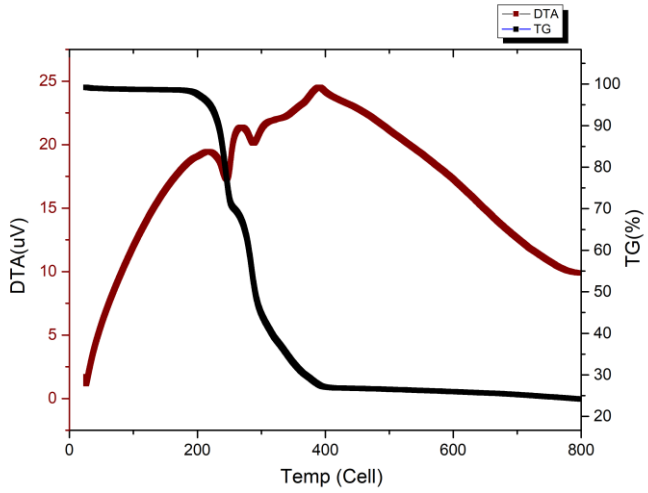
- **Thermal Analysis (TG-DTA) of the ED modified EM1, EM2 and EM3 Group**

The thermal behavior of MOF-5 is significantly different when modified with ethylenediamine EM1 from **Fig.3.6.a** shows two main stages for losing weight, as opposed to the four stages seen in the original MOF-5. The decrease in weight loss steps signifies a shift in the decomposition process and hints at an improvement in the material's thermal stability [154].

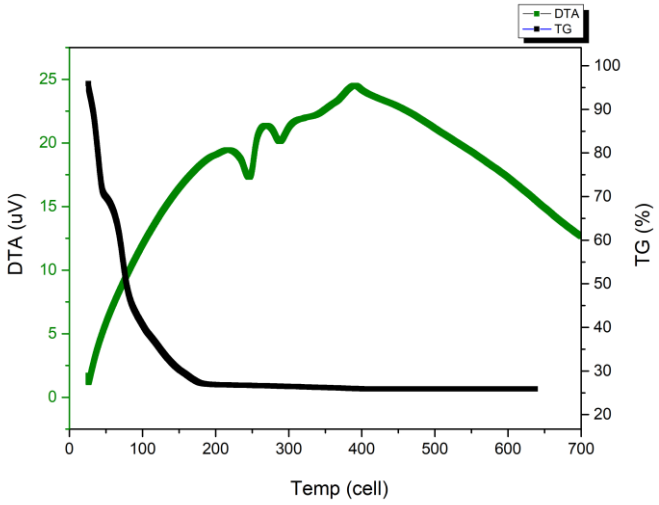
For EM2, the TGA profile from **Fig.3.6.b** reveal weight loss in stages, similar to other MOFs, but with additional weight loss associated with the ethylenediamine component. The significant modification with ethylenediamine is likely to impact the stability and degradation profile. From the elemental analysis reulsts, the experimental carbon content is close to the theoretical value, which suggests that the ethylenediamine modification does not drastically alter the overall composition but could influence the thermal stability and degradation pattern, potentially showing a loss corresponding to the ethylenediamine and other organic components.

EM3 is expected to exhibit a TGA profile with weight loss stages similar to M3, but with additional losses attributed to the ethylenediamine. The modification might lead to a more complex decomposition pattern **(Fig.3.6.c).** The experimental elemental analysis suggests that the ethylenediamine incorporation is effective but might cause some changes in the thermal stability or complete combustion.

a)



b)



c)

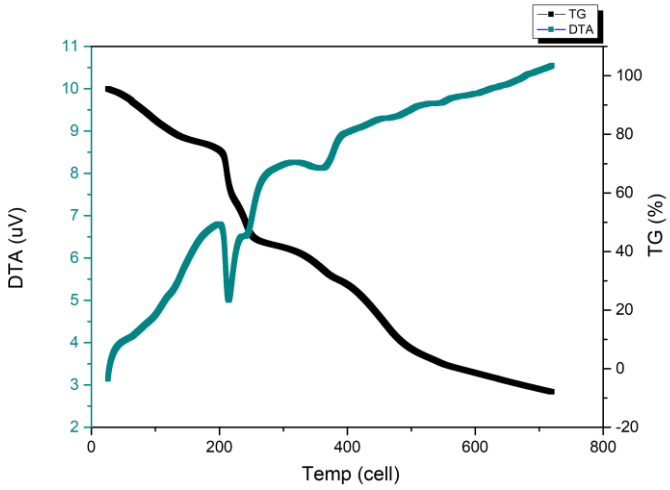


Figure 3.6. Thermal analysis of synthesized **a)** EM1 **b)** EM2 and **c)** EM3

The incorporation of ethylenediamine into the MOF-5 framework probably leads to the creation of more robust coordination interactions between the ethylenediamine molecules and the metal sites [68]. The increased connections can result in a more solid structure, as shown by the fewer and more noticeable weight loss events in the TG-DTA study. The initial weight loss could result from the removal of water and solvents, while the subsequent loss is likely due to the decomposition of the framework, which is now strengthened by ethylenediamine [119].

- **Structural Analysis (XRD) of the ED modified EM1, EM2 and EM3 Group**

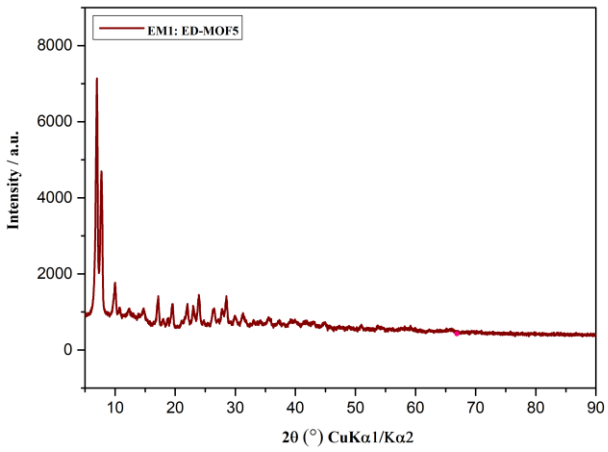
X-ray diffraction (XRD) was utilized to determine the phase and composition of the products, as shown. In contrast to the few diffraction peaks at low angles observed in the **Fig. 3.7.a** and **Fig.3.7.b**, XRD patterns of MOF5 below 15 degrees, the strong correlation between EM1 and EM2 signifies a crystalline product with excellent phase purity [149].

Moreover, it shows the retention of the crystalline form following the ethylenediamine (ED) process. The ethylenediamine curve shows distinct peaks, demonstrating the preservation of the organic structure and the achievement of amine grafting. Moreover, the EM2 demonstrates precise peaks, confirming the lack of a disordered composition (**Fig. 3.7.b)**. The identical diffraction patterns of

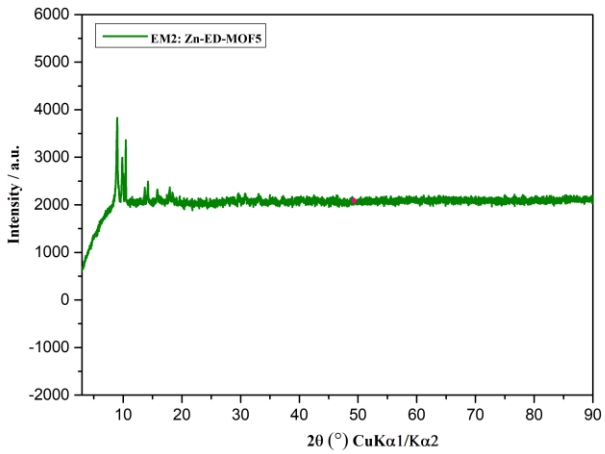
both samples in the image further emphasize that they have the same crystal structure. The significant height of every intensity peak highlights the excellent crystalline quality of the samples [85].

The XRD pattern for EM3 from **Fig. 3.7.c** show peaks corresponding to the crystalline structure of $Co_2(BDC)_3$, though some differences observed due to the incorporation of ethylenediamine. While the peaks may be less intense or slightly shifted compared to M3, they still confirm a crystalline phase. Despite potential changes in peak intensity or position, the presence of characteristic peaks indicates that the ethylenediamine modification has not severely disrupted the crystalline structure, and EM3 remains a crystalline MOF.

a)



b)



c)

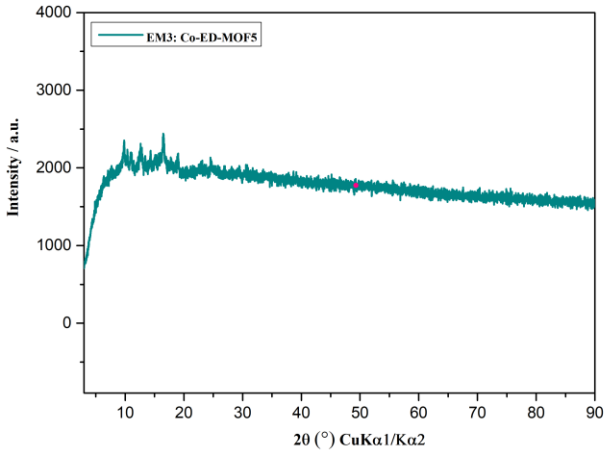


Figure 3.7. The XRD pattern of synthesized **a)** EM1 **b)** EM2 and **c)** EM3

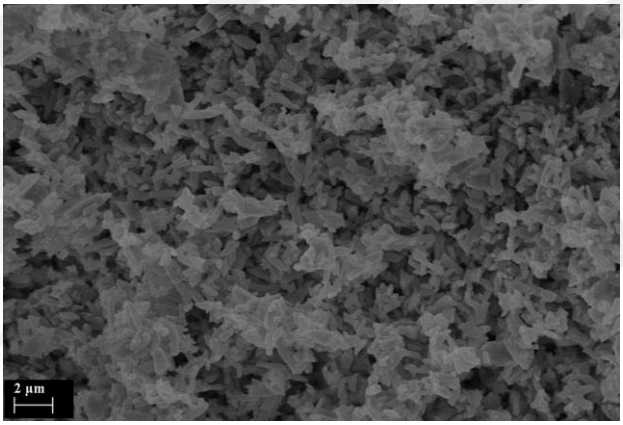
- **Morphological Analysis (SEM and EDS) of the ED modified EM1, EM2 and EM3 Group**

Results from SEM-EDS analysis of EM1 and EM2 confirm the incorporation of molecules into the matrix **(Fig.3.8.a** and **Fig.3.8.b)**. The results from EDS indicate the existence of carbon, nitrogen, oxygen, and zinc in the structural framework. These components are associated with the primary substances utilized in the synthesis procedure. Ethylenediamine and dimethylformamide provide the nitrogen in the content.

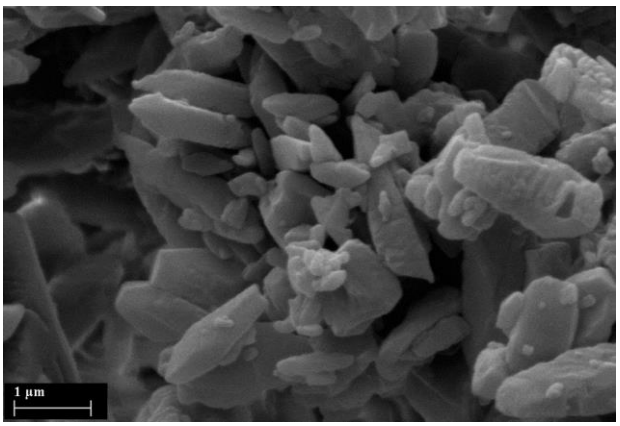
The structural characteristics of the altered metal organic framework were investigated using scanning electron microscopy. The SEM images for EM1 and EM2 can be seen in **Fig.3.8.a** and **Fig.3.8.b**, respectively. The use of ethylenediamine led to the creation of a consistent octahedral shape, as seen under scanning electron microscopy. The smooth-textured shuttle-like nanorods display a uniform dispersion pattern within their structure. (**Fig. 3.8.a**), whereas EM2 prepared via hydrothermal synthesis displays a more porous arrangement (**Fig. 3.8.b**). The difference is probably a result of different synthesis conditions. EM2 was formed by heating and pressurizing in a Teflon-lined stainless steel autoclave at levels higher than those used for EM2, leading to a porous structure resembling a sponge [133].

The SEM images of EM3 from **Fig.3.8.c** reveal a highly porous structure similar to MOF-5, which is consistent with its ligand and metal basis. The presence of ethylenediamine appears to have maintained or even enhanced the porosity of the material. The incorporation of ethylenediamine in EM3 has likely contributed to increased stability while preserving the porous characteristics. This indicates that the modification not only maintains but may enhance the MOF's ability to retain its structure and porosity under various conditions. All substances have pores that are a micrometer wide or smaller, creating a suitable setting for efficient charge interaction. The electric double-layer capacitor is enhanced by the absorption of ions in these small spaces, possibly leading to partially dissolved counterions [41].

a)



b)



c)

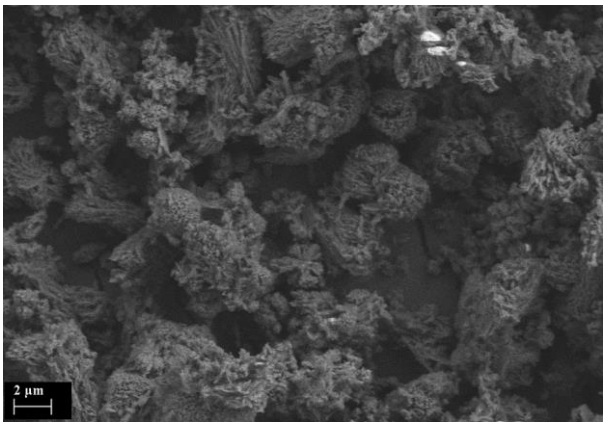


Figure 3.8. The SEM images of synthesized **a)** EM1 at 10000x magnification **b)** EM2 at 5000x magnification and c**)** EM3 at 5000x magnification

Table 3.5. EDS analysis results of EM1, EM2 and EM3 group

Produced MOF	**C (%)**	**N (%)**	**O (%)**	**Zn (%)**	**Co%**
EM1	6	21	61	12	-
EM2	4	15	44	37	-
EM3	41,56	18,01	20,36	-	20,07

3.1.3 Characterization of the M4, M5 and M6 Group

- **Elemental Analysis of the M4, M5 and M6 Group**

The elemental analysis results for the M4, M5, and M6 from **Table 3.6** indicate the successful synthesis of these frameworks, with slight deviations between the theoretical and experimental values.

For M4, the experimental carbon content (36.43%) is slightly higher than the theoretical value. This difference could be due to residual organic solvent or minor impurities, which contribute to the overall carbon content. The small deviation in hydrogen content (1.11%) is within acceptable limits and suggests successful framework formation. The absence of nitrogen, both theoretically and

experimentally, aligns with the absence of nitrogen-containing ligands or solvents in the synthesis.

The experimental values of M5 show a minor decrease in carbon content (58.22%) which could be due to slight decomposition of the organic linker or loss of guest molecules during the synthesis or analysis process. The hydrogen content (2.89%) also shows a slight reduction, which may be attributed to solvent loss or framework degradation. The nitrogen content (3.11%) is consistent with the presence of DMF as a guest molecule, indicating successful coordination of the DMF solvent to the zinc-based framework.

For M6, the experimental carbon content (53.35%) is slightly lower than the theoretical value, suggesting that there may have been some loss of organic components during the synthesis process. The hydrogen content (3.52%) and nitrogen content (5.01%) both show small deviations from the theoretical values, which may indicate that the DMF guest molecules were partially retained but not completely coordinated within the framework.

Table 3.6. Theoretical calculated value of the M4, M5 and M6 group

Produced MOF	***Molecular Formula***	***Molecular Weight (g/mol)***	***Theoretical (%) C, (%) H, (%) N***	***Experimental (%) C, (%) H, (%) N***
M4	$C_{18}H_6Cu_3O_{12}$ $Cu_3O_{12}(BTC)_2$	604.87	C:35.74% H:1,01%	C:36.43% H:1,11%
M5	$C_{18}H_6Zn_2C_3H_7NO$ $Zn_2(BTC)2.DMF$	426.101	C:59.2% H:3.08% N:3.29%	C:58.22% H:2.89% N:3.11%
M6	$C_{18}H_6Co_3C_6H_{14}N_2O$ $Co_3(BTC)_2.(DMF)_2$	529.237	C:54.47% H:3.81% N:5.29%	C:53.35% H:3.52% N:5.01%

- **Spectroscopic Analysis (FT-IR) of the M4, M5 and M6 Group**

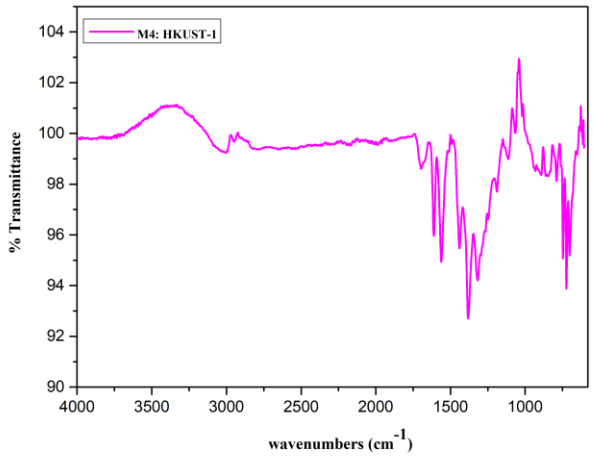
Characteristic peaks are observed in the FTIR spectrum of trimesic acid, which is a precursor ligand. Significant differences in the FTIR spectrum of M4 from **Fig.3.9.a** are observed when compared to trimesic acid. M5 and M6 show different FTIR characteristics in comparison to the original HKUST-1. The absorption of a wide peak around 3500-2500 cm^{-1} in the precursor ligand is due to O-H stretching vibrations, which suggest the presence of carboxylic acid groups [155]. An insignificant high point near 2900 cm^{-1} is due to stretching vibrations of C-H bonds in aliphatic or aromatic compounds. Furthermore, Peaks around 1800 cm^{-1} are probably caused by C=O stretching vibrations originating from the carboxylic acid groups [156]. Elevations around 1500 cm^{-1} suggest C=C stretching vibrations stemming from the aromatic ring.

When copper(II) ions are coordinated to create M4, the FTIR spectrum displays alterations that suggest the formation of the framework (**Fig.3.9.a)**. The decrease in prominence of the wide peak indicates that O-H groups are participating in coordination with copper. The peak for C-H stretching stays, but its strength might vary because of the development of the framework. Changes in peak positions in the 1800s and 1500s cm^{-1} range indicate that the C=O stretching vibrations move towards lower frequencies, indicating the binding of carboxylate groups to copper(II) ions. Changes in the aromatic ring environment due to metal coordination are indicated by new peaks or shifts in the 1500 cm^{-1} range.

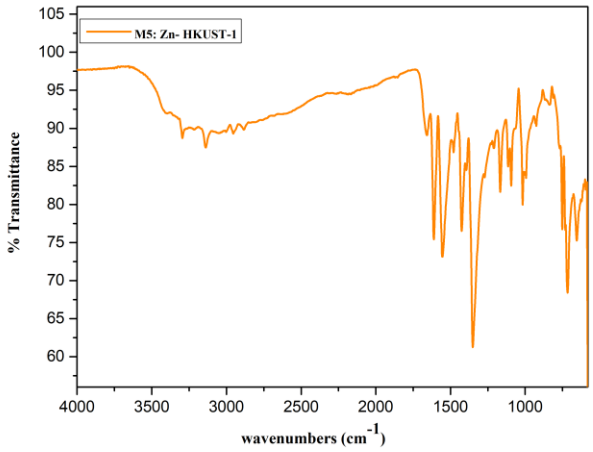
Using zinc(II) acetate instead of copper results in an FTIR spectrum that is similar to HKUST-1 but with some differences as shown from **Fig.3.9.b**. The wide peak for O-H stretching (3500-2500 cm^{-1}) remains present, suggesting the presence of residual or coordinated water molecules. The C-H stretching peak (at approximately 2900 cm^{-1}) persists, potentially showing different levels of intensity because of zinc coordination [147]. The C=O stretching vibrations exhibit a shift that is comparable to HKUST-1 but could differ slightly because of the various metal-ligand interactions with zinc. The presence of peaks around 1500 cm^{-1} suggest alterations in the aromatic ring surroundings due to bonding with zinc ions [151]. The general framework remains intact, showing the successful creation of the M5 structure (**Fig.3.9.b)**.

When cobalt(II) nitrate is substituted for copper, the FTIR spectrum displays unique characteristics for M6 **Fig.3.9.c**. The wide O-H stretching peak could still show up, suggesting leftover or bound water. The C-H stretching peak persists, possibly with different strength because of cobalt coordination. The shifts in C=O stretching vibrations mirror those in M4, showing carboxylate groups coordinating with cobalt(II) ions. Changes in the aromatic ring environment due to cobalt coordination are observed in peaks around 1500 cm^{-1} [157]. A comparison with M4 and M5 will highlight shifts in the carboxylate peaks due to cobalt coordination, and the DMF peak will confirm its presence. The Co-O interaction show up clearly in the low wavenumber region.

a)



b)



c)

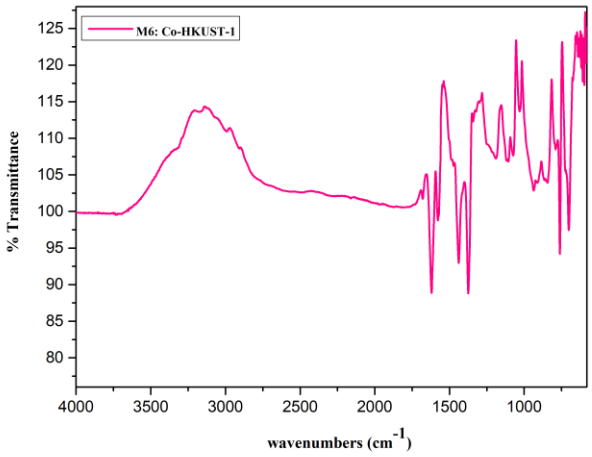


Figure 3.9. The FTIR spectrum of **a)** ligand Trimesic Acid (BTC) **b)** M4 **c)** M5 and **d)** M6

- **Surface Area Calculations (BET) of the M4, M5 and M6 Group**

Table 3.7. shows that M4 demonstrates a reasonable surface area for a copper-based MOF. The moderate pore diameter of 3.72 nm suggests a somewhat open structure, which facilitate access to the internal surface. Although smaller than some copper MOFs reported in the literature, M4's surface area and pore size still position it as a promising material for gas adsorption, separation, or catalysis, particularly where moderately sized molecules are involved.

M5 shows a very low surface area, which could be the result of framework instability, pore collapse, or incomplete activation **(Table 3.7).** The relatively large pore diameter (5.36 nm), however, suggests that while the surface area is low, the structure remains open enough to accommodate larger molecules.

As the **Table 3.7** says the low surface area of M6 is similar to that of M5, likely due to issues during the synthesis process, such as pore collapse or solvent retention. However, the very large pore diameter (10.60 nm) indicates that the framework is significantly more open than expected. While the surface area is limited, M6 still be useful in applications where the ability to transport or adsorb larger molecules is crucial, such as in catalysis or adsorption of bulky organic compounds.

Table 3.7. BET Surface area results of the M4, M5 and M6 group

Produced MOF	***BET Surface Ara***	***Single point adsorption total pore volume***	***Adsorption average pore diameter***	***BJH Adsorption average pore width***	***Average Particle Size***
M4	126,1109 m^2/g	0,117146 cm^3/g	3,7156 nm	4,7779 nm	47,5772 nm
M5	2,2403 m^2/g	0,003001 cm^3/g	5,3579 nm	6,4698 nm	2.678,1923 nm
M6	8,7096 m^2/g	0,023085 cm^3/g	10,6022 nm	35,5274 nm	688,8923 nm

- **Thermal Analysis (TG-DTA) of the M4, M5 and M6 Group**

The characterization and understanding of the modifications induced by ethylenediamine (ED) in HKUST-1 for supercapacitors involve thermal analysis. Thermogravimetric Analysis (TGA) measures weight changes of a substance with temperature. Comparing TGA results from **Fig.3.10** between M4, M5 and M6 may reveal differences in their thermal stability and composition.

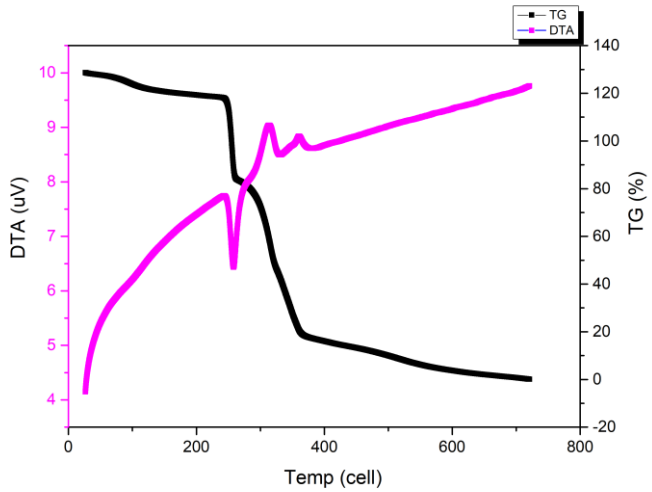
TGA curves show shifts in the decomposition peaks or multiple degradation steps compared to M4 **(Fig.3.10.a).** These shifts may suggest the presence of additional functional groups due to ED modification affecting the thermal decomposition behavior. M4's TGA profile likely shows weight loss in multiple stages, corresponding to the removal of solvents and decomposition of the organic linker. The weight loss stages align with the expected decomposition of copper-based MOFs, with stable retention up to a certain temperature before complete degradation.

From **Fig.3.10.b,** M5 have a TGA profile indicating significant weight loss, especially due to the framework's instability. The low surface area observed in BET analysis suggests potential structural issues, which also be reflected in the TGA profile. The experimental carbon content closely matches the theoretical value implying accurate composition. The significant weight loss before complete

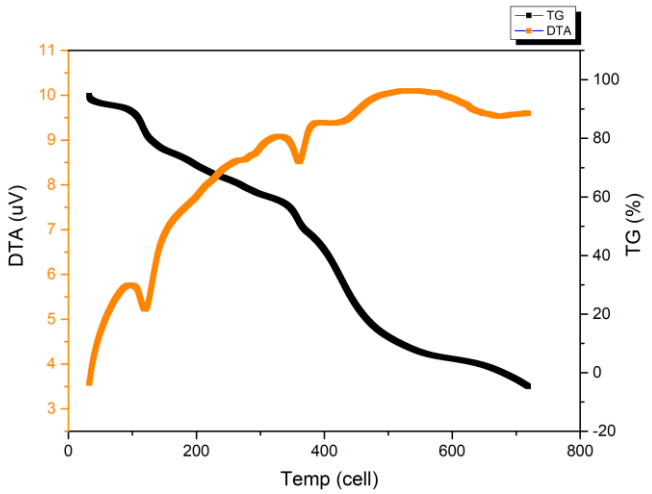
degradation reflects the MOF's instability, possibly due to a compromised framework structure.

M6 show substantial weight loss in stages, indicative of solvent removal and decomposition of the organic linker as it can be seen from **Fig.3.10.c**. The experimental carbon conten which is due to partial decomposition or loss of organic components. The TGA profile considerable weight loss corresponding to the degradation of the MOF structure, consistent with the observed low surface area from BET analysis.

a)



b)



c)

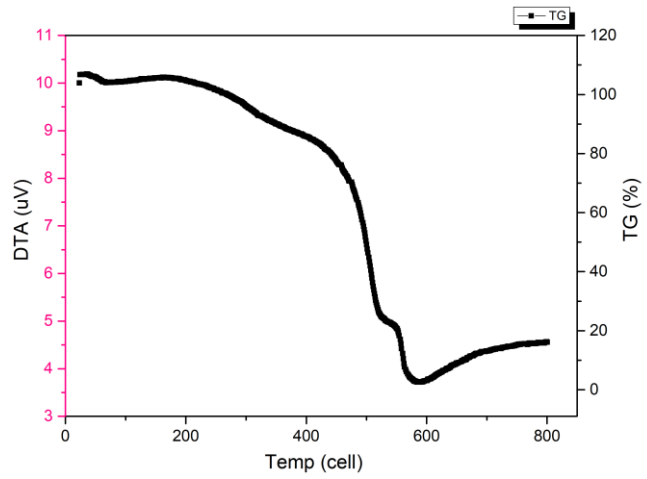


Figure 3.10. The thermal analysis of synthesized **a)** M4 **b)** M5 and c**)** M6

- **Structural Analysis (XRD) of the M4, M5 and M6 Group**

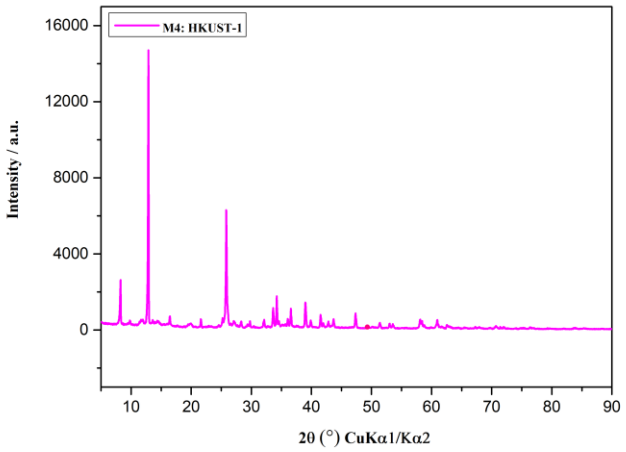
The crystalline nature of M4 is confirmed by the presence of characteristic peaks at 8°, 12°, 25°, and 34° in its XRD pattern as can be seen from **Fig. 3.11.a**. These peaks are representative of the distinct crystallographic planes present in the M4 framework, demonstrating the successful creation of the desired MOF structure. The existence of distinct and strong peaks indicates a significant level of crystallinity, which is crucial for the material to function effectively in various applications [110].

The crystalline framework of M5 from **Fig. 3.11.b** is demonstrated by distinct peaks observed at 8°, 14°, 18°, 23°, 26°, 30°, and 38° in the XRD pattern. The change and emergence of extra peaks in contrast to HKUST-1 indicate that the introduction of zinc into the structure causes minor alterations in the crystal lattice [109]. These variances might stem from differences in how metals interact with ligands and their surroundings when zinc(II) acetate is substituted for copper. The existence of numerous distinct peaks indicates that M5 retains a high level of crystallinity, which is essential for upholding its porosity and structural integrity in diverse uses.

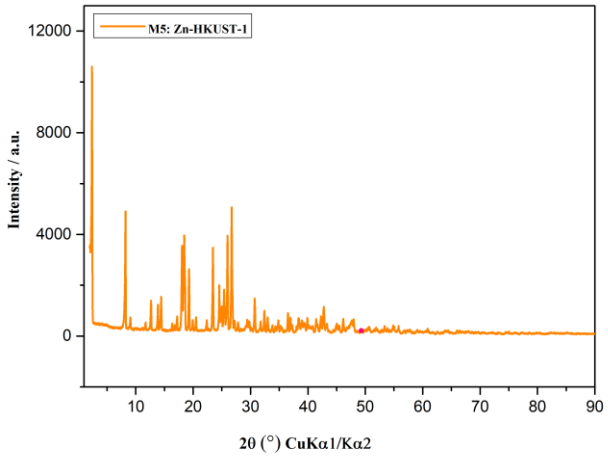
Fig. 3.11.c shows that the XRD analysis validates that the crystalline metal organic frameworks M6 were successfully synthesized. The individual peaks seen in the X-ray diffraction patterns represent the distinct crystal structures of every MOF. The change in peak positions and the emergence of additional peaks in Zn-HKUST-1,

as opposed to HKUST-1, suggest that replacing metal centers impacts the crystal lattice. These results indicate that the structures of the frameworks remain crystalline in nature even as they incorporate various metal ions, resulting in potential changes in their physical and chemical characteristics[158].

a)



b)



c)

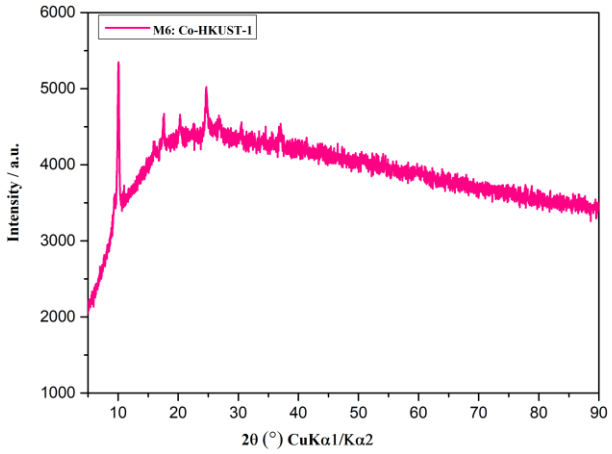
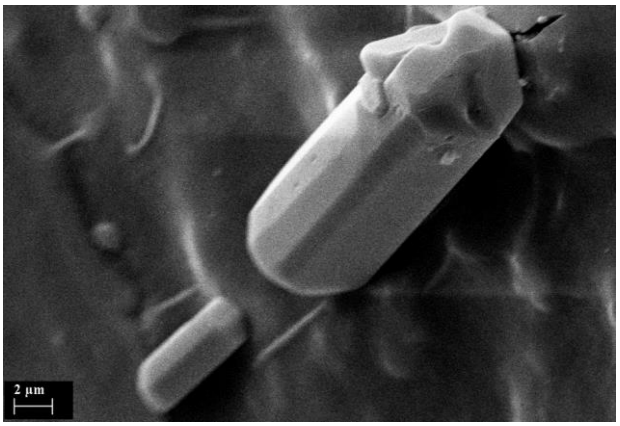


Figure 3.11. The XRD pattern of synthesized **a)** M4 **b)** M5 and **c)** M6

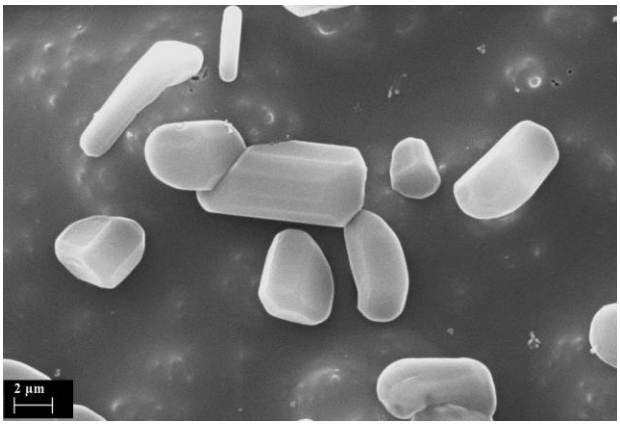
- **Morphological Analysis (SEM and EDS) of the M4, M5 and M6**

The modification with ethylenediamine, despite potentially reducing the pore size of the MOF, serves specific purposes that can outweigh the pore size reduction **(Fig.3.12).** ED modification introduces functional groups onto the HKUST-1 surface, enhancing its interaction with electrolyte ions [117]. This improved interaction lead to better charge storage and faster ion transport, compensating for the reduced pore size by facilitating more efficient utilization of the surface area.

a)



b)



c)

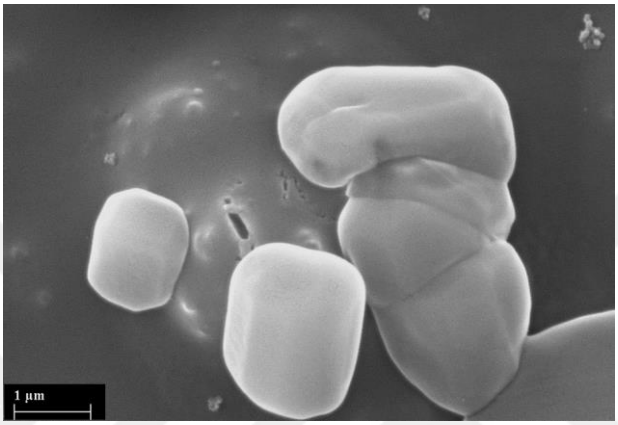


Figure 3.12. The SEM image of synthesized **a)** M4 at 5000x magnification **b)** M5 at 5000x magnification and c**)** M6 at 10000x magnification

The SEM images of M4 and M5 from **Fig.3.12** reveal a more bulky and less defined structure compared to other MOFs in the series. Although the overall morphology appears less refined, the hexagonal structures characteristic of HKUST-1 are still visible. This suggests that while the MOF exhibits a bulkier appearance, the fundamental hexagonal framework of the Zn-based MOF has been preserved (**Fig.3.12.b**). The bulkier appearance of M5 could be attributed to variations in synthesis conditions or the inherent properties of the zinc-based framework. Despite the increased bulkiness, the retention of hexagonal shapes indicates that the synthesis process has successfully produced a framework that maintains its fundamental structural elements.

The SEM images for M6 show a notably bulky structure, with less distinct hexagonal features compared to other MOFs as shown in **Fig.3.12.c**. Despite the bulkier morphology, the characteristic hexagonal structures of HKUST-1 are still observable, indicating that the Co-based MOF retains its essential framework. The increased bulkiness of M6 a result of the synthesis parameters or the specific

interactions within the Co-based framework. While the hexagonal structure is present, the overall morphology suggests a departure from the more defined shapes seen in other MOFs. The presence of hexagonal features confirms that the core structural integrity of the MOF is maintained.

The EDS examination of M4 from **Table 3.8.** displays a makeup in line with the expected elements in the HKUST-1 structure. The existence of carbon, nitrogen, oxygen, and copper validates the successful creation of the M4 framework. The arrangement of components corresponds to the stoichiometry needed for HKUST-1, with copper acting as the core metal ion bonded to trimesic acid ligands [159]. The composition of M5 determined by EDS results shows higher levels of carbon and nitrogen in comparison to M4, as well as the existence of oxygen and zinc. The increased carbon and nitrogen levels indicate more organic linkers compared to metal content, showing copper has been replaced with zinc. The reduced zinc levels in M4 compared to copper indicate the planned substitution and demonstrate the effective integration of zinc into the M4 structure [160]. The results show that M5 maintains its basic structure while incorporating zinc as the main metal ion, which could change its chemical and physical characteristics when compared to M4.

Table 3.8. EDS analysis results of the M4, M5 and M6 group

Produced MOF	**C (%)**	**N (%)**	**O (%)**	**Zn (%)**	**Co%**	**Cu%**
M4	25,56	03,48	37,57	-	-	33,39
M5	41,77	08,28	37,80	12,15	-	-
M6	36,41	05.33	35,45	-	22,81	-

3.1.4 Characterization of the ED modified EM4, EM5 and EM6 Group

- **Elementalal Analysis of the ED modified Em4, EM5 and EM6 Group**

For the M4, M5, and M6 series, the deviations between theoretical and experimental values are relatively minor, indicating that the frameworks were synthesized successfully with minimal loss of organic components or solvent **(Table 3.9).** The incorporation of ethylenediamine confirmed by the significant increase in nitrogen content, with small deviations suggesting that the ethylenediamine was not fully incorporated.

For EM4 the experimental nitrogen content (9.89%) indicates that ethylenediamine has been successfully incorporated into the MOF structure, though in slightly lower quantities than theoretically expected. The carbon content (35.63%) and hydrogen content (3.42%) are both slightly lower than the theoretical values, likely due to the incomplete incorporation of ethylenediamine or partial loss during the synthesis. Overall, these results confirm that ethylenediamine has been integrated, albeit with some deviation from the theoretical values.

For EM5 the experimental carbon content (52.25%) is slightly lower than the theoretical value, possibly due to incomplete retention of the organic ligands or loss of DMF during the synthesis. The hydrogen (6.01%) and nitrogen (15.82%) contents are close to the theoretical values, indicating that ethylenediamine has been well-incorporated into the framework. The minor deviations may be attributed to the partial retention of guest molecules or slight framework degradation.

The experimental values for EM6 show a small decrease in carbon content (52.56%), which may be due to the loss of organic components during synthesis or incomplete ethylenediamine incorporation. The hydrogen content (5.95%) and nitrogen content (8.01%) are both slightly lower than the theoretical values, possibly indicating partial solvent loss or incomplete ethylenediamine binding within the framework. However, the overall nitrogen increase confirms the successful ethylenediamine modification.

Table 3.9. Theoretical calculated value of the EM4, EM5 and EM6 group

Produced MOF	*Molecular Formula*	*Molecular Weight (g/mol)*	*Theoretical (%) C, (%) H, (%) N*	*Experimental (%) C, (%) H, (%) N*
EM4	$C_{18}H_6Cu_3O_{12}C_6H_{24}N_6$ $Cu_3O_{12}(BTC)_2.(ED)_3$	785.172	C:36.71% H:3.85% N:10.71%	C:35.63% H:3.42% N:9.89%
EM5	$C_{18}H_6Zn_2C_3H_7NOC_6H_{24}N_6$ $Zn_2(BTC)_2.DMF.(ED)_3$	606.401	C:53.48% H:6.15% N:16.17%	C:52.25% H:6.01% N:15.82%
EM6	$C_{18}H_6Co_3C_6H_{14}N_2OC_4H_{18}N_2$ $Co_3(BTC)_2.(DMF)_2.(ED)_2$	623.439	C :53.94% H:6.14% N:8.99%	C:52.56% H:5.95% N:8.01%

- **Spectroscopic Analysis (FT-IR) of the ED modified EM4, EM5 and EM6 Group**

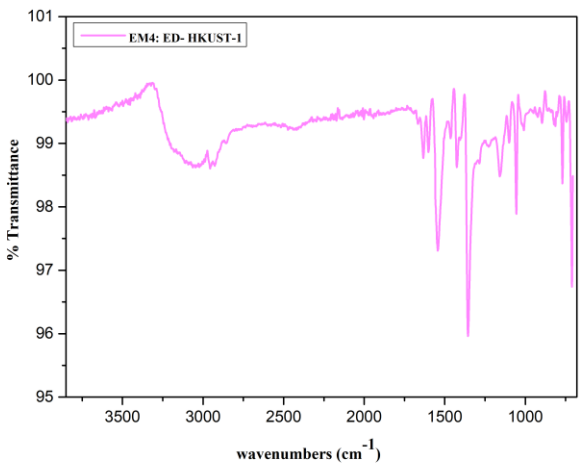
The FTIR spectra show specific differences between ethylenediamine-modified EM4, EM5 and EM6 compared to the unmodified versions **(Fig.3.13).** The emergence of a fresh peak at approximately 3500 cm^{-1} indicates that there are N-H stretching vibrations from ethylenediamine molecules present, showing that ED has been effectively integrated into the MOF structure. This particular peak is a signature of the amine functional group added by ethylenediamine, which bonds with the metal centers and organic linkers found in the MOF framework.

Along with the new N-H stretching peak, the FTIR spectra of ED-modified MOFs exhibit the unique peaks seen in the original M4, M5 and M6 **(Fig.3.13).** This consists of vibrations related to O-H stretching, peaks from C-H stretching, and

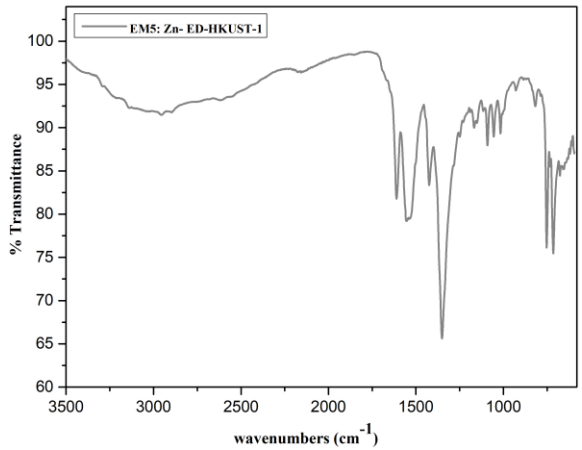
changes in the stretching regions of C=O and C=C, showing the coordination of metal with ligands and integrity of the overall framework [68]. Both metal substitution and ethylenediamine incorporation have an impact on the structural and chemical properties of the frameworks, as illustrated by the similarities and differences in FTIR spectra among these MOFs.

The FTIR results are similar to unmodified ones, but with new bands from ethylenediamine N-H stretching around 3300-3200 cm^{-1} and C-N stretching around 1250-1350 cm^{-1} has shown. As with the other ethylenediamine-modified MOFs, you would expect to see new peaks in the N-H and C-N regions that are absent in unmodified ones and Shifts in the carboxylate bands due to the presence of ethylenediamineto the metal **(Fig.3.13).** The successful incorporation of ethylenediamine will be confirmed by the appearance of N-H and C-N stretching bands. As with EM4 and EM5, the shifts in carboxylate stretching will further confirm the ethylenediamine interaction with cobalt.

a)



b)



c)

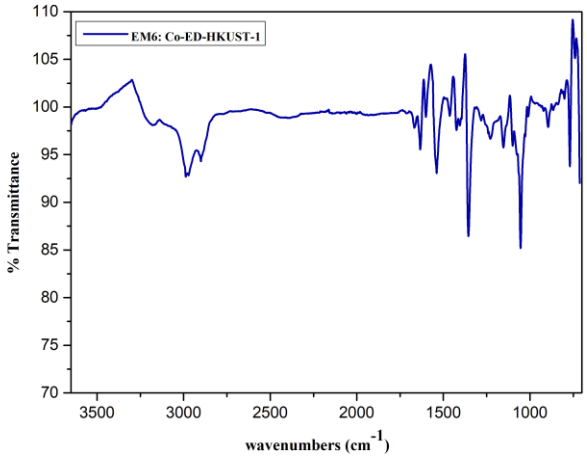


Figure 3.13. The FTIR spectrum of synthesized **a)** EM4 **b)** EM5 and **c)** EM6

- **Surface Area Calculations (BET) of the ED modified EM4, EM5 and EM6 Group**

Table 3.10 for EM4 demonstrates a significant improvement in surface area compared to its unmodified counterpart (M4), likely due to the ethylenediamine modification opening up additional surface sites. The pore diameter remains moderate at 3.16 nm, which suggests that the ethylenediamine has not caused significant pore blockage. This combination of high surface area and moderate pore size makes EM4 a strong candidate for applications in catalysis and adsorption, where both surface accessibility and pore size are important [161].

In contrast, EM5 shows a significantly lower BET surface area and a much smaller total pore volume. The surface area of EM5 remains low after modification, similar to its unmodified counterpart (M5). However, the pore diameter remains large at 5.35 nm, which suggests that the framework is still accessible for larger molecules. The larger pore diameter of 5.3507 nm and wider pore width of 8.1586 nm suggest structural changes possibly due to the incorporation of zinc and ethylenediamine. The average particle size of 2087.8654 nm indicates larger particle dimensions compared to EM4. Although the surface area is limited, the open pore structure could make EM5 useful in applications requiring diffusion of larger molecular species **(Table 3.10).**

EM6 exhibits an extremely low surface area, likely due to severe pore collapse or structural defects introduced during modification. The extraordinarily large pore diameter (531.41 nm) suggests that the framework has collapsed into large voids or interparticle spaces, which would account for the minimal surface area.

Table 3.10. BET Surface area results of the of the EM4, EM5 and EM6 group

Produced MOF	***BET Surface Ara***	***Single point adsorption total pore volume***	***Adsorption average pore diameter***	***BJH Adsorption average pore width***	***Average Particle Size***
EM4	278,2781 m^2/g	0,219603 cm^3/g	3,1566 nm	4,4680 nm	21,5612 nm
EM5	2,8737 m^2/g	0,003844 cm^3/g	5,3507 nm	8,1586 nm	2.087,8654 nm
EM6	0,0165 m^2/g	0,002188 cm^3/g	531,4081 nm	36,3818 nm	364.304,3480 nm

- **Thermal Analysis (TG-DTA) of the ED modified EM4, EM5 and EM6 Group**

ED modification might alter the thermal stability of HKUST-1. The observed variations in the onset temperature of decomposition, indicating changes in the material's resistance to thermal degradation [119].

In **Fig.3.14.a,** EM4's TGA profile show weight loss in stages, reflecting the thermal decomposition of the framework and additional losses due to ethylenediamine. The high surface area observed in BET analysis suggests that the MOF maintains a robust structure. The experimental carbon content is slightly lower than the theoretical value, indicating potential alterations due to modification. The TGA results demonstrate the stability of the framework up to higher temperatures, with clear stages of decomposition.

EM5 exhibit a complex TGA profile with additional weight loss due to ethylenediamine **(Fig.3.14.b)**. The low surface area from BET analysis suggests that the modification might affect the framework's stability. The elemental analysis indicating that the composition is largely preserved. The TGA profile reflect the additional degradation stages corresponding to the ethylenediamine, with overall stability compared to the unmodified MOF.

Fig.3.14.c shows that EM6's TGA profile show weight loss due to both the framework and ethylenediamine modification. The extremely low surface area observed suggests severe structural collapse or instability. The drastic decrease in surface area and very large pore diameter indicate possible severe degradation or collapse of the framework. The TGA results confirm substantial decomposition with possible formation of large voids or structural breakdown.

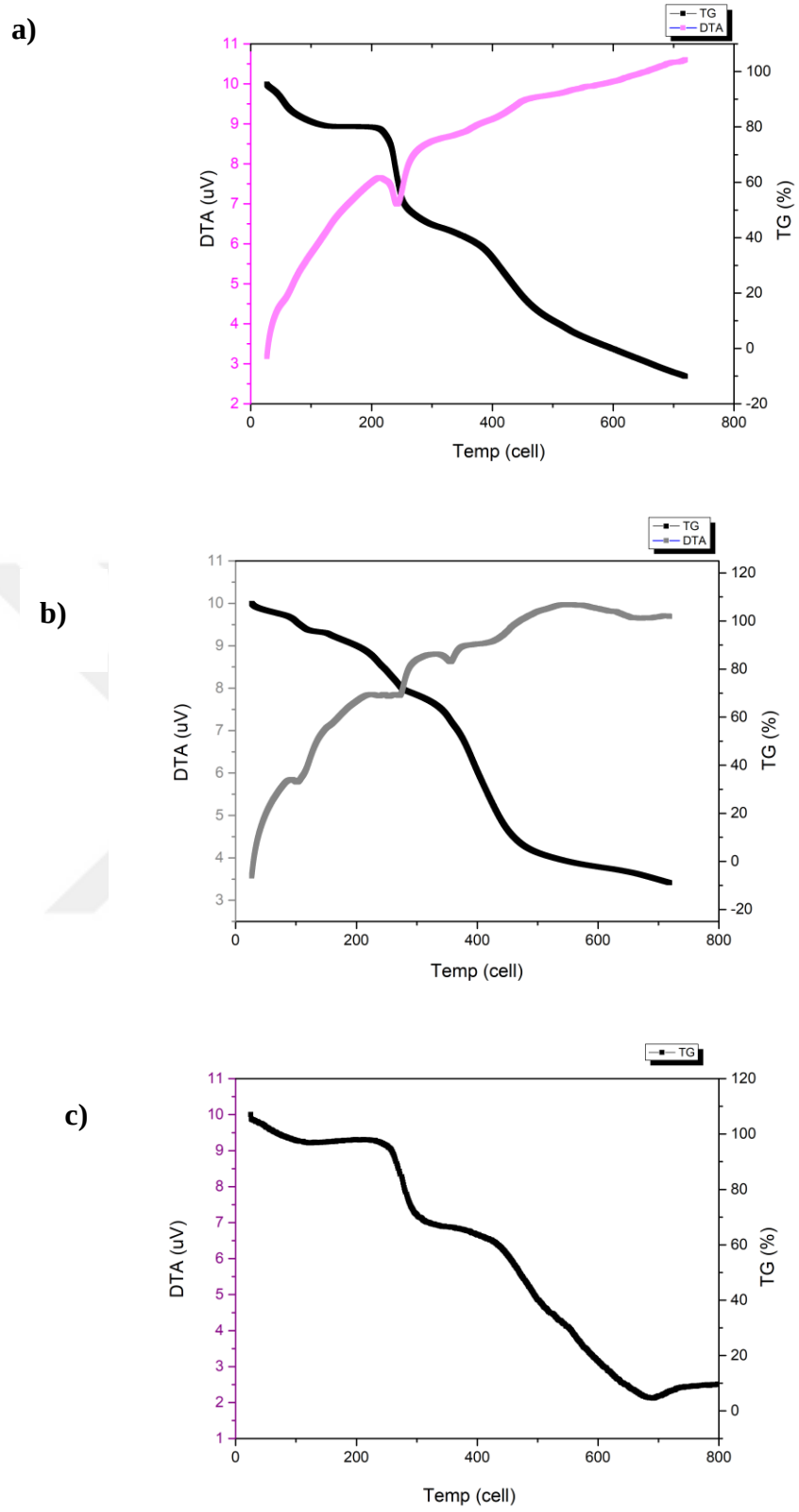


Figure 3.14. The thermal analysis of synthesized **a)** EM4 **b)** EM5 and **c)** EM6

ED modification influences the residual mass at higher temperatures after decomposition. Changes in the amount of residue left after degradation may imply

alterations in the chemical composition or the formation of new compounds or residues due to the modification.

TGA analysis reveal distinct decomposition steps or phases in the modified HKUST-1 that differ from the unmodified form. This could indicate changes in the degradation pathways or the presence of new component [162]. Differences in weight loss profiles between modified and unmodified M4 could suggest variations in the presence of volatile components, functional groups, or structural modifications induced by ED.

- **Structural Analysis (XRD) of the ED modified EM4, EM5 and EM6 Group**

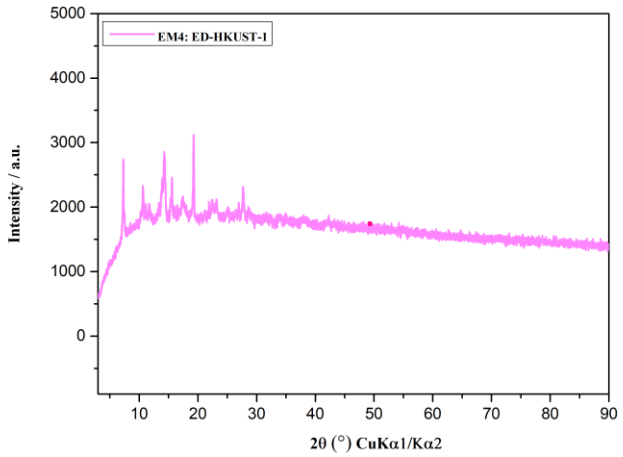
In this work, ED modification were expected to show lead to shifts in diffraction peaks or changes in peak intensities compared to unmodified HKUST-1. This could indicate alterations in the crystal lattice structure or unit cell parameters due to the introduction of ED. However, modifications in the crystal structure induced by ED showed similar of specific peaks in ED-modified EM4 compared to unmodified M4 indicate similarities in the crystalline phase (M6: °2θ: 26.5872 and EM6: °2θ: 26.6199). The formation of new phases due to the modification influence the overall crystallinity of EM4 **(Fig.3.15.a).** A small change in the XRD pattern, indicating changes in the ordered arrangement of atoms within the crystal lattice [99].

EM5's XRD pattern from **Fig.3.15.b** show less distinct peaks compared to its non-modified counterpart, reflecting the influence of ethylenediamine on the crystal structure. While characteristic peaks present, they might be broadened or less intense, indicating possible structural modifications. The presence of crystalline peaks, suggests that the ethylenediamine modification has led to some changes in the crystal lattice but has not completely amorphized the material. This indicates that EM5 retains its crystalline nature but with possible alterations in the structure.

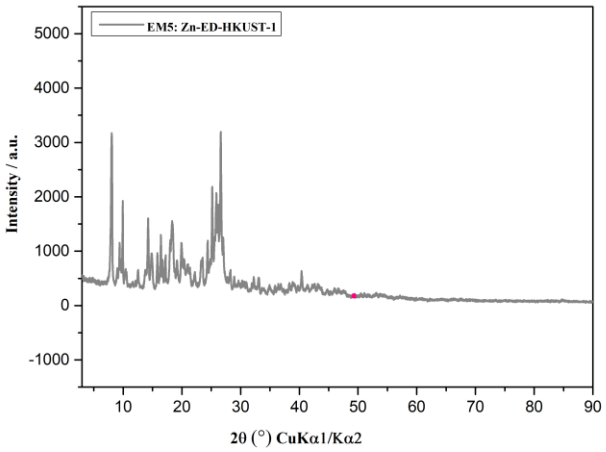
For **Fig.3.15.c** EM6, the XRD pattern show broad or less distinct peaks compared to the unmodified Co-based MOF. This suggests that while EM6 remains crystalline, the incorporation of ethylenediamine has led to modifications in the crystal structure. Although the characteristic peaks of the MOF may not be as sharp or well-defined, the presence of any peaks confirms that EM6 is crystalline. The

broadening or shifting of peaks indicates structural changes due to the modification but does not imply complete loss of crystallinity.

a)



b)



c)

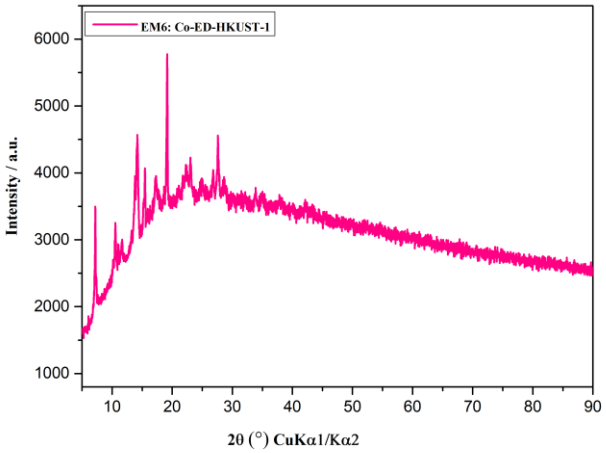


Figure 3.15. The XRD pattern of synthesized **a)** EM4 **b)** EM5 and **c)** EM6

Peaks corresponding to the presence of functional groups introduced by HKUST-1 be observed. However, effect of ED might be challenging to identify solely through XRD unless the changes significantly affect the crystal structure.

- **Morphological Analysis (SEM and EDS) of the ED modified EM4, EM5 and EM6 Group**

SEM provides surface morphology information, revealing changes in surface texture and particle size after modification.

ED modification allows for the tailoring of the MOF's surface chemistry, potentially creating new active sites or altering the nature of existing ones [28]. This alteration can positively impact specific capacitance and charge storage mechanisms, even with a reduced pore size.

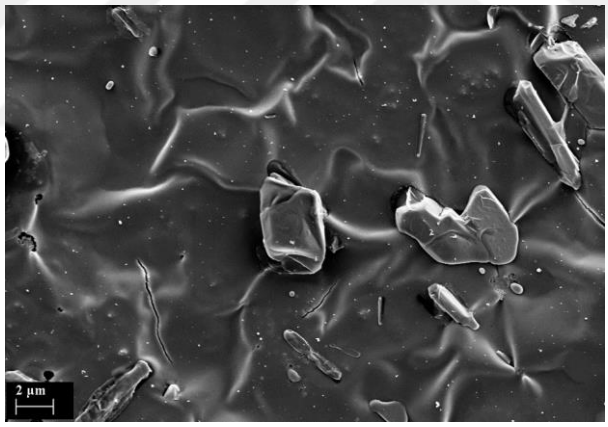
The SEM images of EM4 from **Fig.3.16.a** reveal a well-defined structural shape characteristic of HKUST-1, reflecting the successful incorporation of the 1,3,5-Benzenetricarboxylic Acid ligand and copper. The morphology of EM4 closely resembles that of the non-modified HKUST-1, demonstrating that the ethylenediamine modification has not significantly altered the overall shape of the MOF. The presence of ethylenediamine is expected to enhance the stability of EM4, as evidenced by its well-maintained structural integrity. The modification likely contributes to improved mechanical and chemical stability, ensuring that the MOF retains its structural form even under stress. The improved acid resistance of the ethylenediamine-modified EM4 is due to the heightened stiffness and durability of the structure. The addition of ethylenediamine may also bring about extra hydrogen bonding and interactions in the structure, thus enhancing its stability [68].

Fig.3.16.b EM5 exhibits a well-preserved structural shape similar to HKUST-1, reflecting the successful synthesis with the 1,3,5-Benzenetricarboxylic Acid ligand and zinc. The structural morphology of EM5 remains consistent with the expected HKUST-1-like framework, indicating that ethylenediamine has not disrupted the overall form of the MOF.The ethylenediamine modification in EM5 enhances its stability compared to non-modified counterparts. The improved stability is evident from the retention of its structural shape, suggesting that ED has contributed to maintaining the framework's integrity.

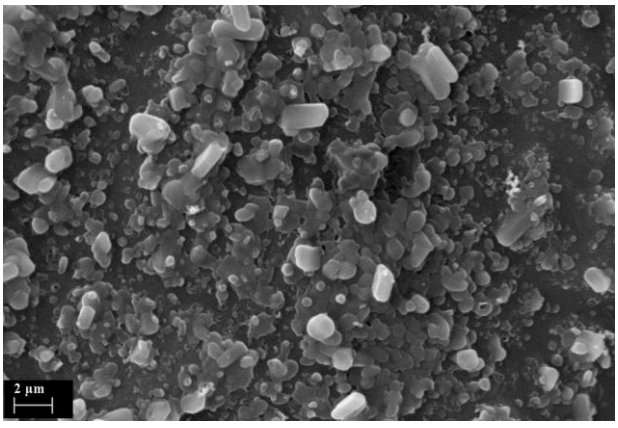
The SEM images for EM6 from **Fig.3.16.c** show a strong resemblance to the HKUST-1 structure, indicating that the incorporation of ethylenediamine has preserved the characteristic morphology of the Co-based MOF. The consistency in shape suggests successful synthesis and structural maintenance. Ethylenediamine modification in EM6 has likely enhanced its stability. The well-preserved structural shape and morphology of EM6 imply that the ED treatment has effectively reinforced the MOF framework, contributing to improved mechanical and chemical stability.

These results indicate that the transformation of ethylenediamine not only changes the way the HKUST-1 material breaks down but also greatly enhances its ability to withstand high temperatures. This enhanced stability is beneficial for possible uses in which thermal resistance is vital, like in catalysis, gas storage, and separation procedures. The capacity to alter and improve the thermal characteristics of MOFs via chemical modifications creates opportunities for creating new materials with customized properties.

a)



b)



c)

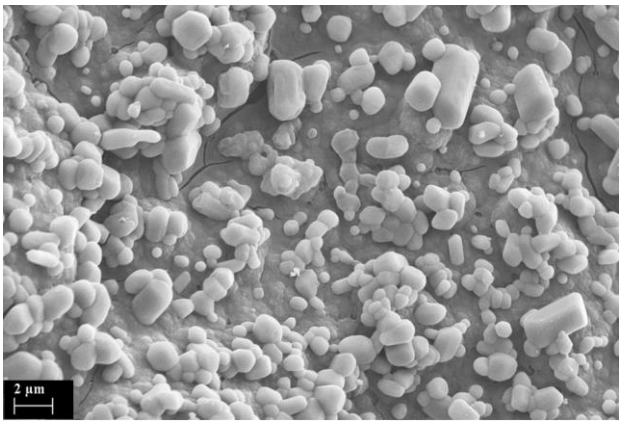


Figure 3.16. The SEM image of synthesized **a)** EM4 at 5000x magnification **b)** EM5 at 10000x magnification and **c)** EM6 at 10000x magnification

Table 3.11. EDS analysis results of the EM4, EM5 and EM6 group

Produced MOF	**C (%)**	**N (%)**	**O (%)**	**Zn (%)**	**Co%**	**Cu%**
EM4	41,14	19,19	21	-	-	18,67
EM5	40,83	18,31	21,77	19,09	-	-
EM6	39,78	21,10	18,97	-	20,15	-

ED modification introduces amine functional groups onto the HKUST-1 surface, potentially improving its interaction with electrolyte ions and facilitating faster charge transfer kinetics. ED contains amine groups that can interact with the Co ions and the ligands of the M4 framework **(Table 3.11)**. This interaction leads to the functionalization of the material's surface with these amine groups. The addition of these functional groups alters the surface chemistry of HKUST-1, affecting its interaction with electrolyte ions during the charge-discharge process in supercapacitors [120].

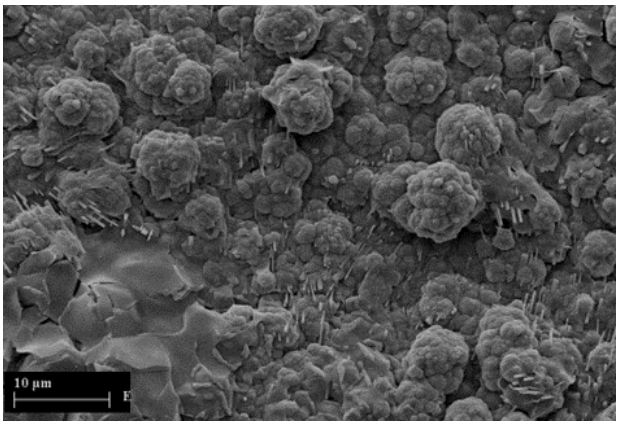
3.2 Characterization of the Prepared Electrodes

In this research, cyclic voltammetry (CV) was employed to study redox reactions for material synthesis and to assess the supercapacitive characteristics of the resulting material [163]. Prior studies focused on fine-tuning important factors like sulfuric acid levels, pyrrole levels, and the number of cycles. At first, CV and EIS were used to investigate how factors like acid concentration, monomer concentration, and cycle number affect electrode capacitance behaviors. Later on, researchers utilized cyclic voltammetry and electrochemical impedance spectroscopy to analyze how changing the mass loading of MOF@/PPy/PGE affected the electrochemical performance of polypyrrole, observing the influence of different substance quantities [93].

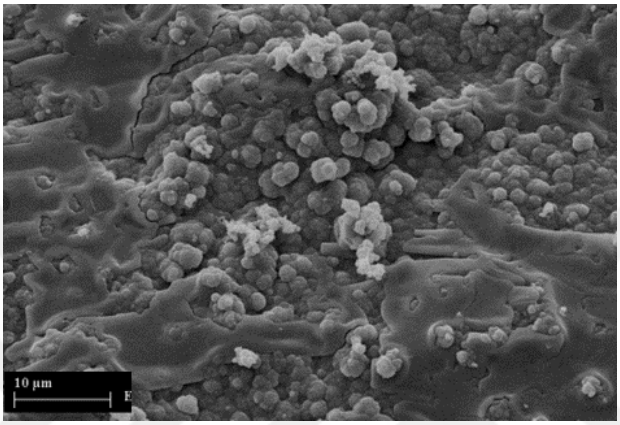
3.2.1 Morphological Characterization of the Electrodes

In this section, the synthesized metal organic frameworks (MOFs), in conjunction with polypyrrole, were integrated onto a carbon electrode (pencil graphite). This study focuses on the morphological and spectroscopic characterization of these composite electrodes [164]. The combination of MOFs and polypyrrole aims to enhance the electrode's properties for potential applications in energy storage and electrochemical sensing. Detailed analysis of the electrode's surface morphology and spectroscopic features provides insights into their structural integrity, surface area, and chemical composition, crucial for optimizing their performance in various electrochemical applications [144].

a)



b)



c)

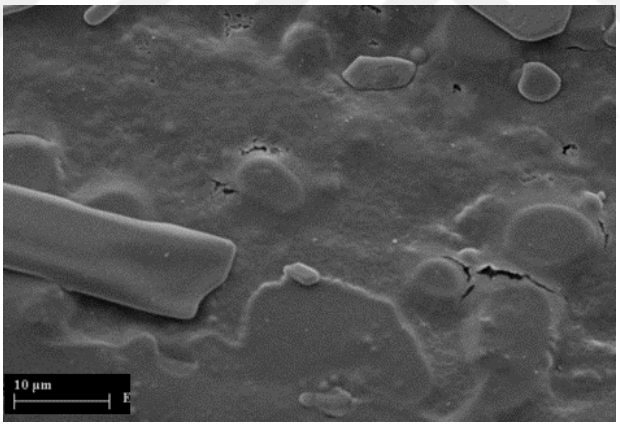


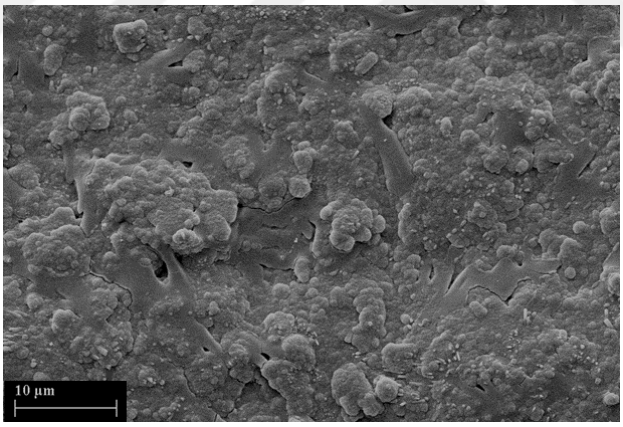
Figure 3.17. The SEM image of electrode PPy/PGE from acid optimisation step: **a)** 0,05 M Acid PPy/PGE **b)** 0,1 M Acid PPy/PGE and **c)** 0,2 M Acid PPy/PGE at 5000x magnification

SEM images of PPy/PGE electrodes from **Fig.3.17** at 5000x magnification reveal distinct morphological differences based on sulfuric acid concentration. Structures resemble a cauliflower morphology characteristic of polypyrrole[165]. For 0.05 M Acid PPy/PGE, SEM analysis at **Fig.3.17.a** shows PPy deposited on PGE electrodes with a visibly bulkier morphology resembling irregular cauliflower structures. The surface appears less uniform compared to optimal conditions. At 0.1 M Acid

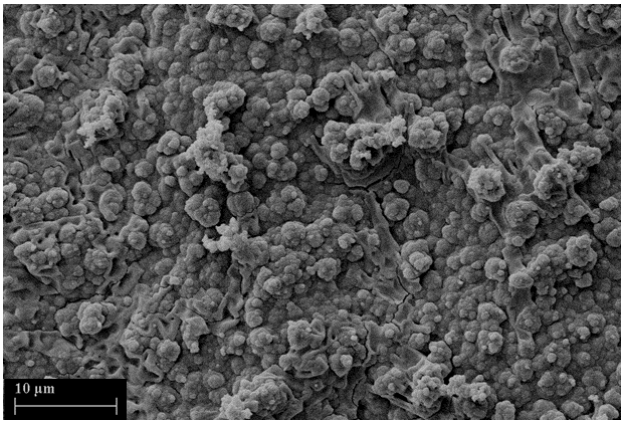
PPy/PGE acid concentration, SEM images exhibit a structure of polypyrrole on the electrode surface can be seen on **Fig.3.17.b**. However, the structure appears slightly more compact and less defined compared to the optimal condition. For 0.2 M Acid PPy/PGE, SEM images reveal a dense, bulky morphology of polypyrrole on PGE electrodes, suggesting a lower surface area and potential aggregation of the polymer (**Fig.3.17.c).**

SEM characterization of PPy/PGE electrodes provides valuable insights into the structural morphology influenced by acid concentration during synthesis [133]. The cauliflower-like structures observed under optimal conditions (1 M acid) indicate an ideal balance between polymer growth and surface area, crucial for applications requiring high conductivity and electrochemical activity as **Fig.3.17** shows. Understanding these morphological features aids in optimizing electrode performance for various electrochemical applications, including sensors and energy storage devices.

a)



b)



c)

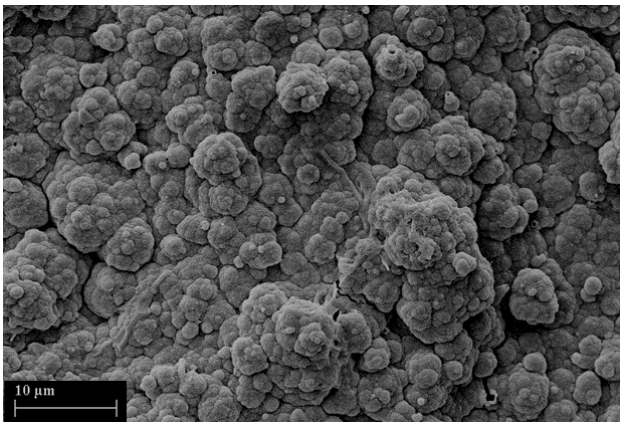
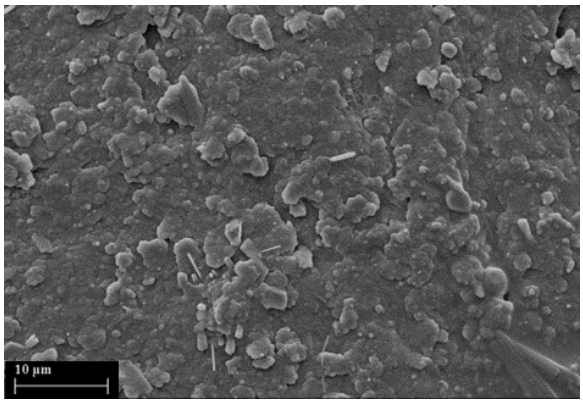


Figure 3.18. The SEM image of electrode PPy/PGE from monomer optimisation step: **a)** 0,05 M Pyyrole PPy/PGE **b)** 0,5 M Pyyrole PPy/PGE and **c)** 2 M Pyyrole PPy/PGE at 5000x magnification

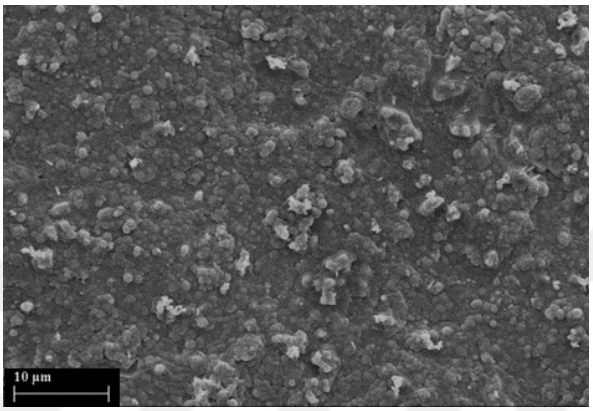
Fig.3.18 indicates the SEM images of PPy/PGE electrodes at 5000x magnification shows variations in morphology based on pyrrole concentration. Optimal structure resembles a well-defined PPy morphology suitable for enhanced surface area [133]. SEM analysis shows PPy deposited on PGE electrodes with a morphology indicating sparse coverage and uneven distribution on 0.05 M Pyrrole PPy/PGE can be seen at **Fig.3.18.a**. The structure appears less compact and uniform. At 0.5 M Pyrrole PPy/PGE pyrrole concentration **Fig.3.18.b**, SEM images reveal a uniform and well-defined structure of polypyrrole on the electrode surface. The morphology resembles a cauliflower-like structure characteristic of PPy with good surface area and interconnected pores. 2 M Pyrrole PPy/PGE, SEM images display a dense and bulky morphology of polypyrrole on PGE electrodes at **Fig.3.18.c**, indicating potential aggregation and reduced surface area compared to optimal conditions.

The SEM analysis of PPy/PGE electrodes under 0.5 M pyrrole concentration shows a favorable morphology with a well-defined PPy structure **(Fig.3.18)**. This structure suggests efficient polymerization and adherence to the electrode surface, resulting in enhanced surface area and conductivity [166].

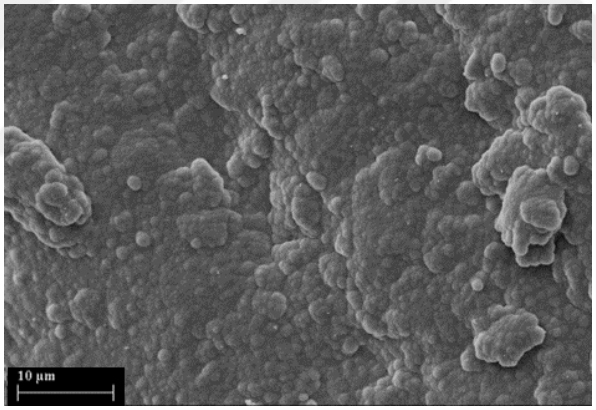
a)



b)



c)



d)

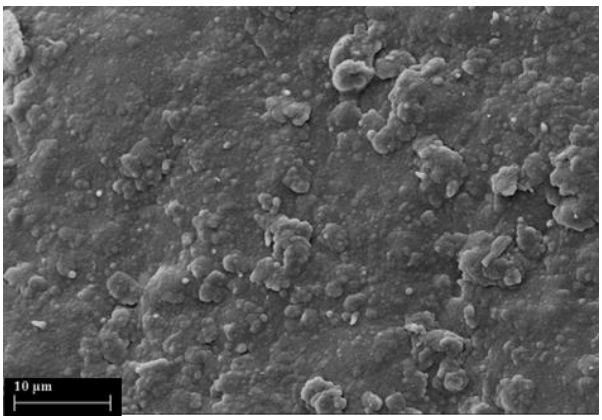


Figure 3.19. The SEM image of electrode PPy/PGE from cycle optimisation step: **a)** 5 cycle PPy/PGE **b)** 10 cycle PPy/PGE **c)** 30 cycle PPy/PGE and d**)** 50 cycle PPy/PGE at 5000x magnification

SEM analysis indicates PPy deposition on PGE electrodes with a morphology suggesting initial stages of polymer growth at **Fig.3.19**. The structure appears less defined with potential areas of uneven coverage. At 10 polymerization cycles **Fig.3.19.b**, SEM images show a more uniform and structured morphology of polypyrrole on the electrode surface. This structure exhibits improved surface area and interconnected pores compared to fewer cycles like **Fig.3.19.a**. 30 Cycle PPy/PGE SEM images display a denser and more compact morphology of polypyrrole on PGE electrodes, indicating increased polymer deposition and potential aggregation (**Fig.3.19.c)**. The structure may show reduced surface area compared to optimal conditions. SEM analysis reveals a bulky and aggregated morphology of polypyrrole on PGE electrodes after 50 cycles of polymerization at **Fig.3.19.d**. The structure appears less uniform with diminished surface area compared to the optimal condition [167].

The SEM analysis of PPy/PGE electrodes after 10 polymerization cycles demonstrates an optimal morphology with a well-defined structure of polypyrrole (**Fig.3.20)**. This structure indicates efficient polymer growth and adherence to the electrode surface, resulting in enhanced surface area and electrochemical performance.

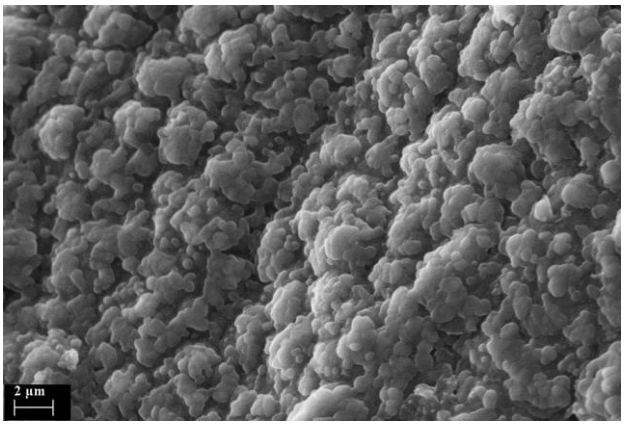


Figure 3.20. The SEM image of the optimum electrode PPy/PGE at 10000x magnification

- **Morphological Analysis of the M1@PPY/PGE, M2@PPY/PGE, M3@PPY/PGE Group**

SEM analysis was conducted to identify the structural characteristics of the electrodes. SEM images of PPy/PGE and M2@PPy/PGE can be seen the typical cauliflower structure of polypyrrole. The addition of M2 altered the morphology of PPy. The presence of M2 in the PPy composition is clearly visible. The inclusion of PPy led to an enhancement in both the active surface area and mesoporous structure of PPy. BET analysis provided backing for this scenario. An increase was detected in the mesoporosity of the PPy. The SEM-EDS analysis confirmed the uniform distribution of M2 within the PPy structure.

The SEM images at **Fig.3.21** reveal a well-dispersed structure of M3 particles within the polypyrrole matrix. The MOF particles are effectively embedded in the conducting polymer, contributing to a highly porous and stable electrode surface.The MOF particles maintain their individual morphology but are surrounded by a continuous and cohesive polypyrrole network. The BET surface area of M3@PPY/PGE is notably high (353.1036 m^2/g), indicating a substantial surface available for electrochemical interactions. This high surface area is complemented by the porous nature observed in the SEM images, which supports enhanced charge storage capabilities (**Fig.3.23)**.The presence of the polypyrrole matrix enhances the dispersion of M3 MOF particles, leading to a more uniform and smooth surface compared to pure MOF materials. This indicates that the electrochemical polymerization has successfully incorporated the MOFs into the polymer structure, improving the overall conductivity and surface characteristics of the electrode.

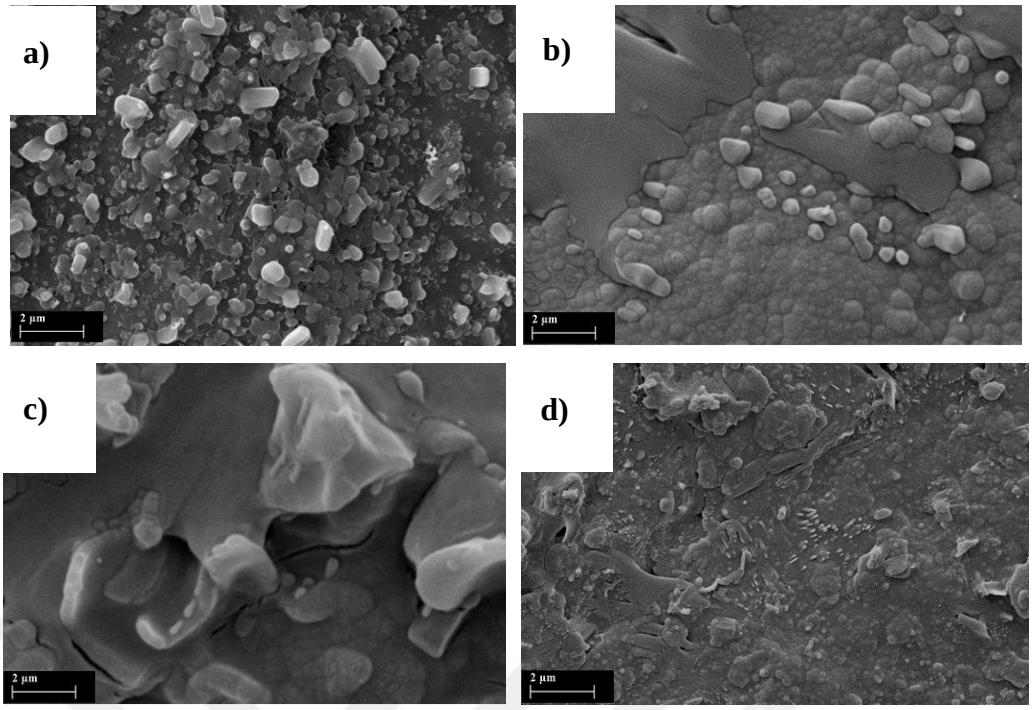


Figure 3.21. The SEM image of M1@PPY/PGEs consisting of **a)**3 mg **, b)**5 mg , **c)**10 mg and **d)** 20 mg M1

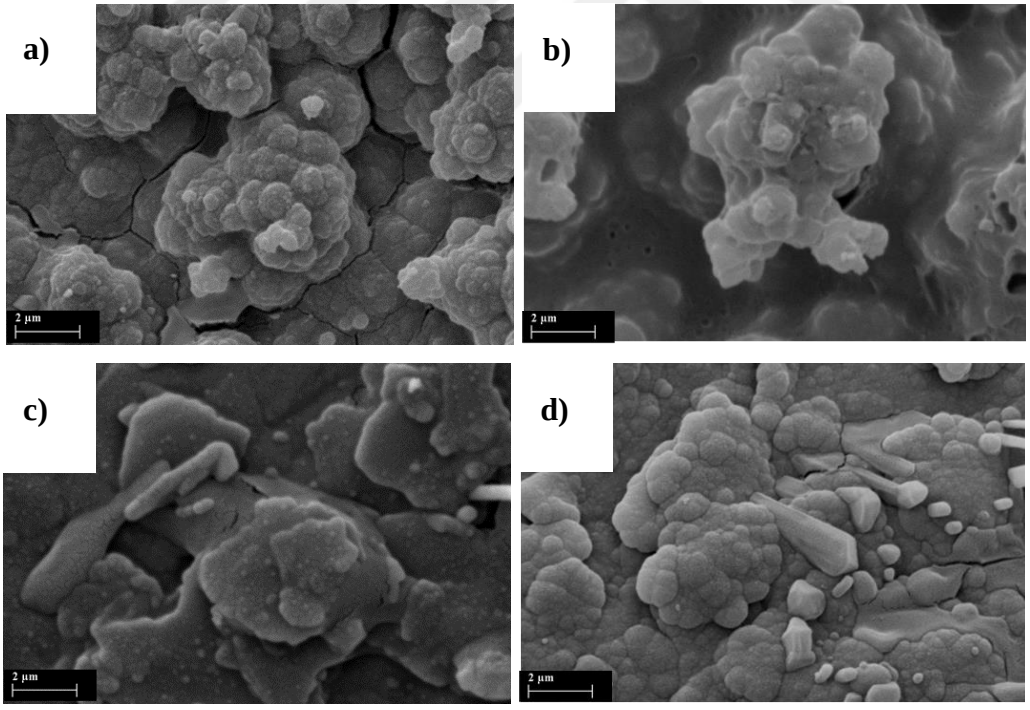


Figure 3.22. The SEM image of M2@PPY/PGEs consisting of **a)**3 mg **, b)**5 mg , **c)**10 mg and **d)** 20 mg M2

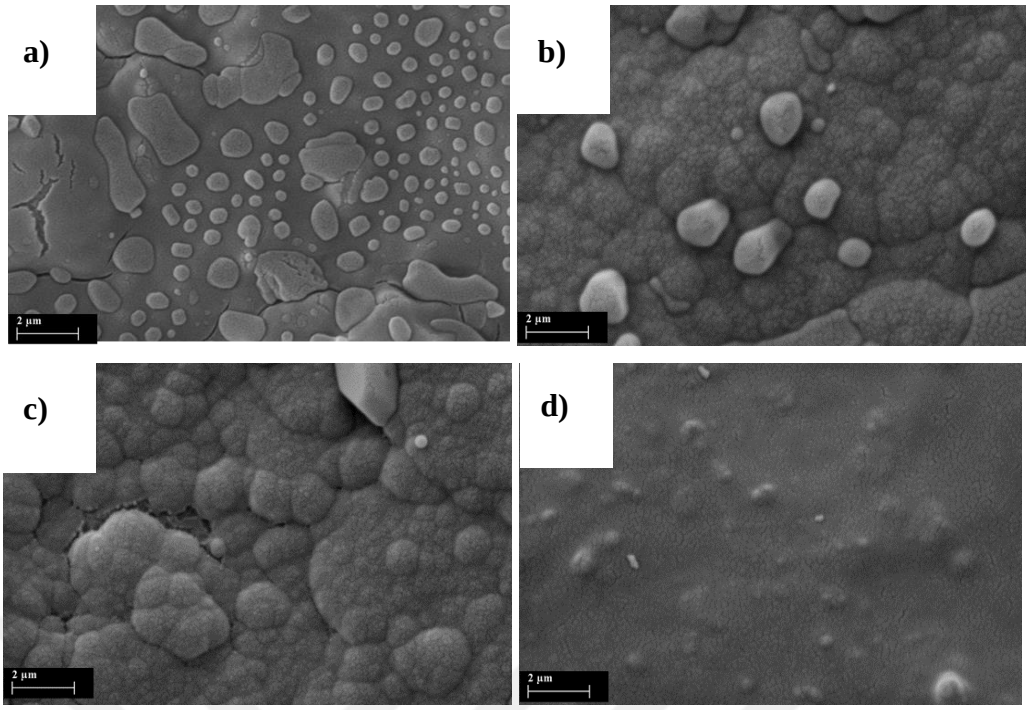


Figure 3.23. The SEM image of M3@PPY/PGEs consisting of **a)**3 mg **, b)**5 mg , **c)**10 mg and **d)**20 mg M3

- **Morphological Analysis of the ED modified EM1@PPY/PGE, EM2@PPY/PGE, EM3@PPY/PGE Group**

SEM analysis of PPy/PGE electrodes offers crucial insights into the structural characteristics influenced by the number of polymerization cycles [110]. The optimal morphology suggests a balance between polymer growth and surface area, essential for achieving superior electrochemical performance. SEM images of EM1@PPy/PGE electrodes at varying mass loadings (3 mg, 5 mg, 10 mg, 20 mg) at **Fig.3.24** shows changes in morphology influenced by ethylenediamine (ED) contribution and mass loading [164].

At 5 mg mass loading at **Fig.3.24.a**, SEM images reveal a uniform distribution of EM1@PPy particles on PGE electrodes. The morphology exhibits increased stability attributed to ethylenediamine and maintains smaller particle sizes, contributing to improved surface area compared to standard MOF5. For 10 mg EM1@PPy/PGE, SEM images display a denser coverage of EM1@PPy particles on PGE electrodes at at **Fig.3.24.b**. The morphology indicates enhanced stability in acidic conditions, facilitated by ethylenediamine modification [68]. Smaller particle

sizes contribute to a larger surface area, enhancing electrochemical performance. SEM analysis at at **Fig.3.24.d** shows a significant accumulation of EM1@PPy particles on PGE electrodes at higher mass loading with 20 mg EM1@PPy/PGE. The morphology exhibits stability under acidic conditions, attributed to ethylenediamine, with particles maintaining smaller sizes for increased surface area compared to standard MOF5 [108].

The SEM images for EM2@PPy/PGE show as at **Fig.3.25** a well-defined structure where the EM2 MOF particles are evenly distributed within the polypyrrole matrix. The uniform dispersion and smooth surface suggest good incorporation and interaction, contributing to a stable and effective electrode. EM2@PPy/PGE has a BET surface area of 26.188 m^2/g, which is relatively low compared to other composites but still indicative of a decent surface area for electrochemical activity.

The SEM images highlight a porous structure similar to MOF5, with EM3 particles well-dispersed within the polypyrrole matrix **(Fig.3.25)**. The polypyrrole appears to provide a stable and continuous coating around the MOF particles. This combination of high surface area and thermal stability suggests a potentially high-performing electrode with good electrochemical properties. EM3@PPy/PGE shows a BET surface area of 74.7351 m^2/g, which is moderate and supports a reasonable amount of surface for electrochemical reactions This indicates a potentially high performance for the electrode due to the good incorporation of the MOFs into the conducting polymer.

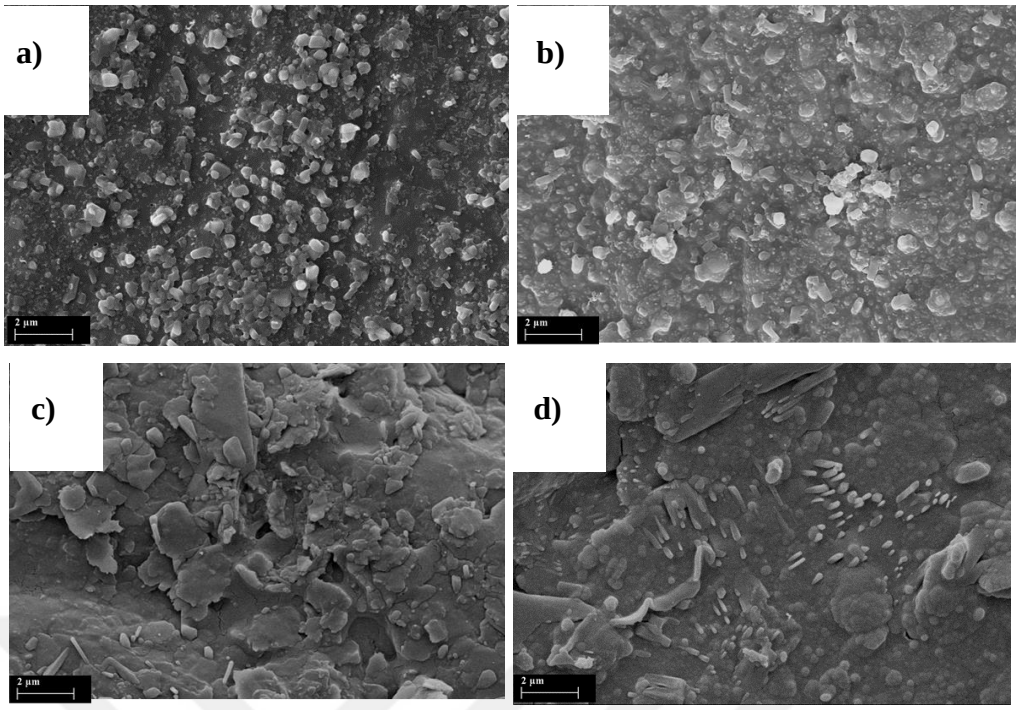


Figure 3.24. The SEM image of EM1@PPY/PGEs consisting of **a)**3 mg **, b)**5 mg, **c)**10 mg and **d)**20 mg EM1

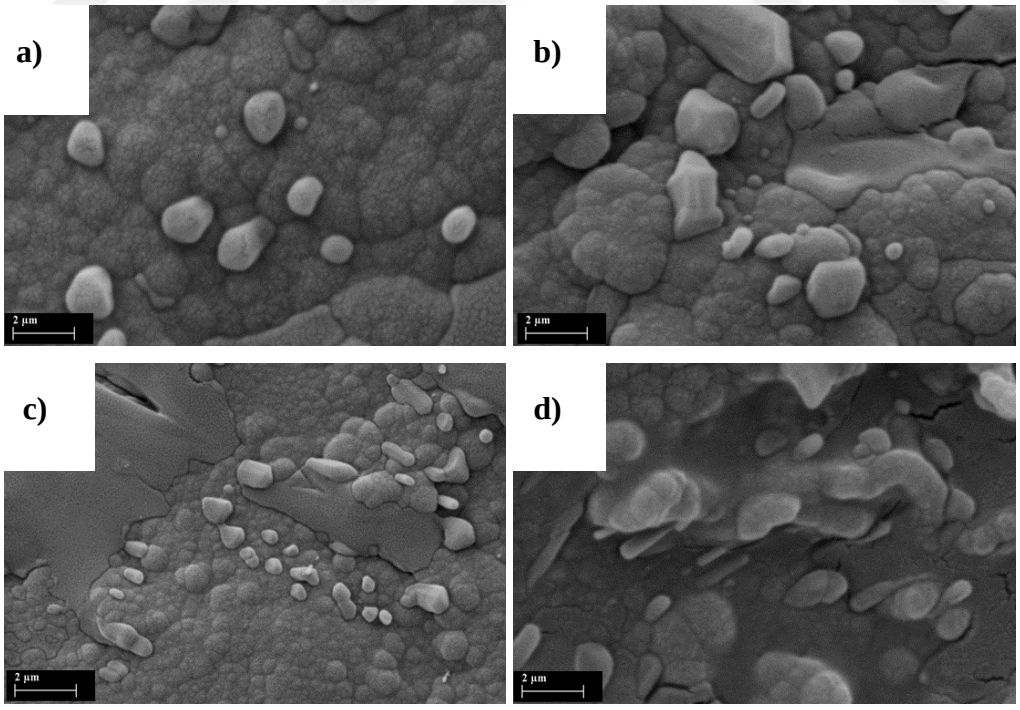


Figure 3.25. The SEM image of EM2@PPY/PGEs consisting of **a)**3 mg **, b)**5 mg , **c)**10 mg and **d)**20 mg EM2

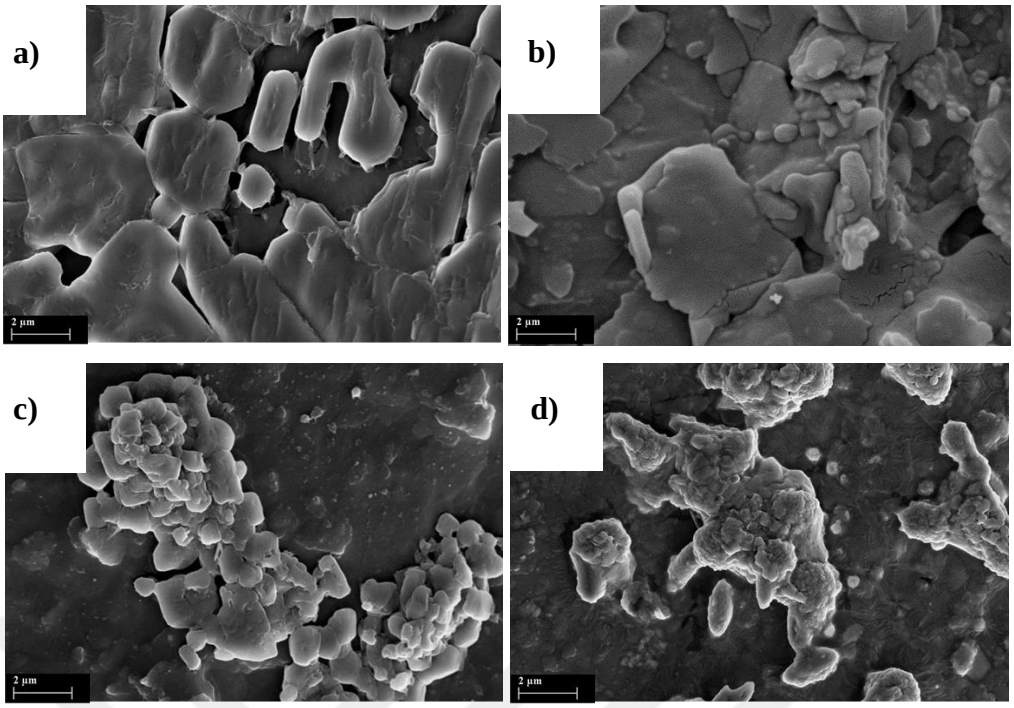


Figure 3.26. The SEM image of EM3@PPY/PGEs consisting of **a)**3 mg **, b)**5 mg , **c)**10 mg and **d)**20 mg EM3

Analyzing the structure of ED modification electrodes using SEM offers important information about the impact of ethylenediamine modification and mass loading on their composition. Enhanced stability in acidic conditions and smaller particle sizes contribute to increased surface area, which is important for improving electrochemical performance in different applications [168]. Comprehension of these morphological characteristics helps customize electrode properties for improved performance in sensors, energy storage devices, and other electrochemical uses

- **Morphological Analysis of the M4@PPY/PGE, M5@PPY/PGE, M6@PPY/PGE Group**

Ethylenediamine (ED) modification of MOFs can potentially enhance their stability in acid medium, which is beneficial for galvanostatic charge-discharge tests in acidic environments. ED modification introduces amine functional groups to the MOF's surface. These functional groups can interact with the framework, potentially enhancing its stability by forming stronger chemical bonds or protecting the MOF from acid-induced degradation [120]. Amines introduced by ED

modification can act as pH buffers, mitigating the impact of acidic conditions. They may help maintain a more neutral local environment around the MOF, reducing acid-induced degradation [116].

SEM images of M4@PPy/PGE electrodes at varying mass loadings (3 mg, 5 mg, 10 mg, 20 mg) reveal morphological characteristics influenced by the composite nature of polypyrrole (PPy) with HKUST1 shown at **Fig.3.27**.

SEM analysis shows a morphology resembling tetrahedral structures typical of HKUST1 embedded within the PPy matrix on PGE electrodes. The composite structure exhibits stable morphology with even distribution at lower mass loading. At 5 mg mass loading at **Fig.3.27.a**, SEM images reveal a well-balanced composite structure of M4@PPy on PGE electrodes [169]. The morphology demonstrates optimal properties derived from both the conducting polymer and metal organic framework, enhancing overall stability and surface area. SEM images display an increased coverage of M4@PPy particles on PGE electrodes at higher mass loading 10 mg M4@PPy/PGE at **Fig.3.27.b.** The morphology maintains the tetrahedral structure of HKUST1 with a dense distribution within the PPY matrix, indicating robust stability and potential for enhanced electrochemical performance. 20 mg M4@PPy/PGE SEM analysis shows a significant accumulation of M4@PPy particles on PGE electrodes at the highest mass loading. The morphology highlights a dense composite structure with well-defined tetrahedral HKUST1 shapes embedded in the PPy matrix, emphasizing stability and surface area advantages for electrochemical applications [110].

The SEM images show that M5 particles are somewhat bulky but still exhibit a discernible hexagonal structure. **Fig.3.28** shows the SEM images for M5@PPy/PGE show a composite structure where the MOF particles appear to be more dispersed and less aggregated compared to M3@PPY/PGE. The interaction between M5 and the polypyrrole matrix is visible, with some degree of surface roughness observed .The polypyrrole matrix appears to incorporate these particles effectively, although the surface roughness and bulkiness may impact the overall electrochemical performance by potentially limiting the accessible surface area. M5@PPy/PGE has a relatively low BET surface area (2.2403 m^2/g), which suggests that while the MOF particles are present, their contribution to the surface area is limited compared to other composites. This clustering may influence the overall

electrochemical performance by affecting the contact points between the MOF particles and the conducting polymer.

The SEM images at **Fig.3.29** of M6@PPy/PGE reveal a similar trend to M5, with a relatively more bulky appearance of the MOF particles embedded within the polypyrrole matrix. The hexagonal structures of M6 are still visible but appear more diffuse due to the polymer matrix. The low surface area and bulkier nature of the MOF particles suggest that while the composite is stable, the performance might be constrained by the limited surface area available for electrochemical reactions. M6@PPy/PGE exhibits an extremely low BET surface area (0.0165 m^2/g), which is significantly lower than other composites. This suggests that the surface area available for electrochemical activity is minimal, potentially affecting the electrode's performance. The diffusion of M6 particles within the polymer matrix suggests a balanced incorporation but may also imply some degree of particle aggregation.

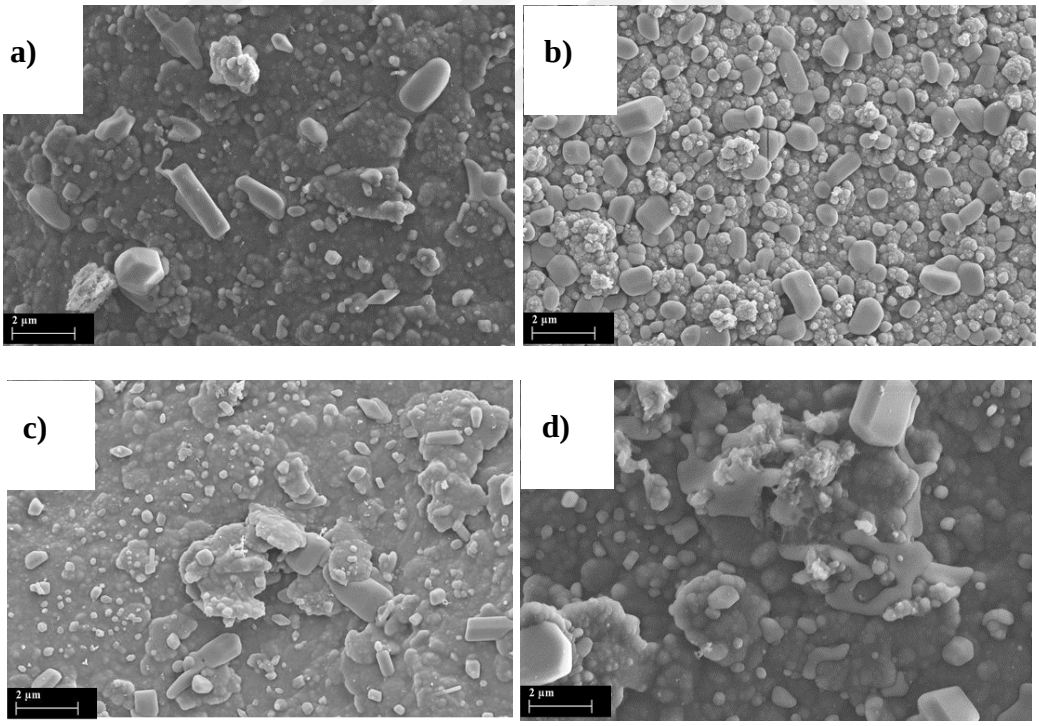


Figure 3.27. The SEM image of M4@PPY/PGEs consisting of **a)**3 mg **, b)**5 mg , **c)**10 mg and **d)**20 mg M4

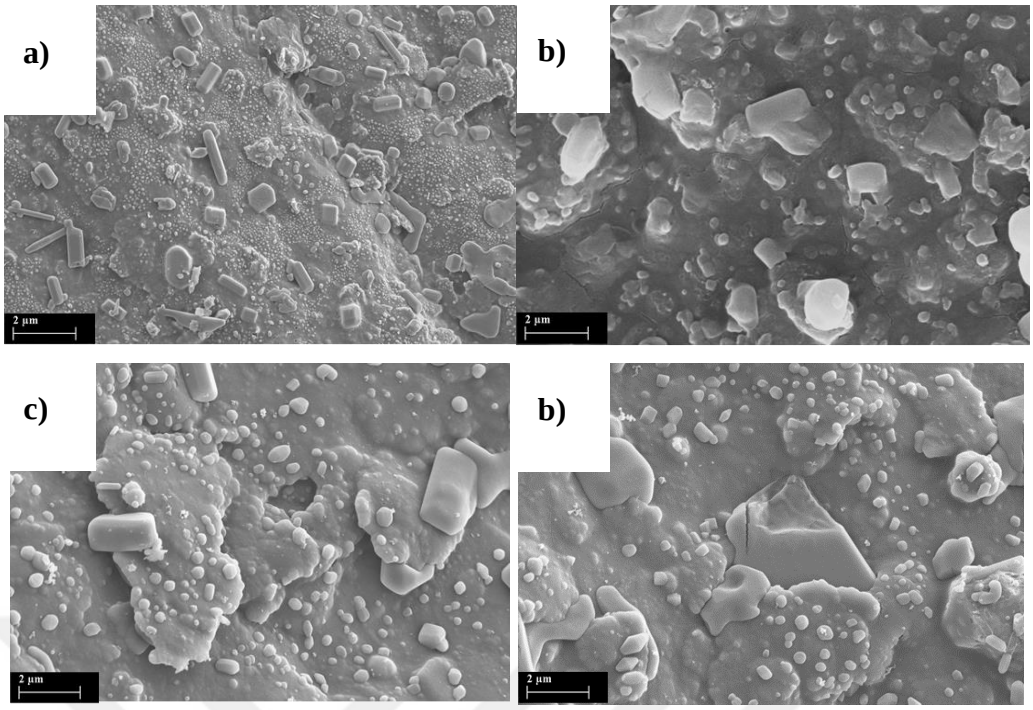


Figure 3.28. The SEM image of M5@PPY/PGEs consisting of **a)**3 mg **, b)**5 mg , **c)**10 mg and **d)**20 mg M5

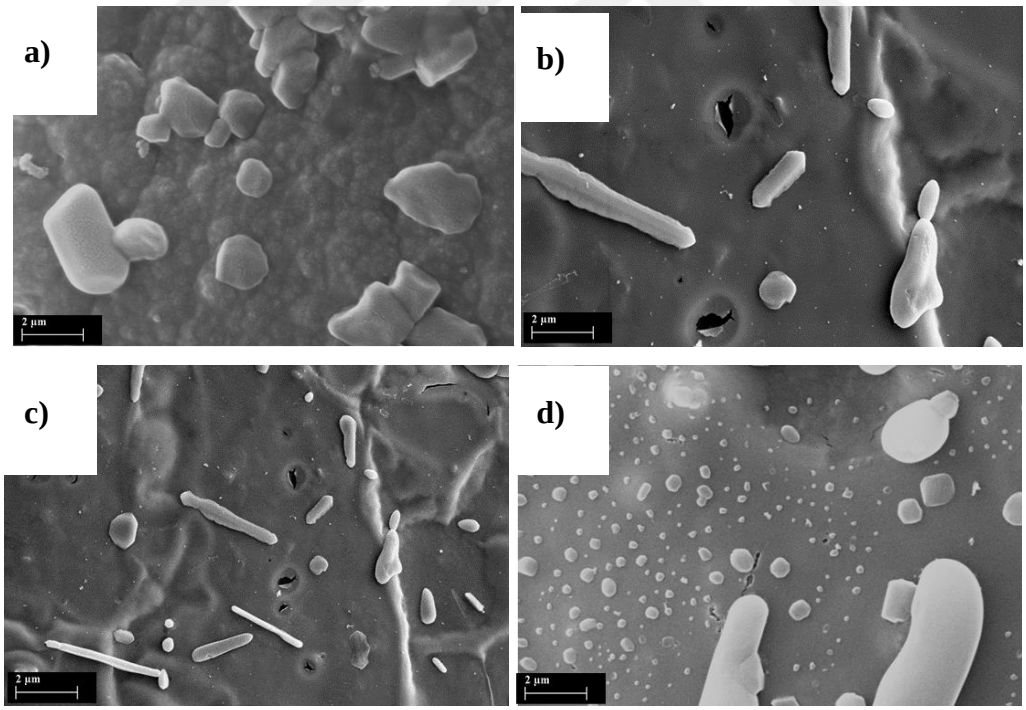


Figure 3.29. The SEM image of M5@PPY/PGEs consisting of **a)**3 mg **, b)**5 mg , **c)**10 mg and **d)**20 mg M5

ED modification might passivate certain reactive sites within the MOF structure, making them less susceptible to acid attack. This passivation can improve the

MOF's resistance to degradation in acidic media [155]. The modification could alter the chemical environment around metal sites within the MOF, potentially making them less prone to dissolution or leaching in acidic conditions.

- **Morphological Analysis of the ED modified EM4@PPY/PGE, EM5@PPY/PGE, EM6@PPY/PGE Group**

ED modification can be part of a strategy to tailor HKUST-1 for targeted applications where surface chemistry and charge transfer kinetics play crucial roles, outweighing the significance of pore size. While ED modification may contribute to enhancing MOF stability in acid medium, it's essential to conduct thorough testing and evaluation under relevant conditions to validate the improved stability. Galvanostatic charge-discharge tests can be performed to assess the stability and electrochemical performance of ED-modified MOFs in acidic environments, providing insights into their suitability for practical applications in acidic electrochemical systems like supercapacitors or batteries [118].

Fig.3.30 shows the SEM characterization of EM4@PPy/PGE electrodes a composite morphology integrating tetrahedral HKUST1 structures with the conducting polymer PPy. Optimal properties, including stability and surface area, are observed at 5 mg mass loading, where the composite benefits from synergistic effects between PPy and HKUST1 [168]. Understanding these morphological features facilitates the optimization of electrode properties for improved performance in sensors, energy storage devices, and other electrochemical applications.

The SEM images for EM5@PPy/PGE show a surface where EM5 MOF particles are distributed throughout the polypyrrole matrix. The SEM images reveal that EM5 particles are somewhat bulkier, but the hexagonal structures are still discernible. The particles appear to be well-integrated but with a slightly more pronounced roughness compared to other composites. EM5@PPy/PGE has a BET surface area of 2.8737 m^2/g, which is quite low compared to other composites, indicating limited surface area for electrochemical activity. The rougher surface may be attributed to the nature of the EM5 particles and their interaction with the polypyrrole matrix **(Fig.3.31)**.

The SEM images for EM6@PPy/PGE reveal a composite with visible EM6 MOF particles embedded within the polypyrrole matrix can be seen at **Fig.3.32**. The particles appear to be more dispersed and less agglomerated compared to other composites. The low surface area and bulky nature suggest that while the composite is stable, the limited surfac area might constrain its electrochemical performance. EM6@PPy/PGE exhibits an extremely low BET surface area (0.0165 m^2/g), suggesting a very limited surface area available for electrochemical activity. The dispersion of EM6 MOF particles in the polypyrrole matrix shows effective incorporation, but the bulkier nature of the particles may lead to a less uniform surface compared to other composites.

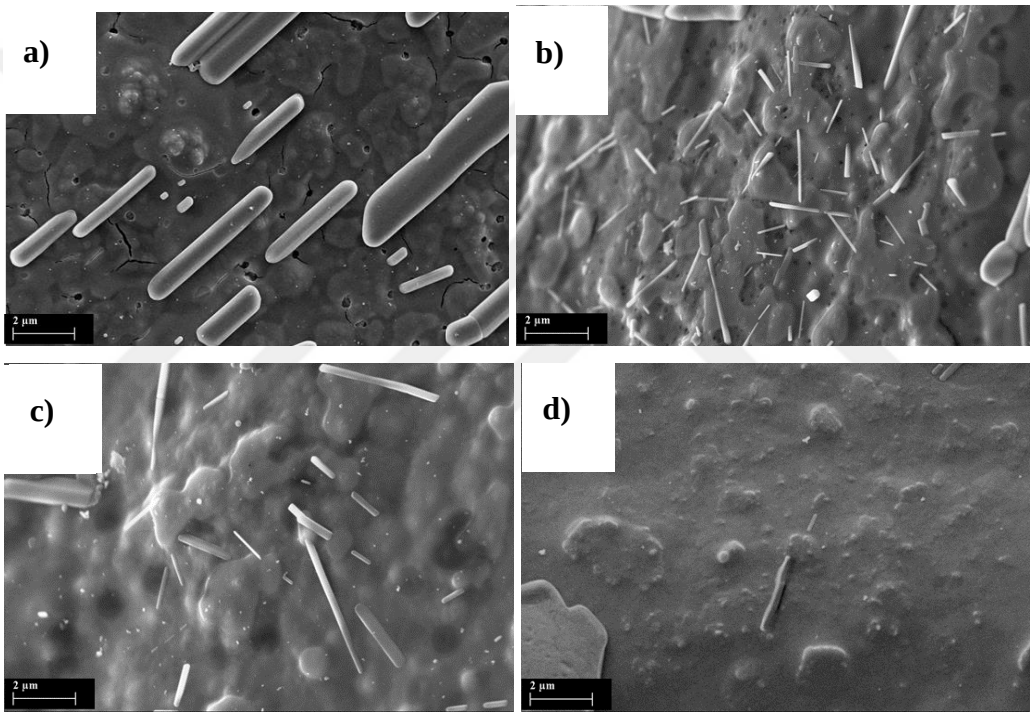


Figure 3.30. The SEM image of EM4@PPY/PGEs consisting of **a)**3 mg **, b)**5 mg, **c)**10 mg and **d)**20 mg EM4

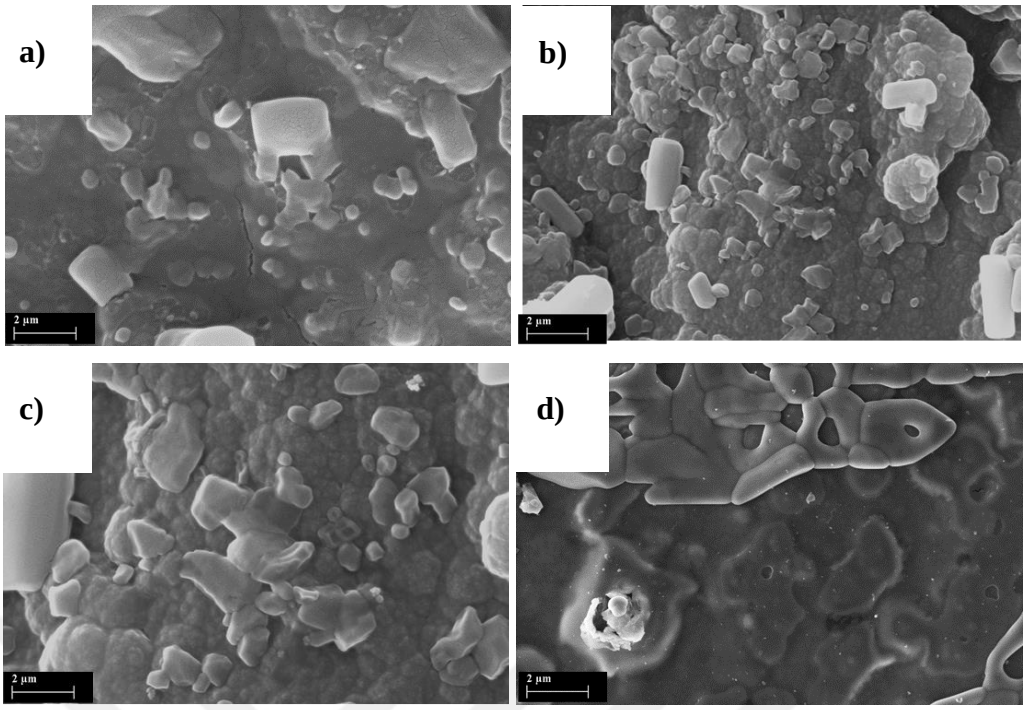


Figure 3.31. The SEM image of EM5@PPY/PGEs consisting of **a)**3 mg **, b)**5 mg, **c)**10 mg and **d)**20 mg EM5

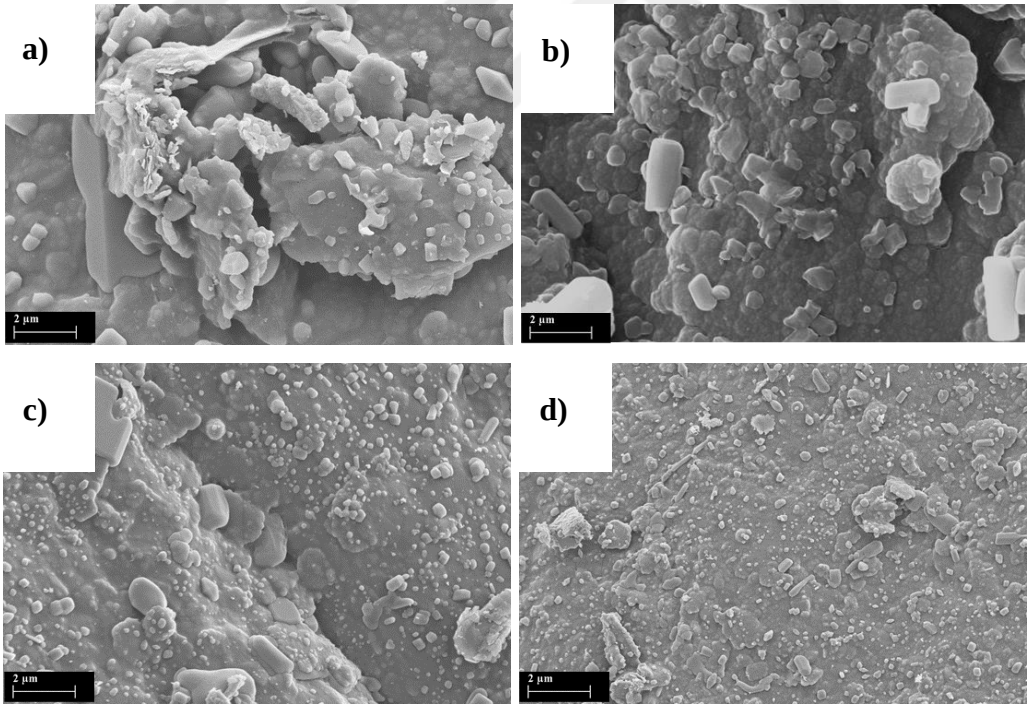


Figure 3.32. The SEM image of EM6@PPY/PGEs consisting of **a)**3 mg **, b)**5 mg, **c)**10 mg and **d)**20 mg EM6

3.2.2 Electrochemical Characterization of the Electrodes

This thesis utilized the CV method to perform pre-optimizations on various parameters involved in the production of composite electrodes. In this scenario, the electrodes were created to act as working electrodes and their capacitive behavior was assessed in a 1.0 M sulfuric acid solution. In this research, Pt will serve as the counter electrode and Ag/AgCl (in 3 M KCl) will be utilized as the reference electrode [133]. Capacitive characteristics were analyzed within the potential range that needed to be maximized. Optimizations were made for both the number of cycles and the quantity of MOF in this scenario.

In the process of electropolymerization, pyrrole monomers undergo oxidation at the surface of the electrode, leading to the creation of cations and the formation of a polymer chain known as polypyrrole or PPy on the electrode. The process persists while the potential is cyclically varied between -0.3 V and 1 V, causing the gradual accumulation of the conducting polymer PPy onto the electrode. Pyrrole oxidation commences polymerization at approximately 0.8-1.0 V. The continuous rise in current with each scan shows that the conductive polymer (PPy) is being deposited on the electrode. As the cycle repeats, the polymer's surface area and conductivity grow, resulting in increased current reactions.

Fig. 3.33. shows the production voltammogram of PPy/PGE. The oxidation stage of the forward scan, an anodic peak is observed, indicating the oxidation of pyrrole monomers. As more cycles are completed, the peaks, particularly the anodic peaks, shift and widen, showing ongoing polymer growth and alterations in the electrode's surface characteristics[68]. The peak on the red curve (corresponding to the 10th cycle) is more noticeable at **Fig. 3.33.**, suggesting an increase in conductivity or thickness of the polymer layer.

The steady rise in the current during each scan suggests that polymer is being deposited onto the electrode surface. Greater amounts of PPy are accumulated as the current increases, leading to higher conductivity levels. The graph **Fig. 3.33.** shows that a clearly identifiable conducting polymer has developed on the pencil graphite electrode following 10 cycles. To conclude, this cyclic voltammogram verifies the effective electropolymerization of pyrrole, resulting in the formation of

a conductive PPy coating on the pencil graphite electrode. The rising current in each cycle indicates that the polymerization process is effective, leading to a conductive polymer film.

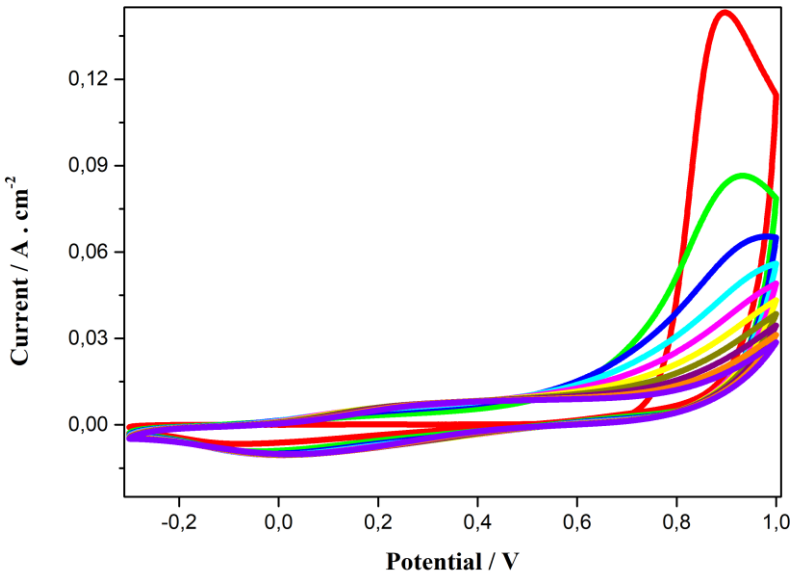


Figure 3.33. Production voltammogram of PPy/PGE

The initial phase of the research involved studying parameters like acid concentration, monomer concentration, and cyclic number that impact the capacitive behaviors of electrodes through CV and EIS analysis. The diagrams display the cyclic voltammograms of the electrodes that were prepared using varying concentrations of pyrrole. In the **Figure 3.34**, it is evident that the solution containing 0.5 M pyrrole and 0.1 M sulfuric acid exhibited the highest peak current and capacity. As the concentration of monomer increased, the degree of polymerization also increased, resulting in a consistent improvement in the capacitive properties of the electrodes from 0.05 M pyrrole to 0.5 M pyrrole electrodes **(Fig.3.34.a).** Nevertheless, if the monomer concentration exceeded 0.5 M, the exfoliation of polypyrrole initiated at the electrode interface. Truly, the mesoporous formation reduced because of the high level of polymerization on the electrode surface created with 1.0 M and 2.0 M pyrrole [69]. In **Fig.3.34.b** and **Table 3.12.,** EIS analysis further confirmed the results from cyclic voltammetric characterization. When the electrodes were made using 0.5 M pyrrole, the Rs and Rct values showed a decrease, suggesting a higher electrical conductivity in this

electrode mixture. Certainly, the electrode exhibited the highest value of double layer capacitance. Therefore, the ideal amount of pyrrole in the electrochemical synthesis of PPy/PGE was determined to be 0.5 M for future investigations [170].

The capacitive behaviors of the electrodes were examined by analyzing the impact of sulfuric acid concentration through cyclic voltammetry and electrochemical impedance spectroscopy. The diagram from **Fig.3.34.c** displays the cyclic voltammograms of PPy/PGEs created using varying levels of sulfuric acid and 0.5 M pyrrole across 10 voltammetric cycles. As shown in the **Figure 3.34.c.** the highest current and peak redox capacity were found in the solution containing 1.0 M sulfuric acid. If the sulfuric acid concentration deviates from 1.0 M, the capacitive properties of the electrodes decrease. The best level of conductivity was achieved when the conducting polymer was in the optimal pronation in a 1.0 M sulfuric acid solution, leading to the highest capacitive behavior observed in this concentration [133]. Based on the **Fig.3.34.d** EIS spectra of the electrodes, it was found that the electrode made in 1.0 M sulfuric acid had the lowest charge transfer resistance **(Table 3.13)**. This also indicated that the redox reactions of pseudocapacitors happened more readily in this electrode compared to others. The electrode prepared in 1.0 M sulfuric acid exhibited the highest diffusion rate, as indicated by the highest Warburg impedance value. During the final phase of producing the conducting polymer, the number of cycles was adjusted for optimal results [133].

Figure 3.34.e displays the cyclic voltammograms of electrodes created through varying voltammetric cycles. As the voltammetric cycles increased from 10 to 50, reductions were seen in the peak current and capacities of the electrodes. This was primarily associated with the exfoliation of the conducting polymers that were prepared on the surface of the electrode. The exfoliation of the electrodes increased with each cycle as the optimal pyrrole concentration was 0.5 M. Furthermore, electrodes with closed mesoporous sides were prepared over more than 10 cycles. EIS analysis provided evidence in support of this outcome as seen in **Table 3.14.** The electrode created through 10 cycles had the lowest solution resistance and charge transfer resistance, while exhibiting the highest Warburg impedance and double layer capacitance value. This also shows improved capacitive behaviors in this electrode **(Fig.3.34.f).** Therefore, the ideal number of cycles for preparing the

electrode using cyclic voltammetry was determined to be 10 for creating metal organic frameworks with conducting polymers for supercapacitor use [69].

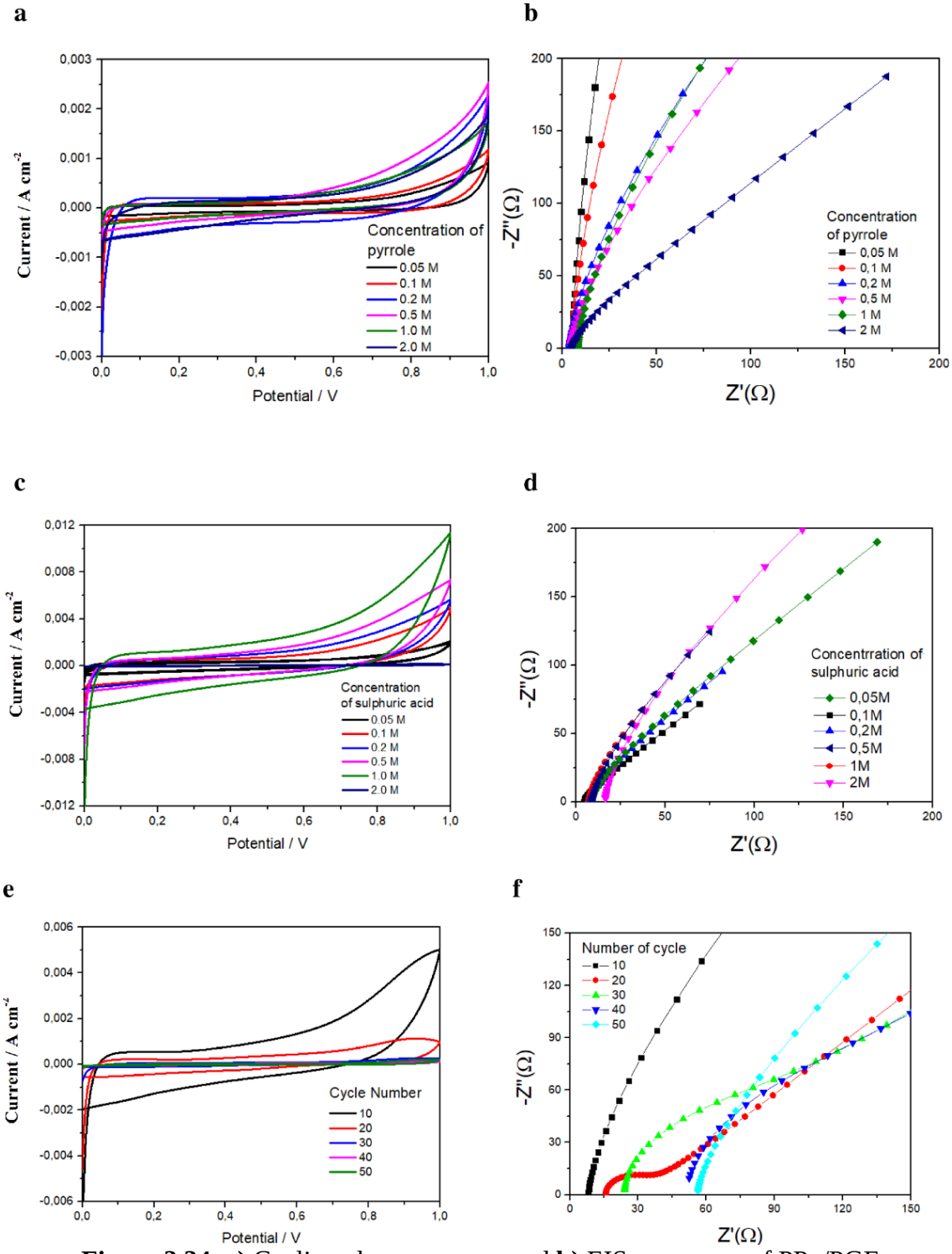


Figure 3.34. a) Cyclic voltammograms and **b)** EIS spectrums of PPy/PGEs prepared in different concentration of pyrrole, **c)** cyclic voltammograms and **d)** EIS spectrums of PPy/PGEs prepared in different concentration of sulfuric acid, **e)** cyclic voltammograms and **f)** EIS spectrums of PPy/PGEs prepared over different cycles, and of PPy/PGEs prepared over different cycles

Table 3.12. Rs, Rct, Cdl and Warburg impedance values of the electrodes prepared in the solution consisting different concentration of pyrrole

Concentration of pyrrole	***Rs / ohm***	***Rct / ohm***	***Cdl / mF***	***W***
0.05 M	5.4	5.9	0.644	0.0001834
0.1 M	5.3	5.4	1.240	0.0004928
0.2 M	3.8	6.7	1.252	0.0019180
0.5 M	4.6	4.7	2.692	0.0021960
1 M	8.1	8.4	0.786	0.0011030
2 M	5.0	5.1	0.797	0.0052900

Table 3.13. Rs, Rct, Cdl and Warburg impedance values of the electrodes prepared in the solution consisting different concentration of sulfuric acid

Concentration of sulphuric acid	***Rs / ohm***	***Rct / ohm***	***Cdl / mF***	***W***
0.05 M	8.3	10.0	1.222	0.005193
0.1 M	4.6	4.9	2.426	0.013890
0.2 M	7.9	8.4	3.687	0.010210
0.5 M	9.2	9.7	6.315	0.006665
1 M	7.1	7.2	14.28	0.011140
2 M	16.5	43.3	0.003	0.000122

Table 3.14. Rs, Rct, Cdl and Warburg impedance values of the electrodes prepared in the solution consisting of 0.5 M pyrrole and 1.0 M sulfuric acid over different voltammetric cycles

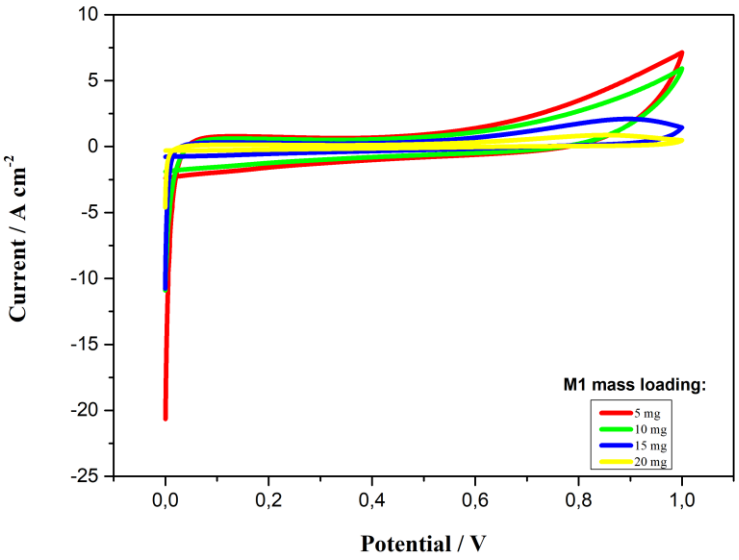
Cycle number	*Rs / ohm*	*Rct / ohm*	*Cdl / mF*	*W*
10	8.1	9.7	6.7200	0.0043660
20	15.7	18.1	0.0097	0.0031590
30	23.9	64.3	0.0028	0.0003732
40	51.5	77.9	0.8210	0.0001477
50	45.7	78.7	0.0030	0.0001469

- **Electrochemical Analysis of the M1, M2 and M3 Group**

The cyclic voltammograms of PGE electrodes with MOF@PPy show distinct redox peaks that indicate interactions between MOF5 and polypyrrole on the electrodes. The peaks represent the electrochemical processes that occur due to M1's porous structure and PPy's conductive matrix, seen in SEM analyses revealing clear shapes with tetrahedral M1 crystals integrated in the PPy network [171].

With a mass loading of 5 mg, the cyclic voltammograms show distinct oxidation-reduction peaks, indicating fast charge transfer and improved electrochemical stability. This aligns with SEM results showing improved electrode shape, increasing surface area and ion exchange capabilities for better electrochemical performance. **Fig 3.35.a** shos that the differences in mass loading impact the strengths and locations of these redox peaks, highlighting how M1 boosts the electrode's electrochemical performance by maintaining its structure and storing ions effectively [147]. Therefore, the best condition for M1@PPy/PGE electrodes is determined to be a mass loading of 5 mg.

a)



b)

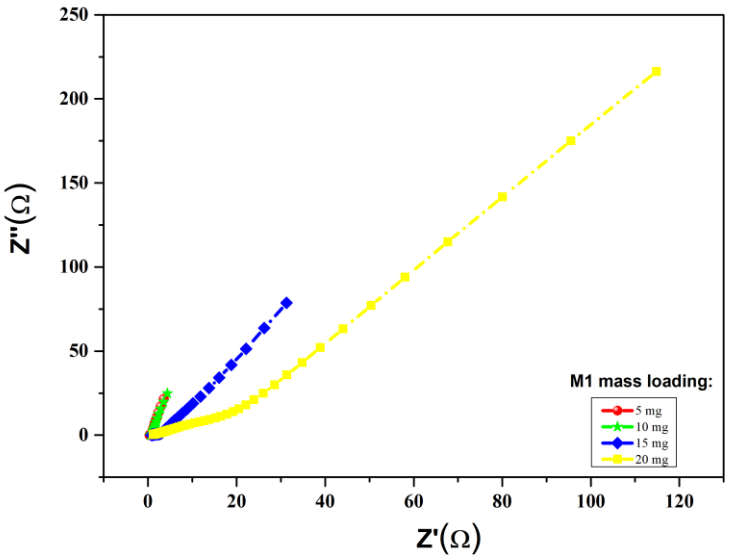


Figure 3.35. Cyclic voltammograms and EIS spectrums of M1@PPy/PGEs consisting different amounts of MOF compounds

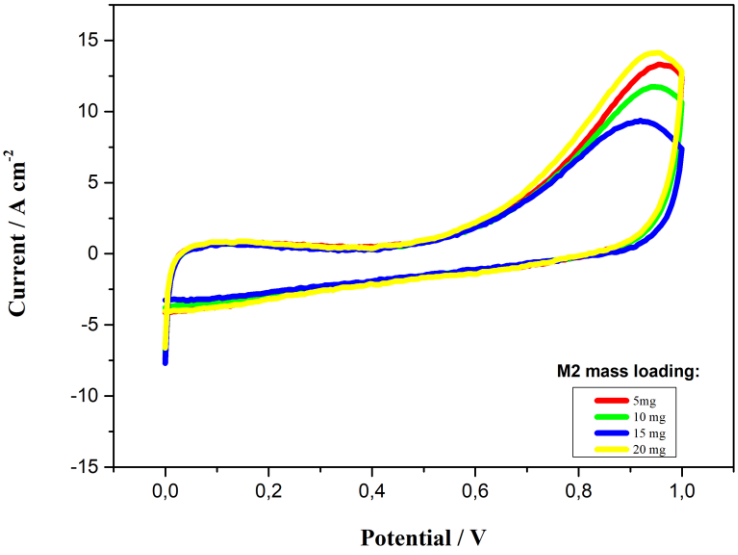
M2@PPy/PGE shows a high specific capacitance with well-defined and symmetric redox peaks, it indicates excellent electrochemical performance. The presence of redox peaks suggests that the MOF is contributing to the overall charge storage mechanism, enhancing the capacitance of the composite (**Fig 3.36.a)**.

For M3@PPy/PGE, if the CV shows a significant increase in specific capacitance compared to pure PPy, this indicates that the incorporation of MOF M3 enhances the electrochemical properties. M3@PPy/PGE displays well-defined peaks as seen

in **Fig 3.37.a**, it suggests good charge storage and transport properties. M3 shows high capacitance and stability, it may be attributed to the MOF's ability to enhance the surface area or improve the charge distribution within the composite.

M1@PPy/PGE performs better than other composites in this group, it could be due to the optimal interaction between M1 and the polypyrrole matrix, maximizing the charge storage capability.

a)



b)

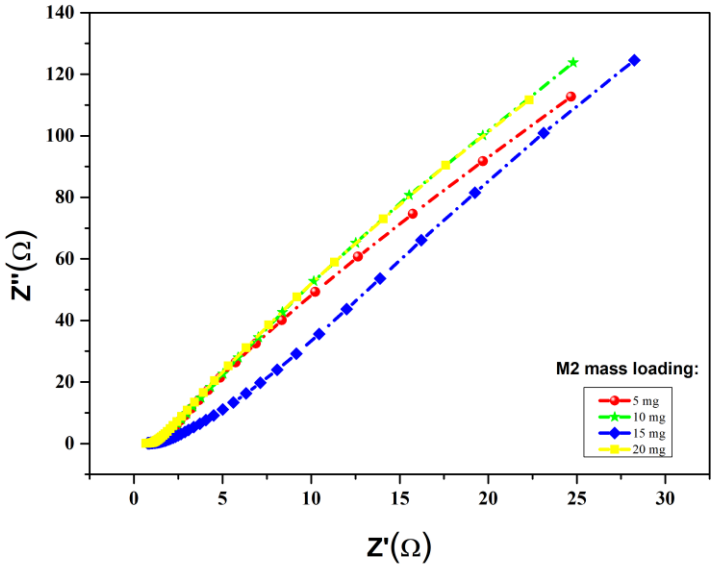
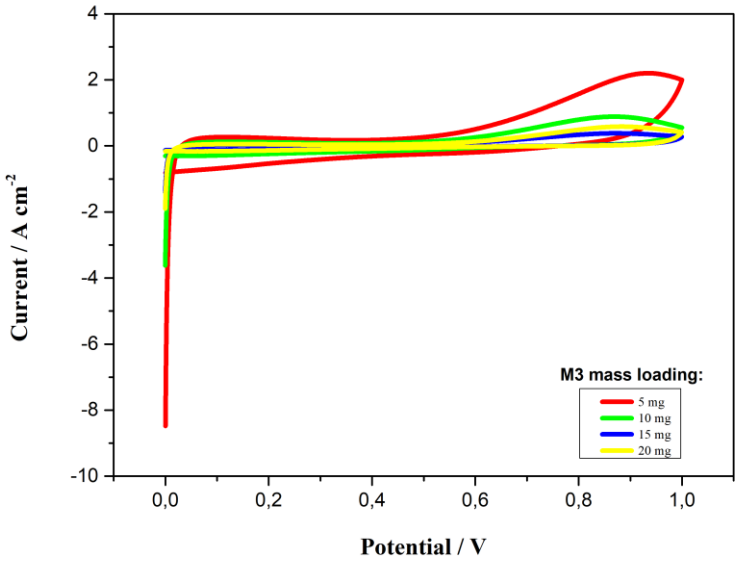


Figure 3.36. Cyclic voltammograms and EIS spectrums of M2@PPy/PGE different amounts of MOF compounds

In the Nyquist plot at **Fig 3.35.b**, M2@PPy/PGE a steep slope in the low-frequency region suggests a high capacitance behavior. M2 exhibits a vertical line at low frequencies, it implies excellent capacitive behavior with minimal diffusion impedance. For M3@PPy/PGE, the impedance plot shows a relatively low and flat line in the low-frequency region, it suggests high capacitance and minimal resistive losses (**Fig 3.36.b)**. A large capacitive behavior at low frequencies is expected. M3 shows a clear and distinct capacitive response, it reflects effective MOF contribution to the overall performance. M1@PPY/PGE performance in EIS be considered the best in this group as it shows similar or better impedance characteristics compared to M2 and M3, suggesting that the MOF contributes positively to the overall electrochemical performance.

a)



b)

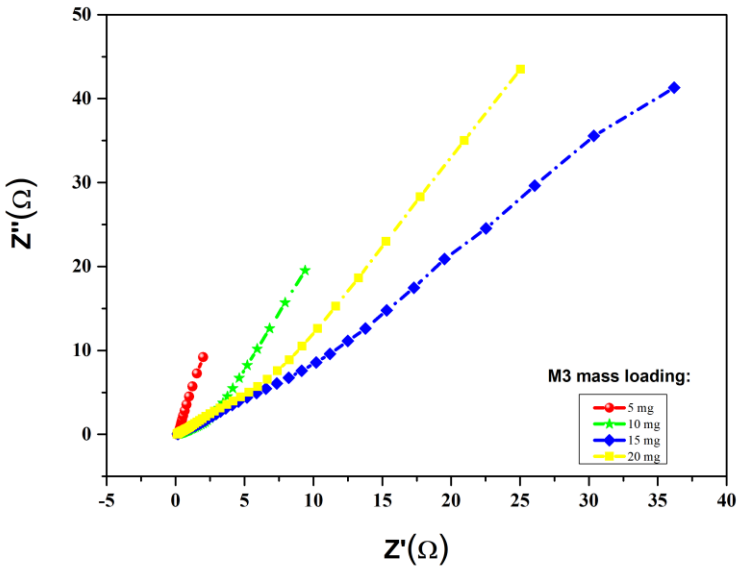
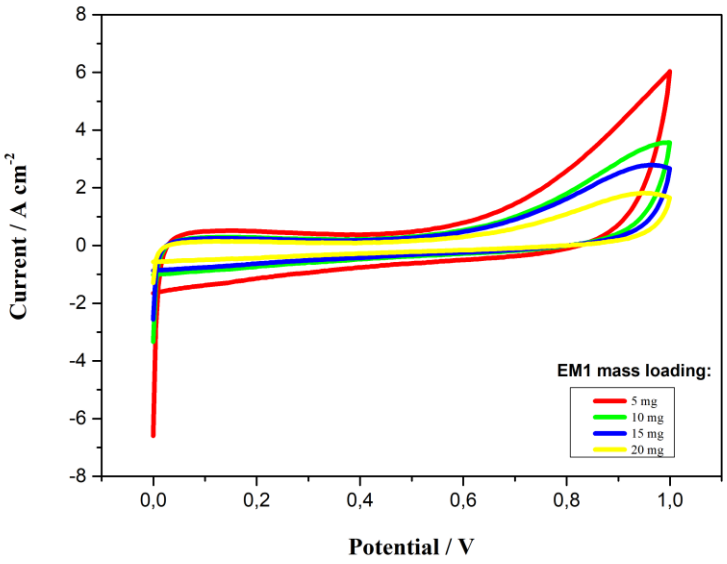


Figure 3.37. Cyclic voltammograms and EIS spectrums of M3@PPy/PGE different amounts of MOF compounds

- **Electrochemical Analysis of the ED modified EM1, EM2 and EM3 Group**

Fig.3.38 the voltammograms show specific redox peaks that are unique to the interactions between MOF5 and polypyrrole (PPY) on pencil graphite electrodes (PGE). The peaks seen in SEM correspond to the electrochemical activity and display distinct morphologies with tetrahedral MOF5 crystals incorporated in the PPY matrix [172]. Ideal mass loading conditions, as determined by analyzing BET surface area and pores, show distinct oxidation-reduction peaks that suggest effective charge transfer kinetics and improved electrochemical stability. The connection between surface area improvement and structural integrity in SEM is crucial for improving electrochemical performance in capacitive uses [133]. The integration of ED further enhances ion accessibility, reinforcing 5 mg as the optimum mass loading for EM1@PPY/PGE electrodes.

a)



b)

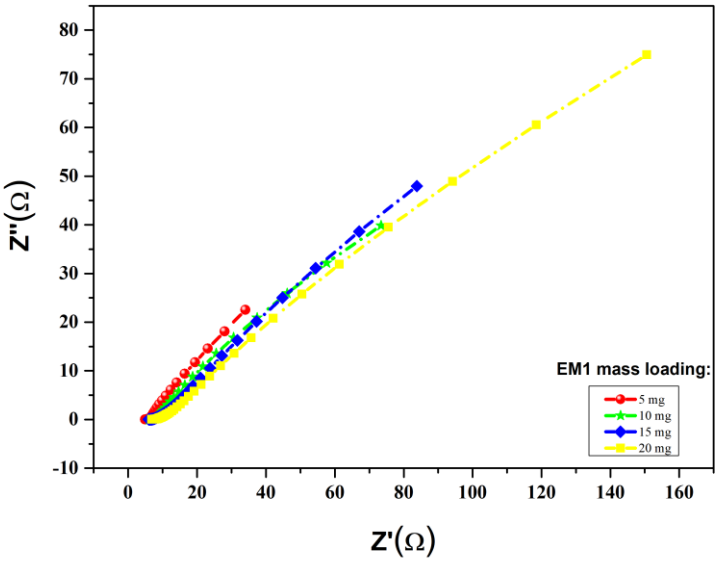


Figure 3.38. Cyclic voltammograms and EIS spectrums of EM1@PPy/PGE different amounts of MOF compounds

Changes in redox behavior of M1@PPy/PGE electrodes compared to original electrodes indicate the effect of ethylenediamine (ED) in improving ion exchange capacity and electrochemical activity(**Fig.3.38.a)**. Measurement of BET surface area indicates ideal surface properties that promote ion adhesion and enhance ability to store charge. SEM images from **Fig.3.39** show smaller particle sizes and distribution, pointing to improved surface interactions that are advantageous for electrochemical processes [173]. Incorporating ED into M2 improves electrode

durability and ion access, leading to better electrochemical efficiency. SEM and BET analyses show that the ideal mass loading for EM2@PPy/PGE electrodes is 5 mg.

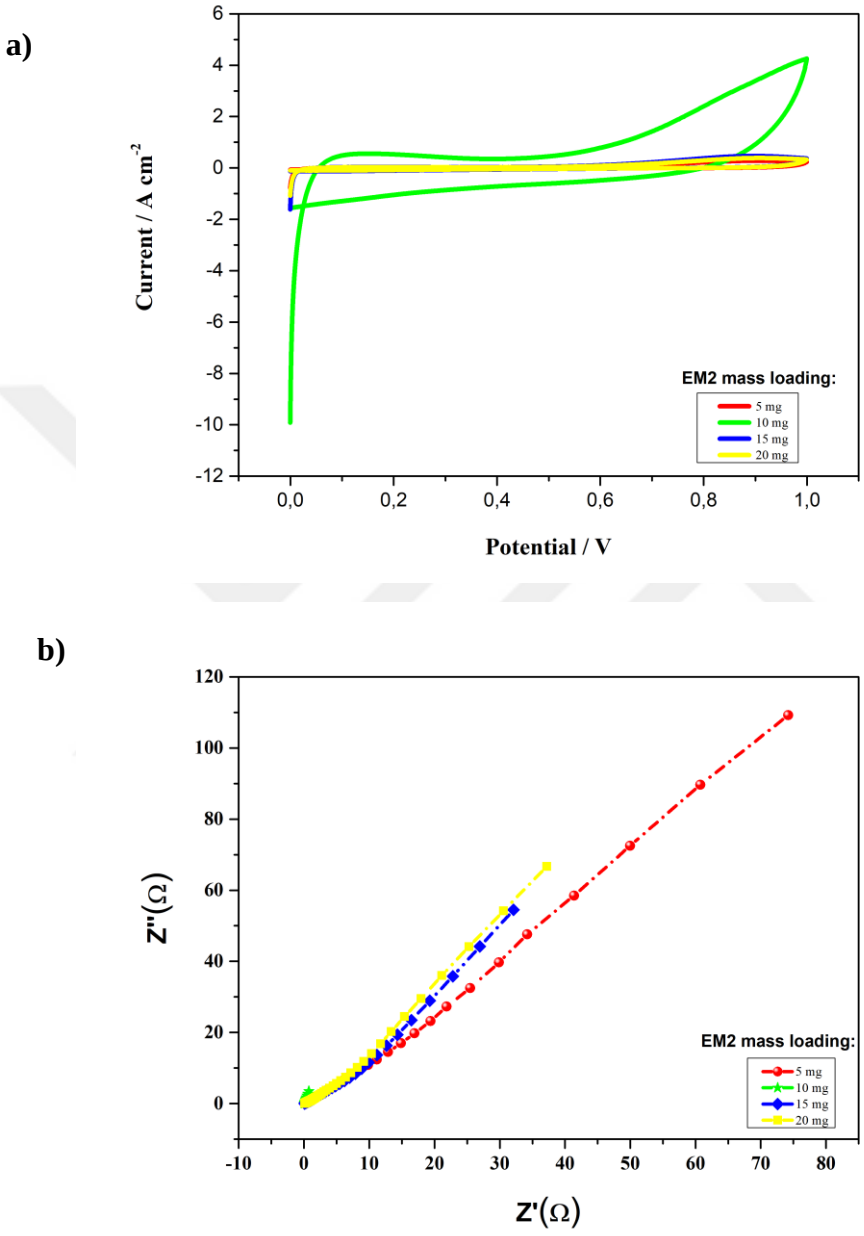


Figure 3.39. Cyclic voltammograms and EIS spectrums of EM2@PPy/PGE different amounts of MOF compounds

Customized oxidation-reduction peaks in cyclic voltammograms demonstrate how cobalt affects the dynamics of charge transfer and the electrochemical stability in EM3@PPy/PGE electrodes. SEM observations show morphological characteristics that promote higher surface area and improved ion diffusion paths **(Fig.3.40).**

Analysis of BET surface area affirms improved pore structure and enhanced ion storage capacity, supporting the electrochemical behavior noted in cyclic voltammograms. The joint alterations of cobalt and ED improve electrode functionality for advanced electrochemical applications [68].

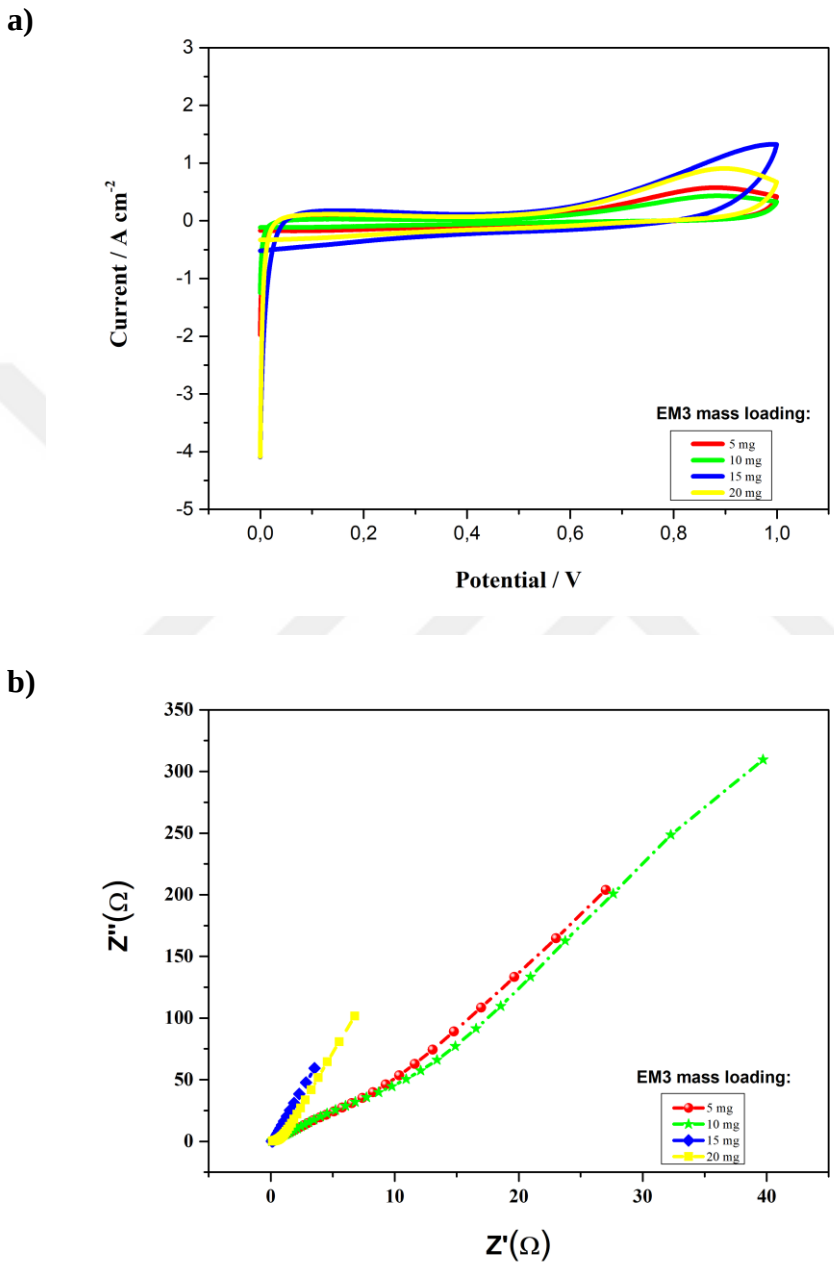


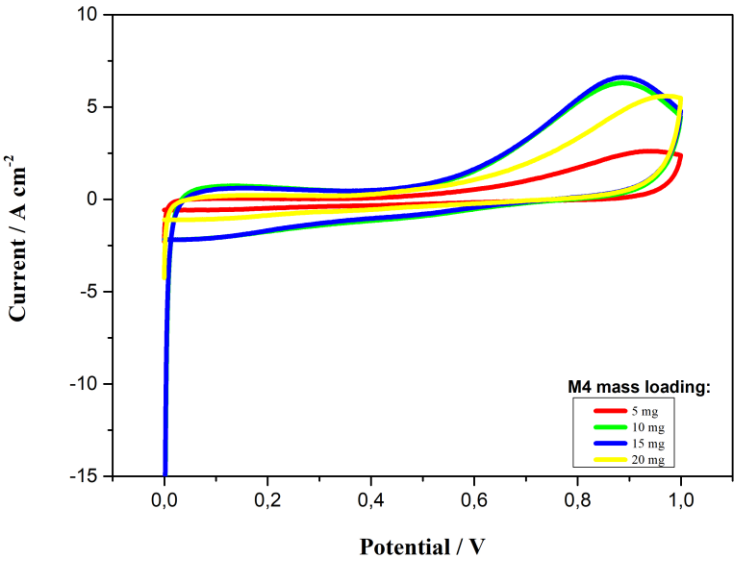
Figure 3.40. Cyclic voltammograms and EIS spectrums of EM3@PPy/PGE different amounts of MOF compounds

- **Electrochemical Analysis of the M4, M5 and M6 Group**

Cyclic voltammograms display distinct redox peaks that show HKUST1 and polypyrrole (PPYy interactions on pencil graphite electrodes (PGE). These peaks represent scanning electron microscope (SEM) images of clearly defined tetrahedral HKUST1 crystals enclosed in the PPY matrix [162]. Analysis of BET surface area shows that surface characteristics have been optimized to improve ion adsorption and charge storage capabilities. SEM images show consistent particle distribution and shape, aiding in effective charge transfer and electrochemical durability. From **Fig.3.41** a mass loading of 3 mg for M4@PPY/PGE electrodes is determined as the best option, considering both SEM and BET analyses, in order to balance structural integrity and improve electrochemical performance [110].

Fig. 3.41 shows that the presence of zinc acetate in M4@PPY/PGE electrodes alters their redox behavior, resulting in increased ion exchange capacity and electrochemical activity. Optimal pore structure and higher ion storage capacity, as shown by BET surface area measurements, contribute to improved electrochemical performance. SEM images at **Fig.3.42** show smaller and evenly dispersed particles, suggesting enhanced surface interactions that are advantageous for electrochemical reactions [112]. The addition of zinc to HKUST1 improves electrode durability and ion availability, with 10 mg found to be the best mass for M5@PPy/PGE electrodes based on SEM and BET studies.

a)



b)

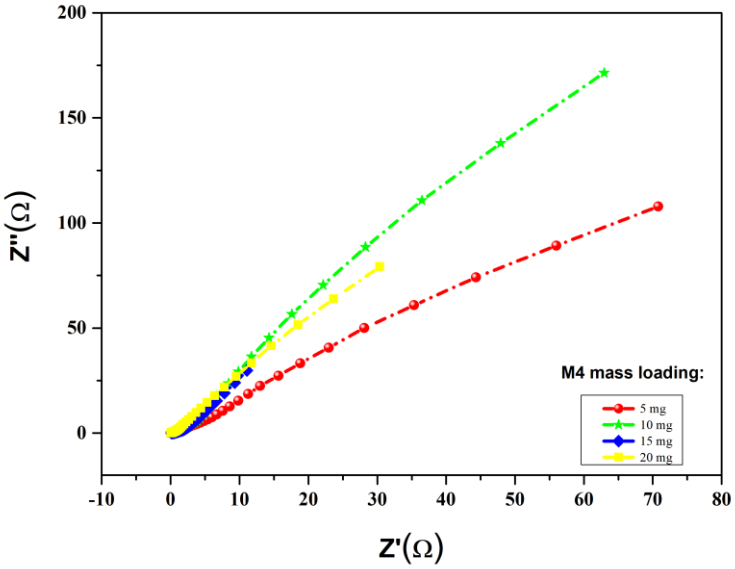
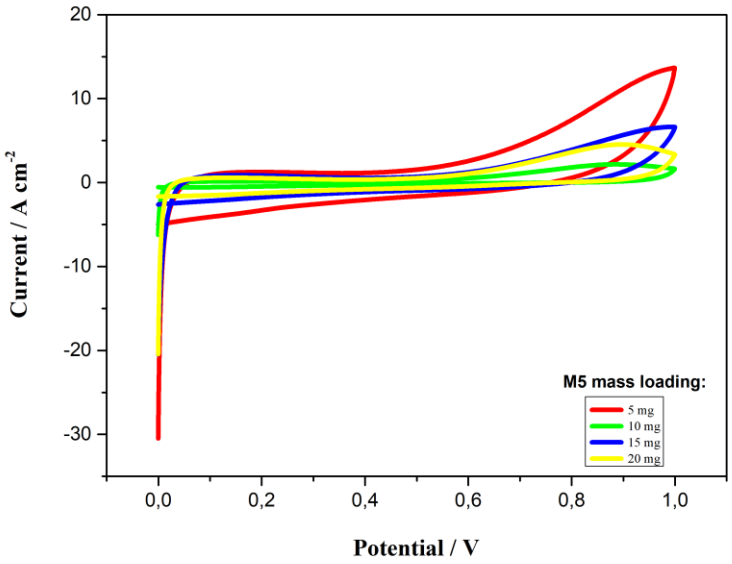


Figure 3.41. Cyclic voltammograms and EIS spectrums of M4@PPy/PGE different amounts of MOF compounds

a)



b)

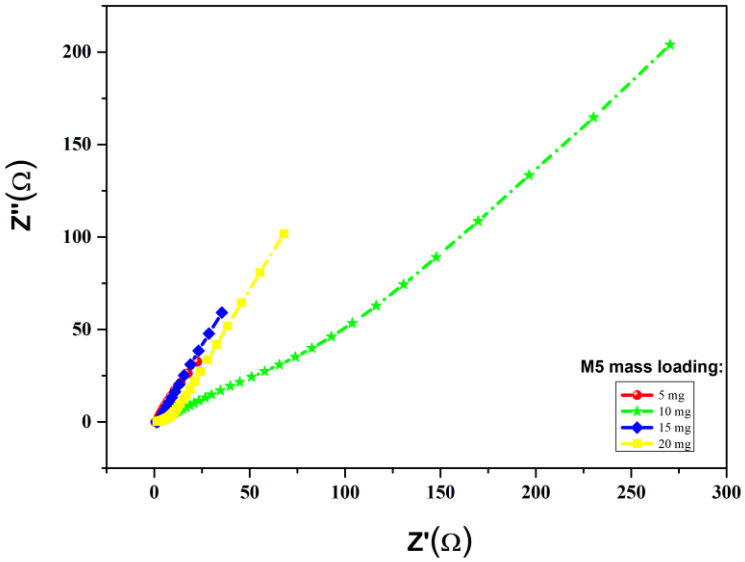
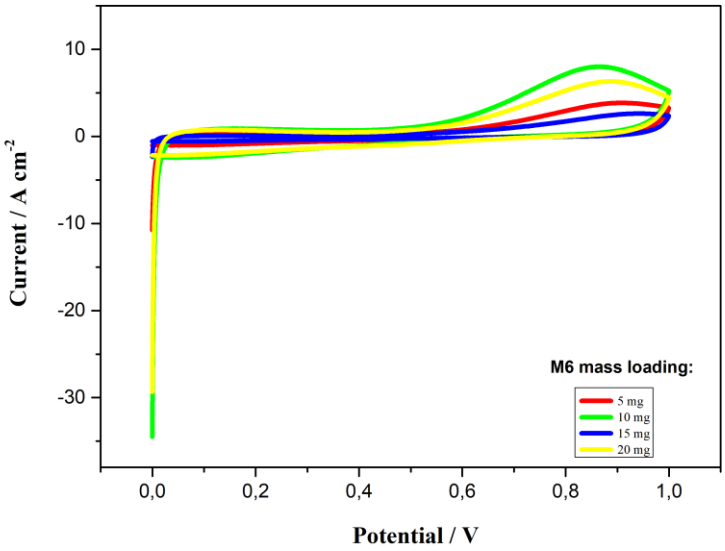


Figure 3.42 Cyclic voltammograms and EIS spectrums of M5@PPy/PGE different amounts of MOF compounds

a)



b)

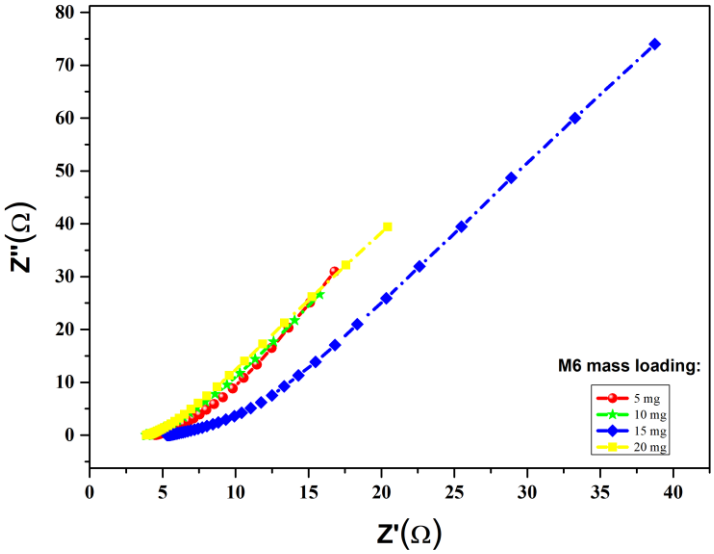


Figure 3.43. Cyclic voltammograms and EIS spectrums of M6@PPy/PGE different amounts of MOF compounds

The CV for M6@PPy/PGE ideally show a large capacitive current, indicating high capacitance **(Fig.3.43.a).** M6@PPy/PGE shows broader or less defined peaks, it might suggest some issues with the integration of the MOF within the polypyrrole matrix. And it indicates poor interaction between M6 and polypyrrole or dispersion of the MOF within the polymer matrix.

A larger semicircle in the Nyquist plot would be indicative of higher charge transfer resistance. A less steep slope or a more sloped line in the low-frequency region

could suggest lower capacitance and less effective capacitive behavior **(Fig.3.41.b., Fig.3.42.b.** and **Fig.3.43.b.).**

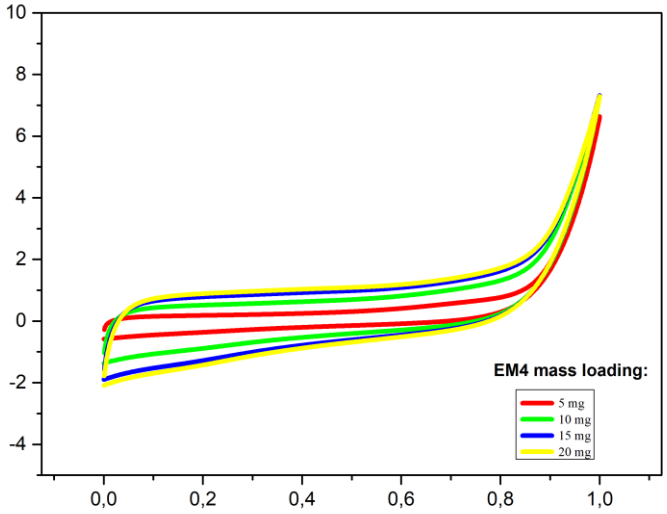
The differences in elemental composition between M4, M5 and M6 demonstrate how MOFs can adjust to various metal ions while maintaining their structural stability. Understanding how metal substitutions impact the properties and performance of MOFs in applications like catalysis and gas separation is important [62].

- **Electrochemical Analysis of the ED modified EM4, EM5 and EM6 Group**

EIS data at **Fig. 3.44** shows unique impedance patterns that suggest improved kinetics of charge transfer and stability in ED treated M4@PPy/PGE electrodes. The increased BET surface area and greater pore volume in EM4 indicate it has more potential for gas adsorption and catalytic processes compared to EM5.

Scanning electron microscopy images show clear structure and distribution of particles, enhancing electrode efficiency. SEM and BET analyses confirm that a mass loading of 10 mg is ideal for the electrodes made of EM4@PPY/PGE, striking a balance between structural integrity and electrochemical efficiency.

a)



b)

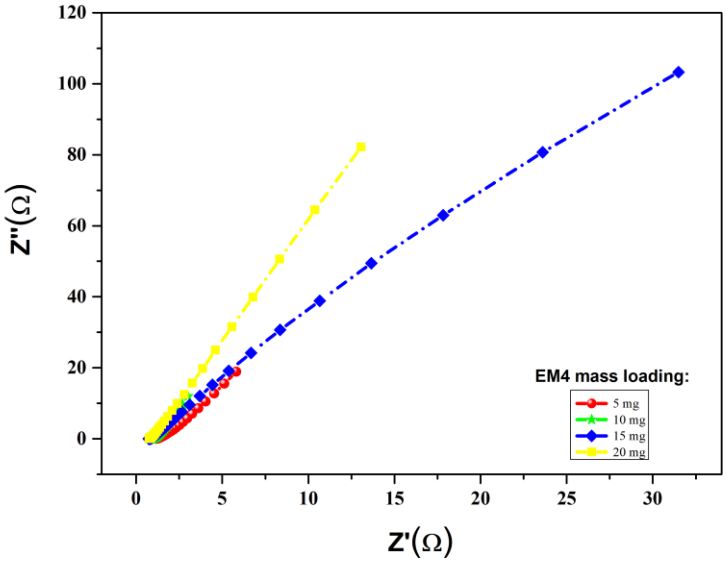
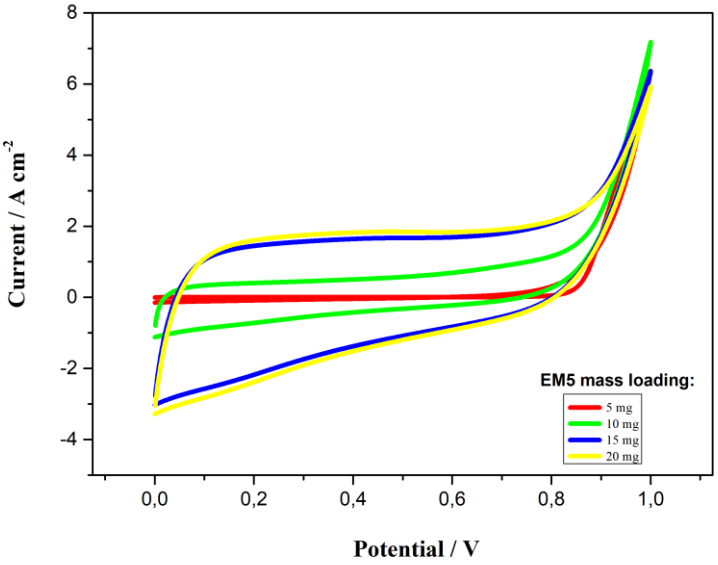


Figure 3.44. Cyclic voltammograms and EIS spectrums of EM4@PPy/PGE different amounts of MOF compounds

a)



b)

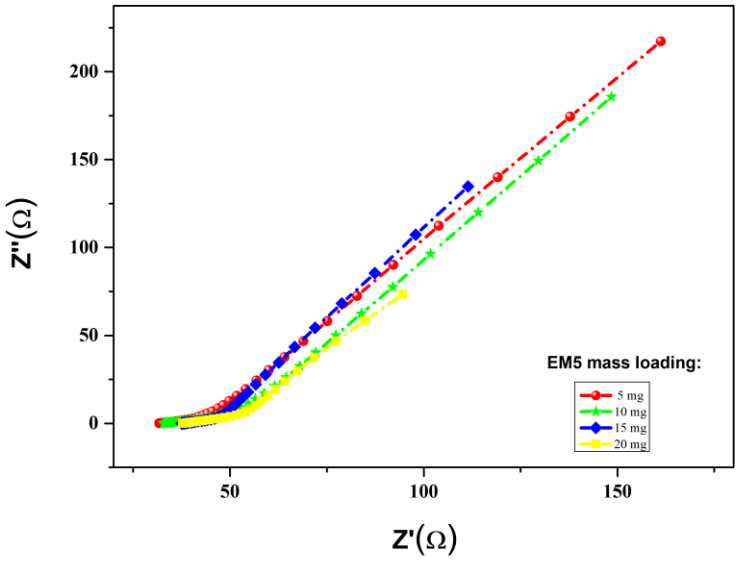
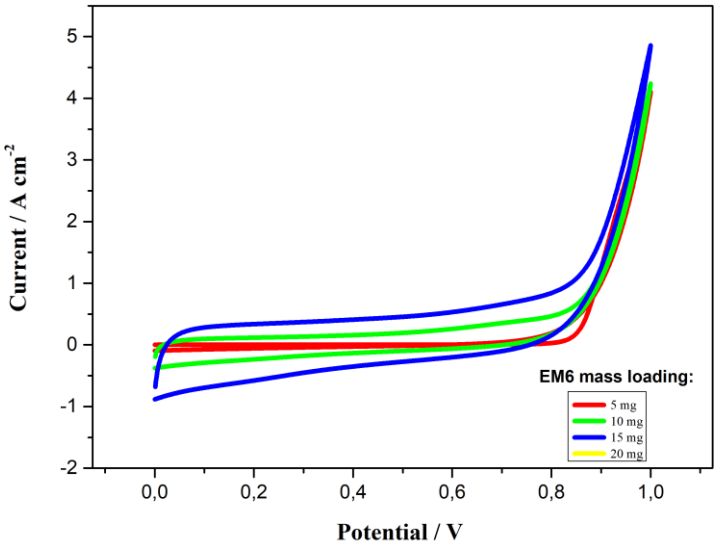


Figure 3.45. Cyclic voltammograms and EIS spectrums of EM5@PPy/PGE different amounts of MOF compounds

a)



b)

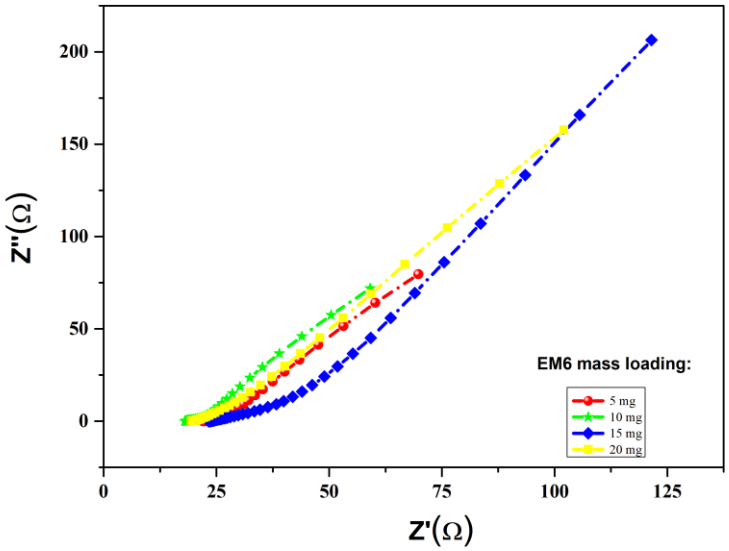


Figure 3.46. Cyclic voltammograms and EIS spectrums of EM6@PPy/PGE different amounts of MOF compounds

SEM analysis at **Fig. 3.45** shows improved particle sizes and distribution, enhancing surface interactions important for electrochemical processes. The combination of zinc and ED improves electrode stability and ion accessibility, with 10 mg being the most effective mass loading for EM5@PPy/PGE electrodes based on SEM and BET findings. The electrode functionality for advanced electrochemical applications is improved by the combined alterations of cobalt and ethylenediamine. SEM and BET findings suggest that a mass loading of 10 mg is the best choice for EM6@PPY/PGE electrodes, striking a balance between structural integrity and improvements in electrochemical performance **(Fig. 3.46).**

3.3 Supercapacitor Application of the Electrodes

The presence of amine groups introduced by ED modification can facilitate faster electron transfer within the material. This improvement in charge transfer kinetics enhances the material's conductivity and reduces internal resistance, contributing to improved performance in supercapacitors [122].

To evaluate the areal capacity performance of MOF@PPy/PGE and ED-MOF@PPy/PGE over 1000 cycles, galvanostatic charge-discharge tests were

conducted **(Fig.3.47).** The cyclic stability of conductive polymers often suffers from molecular chain expansion and contraction during charge-discharge cycles. To address these stability challenges, ED-MOF has been integrated into PPy composites. Incorporating ED into polymers or composites can enhance mechanical strength and electrical conductivity, broadening their application scope. Additionally, ED doping serves as coordination sites for metal ions, leading to functional materials with catalytic activity and ion exchange capabilities. Incorporating ED into MOFs may enhance charge storage capacity and electrochemical stability, altering the electrochemical behavior and making them suitable for supercapacitor applications.

The observed decrease in capacitance over cycles in MOF@PPy/PGE can be attributed to various factors, including the presence of functional groups that interact with electrolyte ions, influencing ion adsorption/desorption at the electrode-electrolyte interface and overall ionic charge storage capacity. **Figure 3.47** illustrates the evolving areal capacitance behavior of electrodes over 1000 cycles. All electrodes utilize a porous active material as a current collector, facilitating electrical conduction into the surrounding environment. ED-MOF@PPy/PGE benefits from enhanced specific surface area, improving ion transport and electrical conductivity of the active material, thereby enabling higher energy storage capacities. These differences in ion charge behavior are primarily influenced by ethylenediamine's role in modifying surface functional groups and their chemical affinity towards ions, resulting in varying degrees of ion adsorption/desorption and ionic charge storage. The porosity and surface area of organic electrodes crucially affect ion-accessible surface area and ion diffusion kinetics. Higher porosity and surface area provide more active sites for ion adsorption/desorption, enhancing ionic charge storage capacity. Supported by pore size results, ED-MOF@PPy/PGE exhibits smaller ions with higher mobility and greater charge storage capacity.

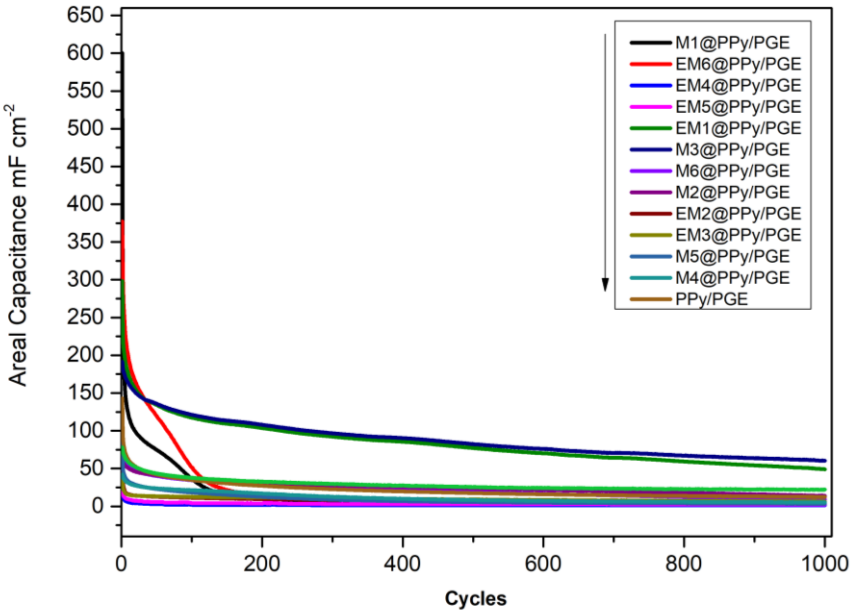


Figure 3.47. Comparison of the areal capacitance of all synthesized MOF based electrodes for 1000 cycles

To evaluate the electrochemical performance of various MOF@PPy/PGE electrodes, galvanostatic charge-discharge tests were conducted over 1000 cycles at 1 mA.cm^{-2} charge/discharge current density **(Table 3.15).** The initial areal capacitance of PPy/PGE was 77.4 mF cm^{-2}. Incorporation of M1@PPy/PGE significantly enhanced the areal capacitance to 575.2 mF cm^{-2}, attributed to its high surface area and ion accessibility. This enhancement underscores its potential for stable performance in acidic environments crucial for electrochemical supercapacitors. In contrast, M2@PPy/PGE exhibited a lower capacitance of 183.9 mF cm^{-2} due to differences in structural characteristics.

Similarly, M3@PPy/PGE demonstrated areal capacitance of 232.9 mF cm^{-2}, respectively, reflecting the influence of cobalt substitution on electrochemical performance and acid stability. EM2@PPy/PGE and EM3@PPy/PGE showed capacitances of 234.4 mF cm^{-2} and 127 mF cm^{-2}, respectively, highlighting the impact of different metal centers on capacitive behavior and acid resistance.

Table 3.15. GCD values comparison of all electrodes at 1 mA.cm^{-2} charge/discharge current density

Produced Electrode	***Areal Capacitance***
E	77.4 mF cm^{-2}
M1	575,2 mF cm^{-2}
M2	183,9 mF cm^{-2}
M3	232,9 mF cm^{-2}
EM1	234.4 mF cm^{-2}
EM2	159,7 mF cm^{-2}
EM3	127 mF cm^{-2}
M4	107,4 mF cm^{-2}
M5	113,2 mF cm^{-2}
M6	186,9 mF cm^{-2}
EM4	459 mF cm^{-2}
EM5	287,5 mF cm^{-2}
EM6	570 mF cm^{-2}

For PPy/PGE electrodes, M1@PPy/PGE, M2@PPy/PGE, M3@PPy/PGE, EM1@PPy/PGE, EM2@PPy/PGE, and EM3@PPy/PGE demonstrated areal capacitances of 575.2 mF cm^{-2}, 183.9 mF cm^{-2}, 232.9 mF cm^{-2}, 234.4 mF cm^{-2}, 159.7 mF cm^{-2}, and 127 mF cm^{-2}, respectively. These enhancements are attributed to ethylenediamine modification, which improves ion exchange properties,

electrochemical stability in acidic environments, and overall performance in supercapacitor applications.

Furthermore, M4@PPy/PGE, M5@PPy/PGE, M6@PPy/PGE, EM4@PPy/PGE, EM5@PPy/PGE, and EM6@PPy/PGE demonstrated areal capacitances of 107.4 mF cm^{-2}, 113.2 mF cm^{-2}, 186.9 mF cm^{-2}, 459 mF cm^{-2}, 287.5 mF cm^{-2}, and 570 mF cm^{-2}, respectively, showcasing the synergistic effects of ethylenediamine modification on enhancing charge storage capacity, stability in acid environments, and performance in supercapacitor applications.

Among M1@PPy/PGE, M2@PPy/PGE, M3@PPy/PGE, EM1@PPy/PGE, EM2@PPy/PGE, and EM3@PPy/PGE has the highest capacitance of 575.2 mF cm^{-2}. Among M4@PPy/PGE, M5@PPy/PGE, M6@PPy/PGE, EM4@PPy/PGE, EM5@PPy/PGE, and EM6@PPy/PGE exhibits the highest capacitance of 570 mF cm^{-2}. Therefore, M1@PPy/PGE and EM6@PPy/PGE are the best performers within their respective groups based on the provided data.

In summary, the integration of MOF materials into PPy/PGE electrodes demonstrates tailored electrochemical properties crucial for various applications, particularly in acidic conditions relevant to supercapacitors. The customized electrochemical properties of ED modified composites are highlighted through electrochemical analysis, with a notable impact from ethylenediamine (ED) modification. SEM and BET analyses offer crucial structural insights that enhance understanding of observed electrochemical reactions, emphasizing the significance of surface morphology and ion accessibility in improving electrode performance for a wide range of technological uses.

4
CONCLUSION

In presented work, metal organic frameworks including polyprrole based conducting polymers were synthesized and used as electrode materials of supercapacitors.

Twelve metal organic frameworks (MOFs) were synthesized using various metal salts and organic ligands, following established solvothermal procedures. The metal salts and ligands were selected to produce two distinct groups: one using 1,4-benzenedicarboxylic acid and the other using 1,3,5-benzenetricarboxylic acid as the organic linkers. Additionally, ethylenediamine was introduced as a modulating agent in half of the synthesized MOFs to examine its effect on framework properties.

During the initial phase of the research, the impact of variables like acid concentration, monomer concentration, and cyclic number on the electrodes' capacitive behaviors was examined using CV and EIS analysis. The cyclic voltammograms of the electrodes that were prepared using varying concentrations of pyrrole. The solution containing 0.5 M pyrrole and 0.1 M sulfuric acid exhibited the highest peak current and capacity. As the amount of monomer increased, the polymerization degree also increased, leading to a noticeable improvement in the capacitive properties of the electrodes prepared with pyrrole concentrations ranging from 0.05 M to 0.5 M. Nevertheless, exfoliation of polypyrrole commenced at the electrode surface once the monomer concentration exceeded 0.5 M. This also suggests improved capacitive properties in this electrode. Therefore, the best number of cycles for preparing the electrode using cyclic voltammetry was determined to be 10 for creating a metal organic framework.

The MOF class offers readily available specific binding spots thanks to their high concentration of unsaturated metal centers and circular pore geometry. To evaluate the electrochemical performance of these composites as electrodes for energy storage applications by utilizing the enormous interior surface area of MOFs as a substrate for popular pseudocapacitive polymer: Polypyyrole.

Developing and characterizing new electrode materials with improved electrochemical performance and energy storage capabilities for supercapacitors. This can involve synthesizing or modifying materials such as metal oxides, conducting polymers, carbon-based materials, or metal organic frameworks (MOFs).

Developing novel approaches for the production of electrodes in order to enhance the efficiency, manufacturability and reliability of supercapacitor electrodes. Performing comprehensive electrochemical testing to assess the efficiency of the supercapacitor electrodes. Evaluating parameters such as specific capacitance, energy density, power density, cyclic stability, rate capability and impedance behavior are included in this evaluation. Comparison with modern materials or devices available in the industry would help support the progress made.

Determining and explaining the charge storage mechanisms of the synthesized electrode materials. This may be comprehensibly performed by employing diverse methodologies and tools of investigation; including simulation, experimentation, and evaluation of electrochemical data to deduce how much contribution comes from each attribute including double-layer capacitance, pseudocapacitance, ion diffusion, and surface reactions.

The particular aims of this the work are to develop, produce and improve supercapacitor devices comprising the newly created electrode materials. It includes integration of electrode and capacitor electrodes with the proper current collectors and separators in order to create supercapacitor devices of specific configuration for maximum performance.

REFERENCES

[1] R. Noack, *Human Energy Requirements. A manual for planners and nutritionists*, 45th ed. Oxford, New York: Oxford University Press, 1991.

[2] W. Energy, C. Turkish, N. Committee, and Q. S. Group, "TURKEY ' S DAILY FINAL ENERGY CONSUMPTION AND ITS RESULTS," no. September, pp. 1–2, 2017.

[3] W. Energy, C. Turkish, N. Committee, and Q. W. Group, "SHIFTING ENERGY DEMAND BALANCES IN," no. April, pp. 1–3, 2018.

[4] Y. Yang, S. Bremner, C. Menictas, and M. Kay, "Battery energy storage system size determination in renewable energy systems: A review," *Renew. Sustain. Energy Rev.*, vol. 91, pp. 109–125, Aug. 2018.

[5] O. Krishan and S. Suhag, "An updated review of energy storage systems: Classification and applications in distributed generation power systems incorporating renewable energy resources," *Int. J. Energy Res.*, vol. 43, no. 12, pp. 6171–6210, Oct. 2019.

[6] P. Moriarty and D. Honnery, "What is the global potential for renewable energy?," *Renew. Sustain. Energy Rev.*, vol. 16, no. 1, pp. 244–252, 2012.

[7] A. Qazi *et al.*, "Towards Sustainable Energy: A Systematic Review of Renewable Energy Sources, Technologies, and Public Opinions," *IEEE Access*, vol. 7, pp. 63837–63851, 2019.

[8] Q. Xu and T. Kobayashi, *Advanced materials for clean energy*. 2015.

[9] N. S. Lewis, "Solar Energy Use," *Science (80-.).*, vol. 798, no. 2007, pp. 798–801, 2012.

[10] R. Korthauer, *Lithium-ion batteries: Basics and applications*. 2018.

[11] J. Jiang and C. Zhang, *Fundamentals and application of lithium-ion batteries in electric drive vehicles*. 2015.

[12] C. Julien, A. Mauger, A. Vijh, and K. Zaghib, *Lithium Batteries: Science and Technology*. 2015.

[13] J. A. Harrison, “Electrochemical Power Sources,” *Electron. Power*, vol. 27, no. 4, p. 333, 1981.

[14] Z. He and Y. Liu, “Fundamentals of - Lithium-Ion Supercapacitors,” pp. 1–11.

[15] R. Kötz and M. Carlen, “Principles and applications of electrochemical capacitors,” *Electrochim. Acta*, vol. 45, no. 15, pp. 2483–2498, 2000.

[16] T. Waldmann, M. Wilka, M. Kasper, M. Fleischhammer, and M. Wohlfahrt-Mehrens, “Temperature dependent ageing mechanisms in Lithium-ion batteries - A Post-Mortem study,” *J. Power Sources*, vol. 262, pp. 129–135, 2014.

[17] S. Zhang and N. Pan, “Supercapacitors Performance Evaluation,” *Adv. Energy Mater.*, vol. 5, no. 6, Mar. 2015.

[18] W. Yan and Q. Shao, “Anodes of Lithium-Ion Supercapacitors,” *Lithium-Ion Supercapacitors*, pp. 13–37, 2018.

[19] X. Chen, H. Lin, P. Chen, G. Guan, J. Deng, and H. Peng, “Smart, stretchable supercapacitors,” *Adv. Mater.*, vol. 26, no. 26, pp. 4444–4449, 2014.

[20] P. Simon, Y. Gogotsi, and B. Dunn, “Where do batteries end and supercapacitors begin?,” *Science*, vol. 343, no. 6176. pp. 1210–1211, 2014.

[21] H. Budde-Meiwes *et al.*, “A review of current automotive battery technology and future prospects,” *Proc. Inst. Mech. Eng. Part D J. Automob. Eng.*, vol. 227, no. 5, pp. 761–776, May 2013.

[22] A. Chandra, “Supercapacitors: An alternate technology for energy storage,” *Proc. Natl. Acad. Sci. India Sect. A - Phys. Sci.*, vol. 82, no. 1, pp. 79–90, 2012.

[23] L. L. Zhang and X. S. Zhao, “Carbon-based materials as supercapacitor electrodes,” *Chem. Soc. Rev.*, vol. 38, no. 9, pp. 2520–2531, 2009.

[24] P. Forouzandeh and S. C. Pillai, “Two-dimensional (2D) electrode materials for supercapacitors,” in *Materials Today: Proceedings*, 2020, vol. 41, pp. 498–505.

[25] R. Kumar *et al.*, “An overview of recent progress in nanostructured carbon-

based supercapacitor electrodes: From zero to bi-dimensional materials," *Carbon N. Y.*, vol. 193, pp. 298–338, 2022.

[26] Y. Tao *et al.*, "Few-layer phosphorene: An emerging electrode material for electrochemical energy storage," *Appl. Mater. Today*, vol. 15, pp. 18–33, 2019.

[27] K. Namsheer, S. Kapse, M. Manoj, R. Thapa, and C. S. Rout, "2D-black phosphorus/polyaniline hybrids for efficient supercapacitor and hydrogen evolution reaction applications," *Sustain. Energy Fuels*, vol. 6, no. 18, pp. 4285–4298, 2022.

[28] O. Yilmaz, H. Y. Kalyon, M. Gencten, and Y. Sahin, "One step production of phosphorene from red phosphorus and investigation of their supercapacitor applications with conducting polymers," *J. Energy Storage*, vol. 79, p. 110133, 2024.

[29] Poonam, K. Sharma, A. Arora, and S. K. Tripathi, "Review of supercapacitors: Materials and devices," *Journal of Energy Storage*. 2019.

[30] P. Simon, T. Brousse, and F. Favier, *Supercapacitors based on carbon or pseudocapacitive materials*. 2017.

[31] D. P. Dubal and R. Holze, "Synthesis, properties, and performance of nanostructured metal oxides for supercapacitors," *Pure Appl. Chem.*, vol. 86, no. 5, pp. 611–632, May 2014.

[32] J. Wang, J. Polleux, J. Lim, and B. Dunn, "Pseudocapacitive Contributions to Electrochemical Energy Storage in TiO 2 (Anatase) Nanoparticles," *J. Phys. Chem. C*, vol. 111, no. 40, pp. 14925–14931, Oct. 2007.

[33] X. Li and B. Wei, "Supercapacitors based on nanostructured carbon," *Nano Energy*, vol. 2, no. 2, pp. 159–173, Mar. 2013.

[34] J. Sung and C. Shin, "Recent Studies on Supercapacitors with Next-Generation Structures," *Micromachines*, vol. 11, no. 12. 2020.

[35] P. Forouzandeh, V. Kumaravel, and S. C. Pillai, "Electrode Materials for Supercapacitors: A Review of Recent Advances," *Catalysts*, vol. 10, no. 9, p. 969, Aug. 2020.

[36] P. Sharma and T. S. Bhatti, “A review on electrochemical double-layer capacitors,” *Energy Convers. Manag.*, vol. 51, no. 12, pp. 2901–2912, Dec. 2010.

[37] A. Laforgue *et al.*, “Activated Carbon/Conducting Polymer Hybrid Supercapacitors,” *J. Electrochem. Soc.*, vol. 150, no. 5, p. A645, 2003.

[38] M. Miyake, “Chapter 26 - Electrochemical Functions,” E. YASUDA, M. INAGAKI, K. KANEKO, M. ENDO, A. OYA, and Y. B. T.-C. A. TANABE, Eds. Oxford: Elsevier Science, 2003, pp. 435–445.

[39] N. Kocyigit, M. Gencten, M. Sahin, and Y. Sahin, “A novel electrolytes for redox flow batteries: Cerium and chromium couples in aqueous system,” *Int. J. Energy Res.*, vol. 45, no. 11, pp. 16176–16188, Sep. 2021.

[40] Q. Jiang, N. Kurra, M. Alhabeb, Y. Gogotsi, and H. N. Alshareef, “All Pseudocapacitive MXene-RuO2 Asymmetric Supercapacitors,” *Adv. Energy Mater.*, vol. 8, no. 13, pp. 1–10, 2018.

[41] N. I. Jalal, R. I. Ibrahim, and M. K. Oudah, “A review on Supercapacitors: Types and components,” *J. Phys. Conf. Ser.*, vol. 1973, no. 1, 2021.

[42] D. Yang, “Application of Nanocomposites for Supercapacitors: Characteristics and Properties,” *Nanocomposites - New Trends Dev.*, 2012.

[43] H. Lv, Q. Pan, Y. Song, X. X. Liu, and T. Liu, *A Review on Nano-/Microstructured Materials Constructed by Electrochemical Technologies for Supercapacitors*, vol. 12, no. 1. Springer Singapore, 2020.

[44] K. Qi, R. Hou, S. Zaman, Y. Qiu, B. Y. Xia, and H. Duan, “Construction of Metal–Organic Framework/Conductive Polymer Hybrid for All-Solid-State Fabric Supercapacitor,” *ACS Appl. Mater. Interfaces*, vol. 10, no. 21, pp. 18021–18028, May 2018.

[45] S. Banerjee and K. K. Kar, “Conducting Polymers as Electrode Materials for Supercapacitors,” in *Springer Series in Materials Science*, vol. 302, 2020, pp. 333–352.

[46] “A Review on Conducting Polymers-Based Composites for Energy Storage Application,” *J. Chem. Rev.*, vol. 1, no. 1, pp. 19–34, Jan. 2019.

[47] W.-S. Huang, B. D. Humphrey, and A. G. MacDiarmid, “Polyaniline, a novel conducting polymer. Morphology and chemistry of its oxidation and reduction in aqueous electrolytes,” *J. Chem. Soc. Faraday Trans. 1 Phys. Chem. Condens. Phases*, vol. 82, no. 8, p. 2385, 1986.

[48] H. L. Wang, A. G. MacDiarmid, Y. Z. Wang, D. D. Gebier, and A. J. Epstein, “Application of polyaniline (emeraldine base, EB) in polymer light-emitting devices,” *Synth. Met.*, vol. 78, no. 1, pp. 33–37, Mar. 1996.

[49] H. Itoi *et al.*, “Electrochemical polymerization of pyrene and aniline exclusively inside the pores of activated carbon for high-performance asymmetric electrochemical capacitors,” *Nanoscale*, vol. 10, no. 20, pp. 9760–9772, 2018.

[50] R. Noriega *et al.*, “A general relationship between disorder, aggregation and charge transport in conjugated polymers,” *Nat. Mater.*, vol. 12, no. 11, pp. 1038–1044, 2013.

[51] A. M. Bryan, L. M. Santino, Y. Lu, S. Acharya, and J. M. D’Arcy, “Conducting Polymers for Pseudocapacitive Energy Storage,” *Chem. Mater.*, vol. 28, no. 17, pp. 5989–5998, Sep. 2016.

[52] J. B. Kaushal, P. Raut, and S. Kumar, “Organic Electronics in Biosensing: A Promising Frontier for Medical and Environmental Applications,” *Biosensors*, vol. 13, no. 11, pp. 1–48, 2023.

[53] I. Sapurina and J. Stejskal, “The mechanism of the oxidative polymerization of aniline and the formation of supramolecular polyaniline structures,” *Polym. Int.*, vol. 57, no. 12, pp. 1295–1325, Dec. 2008.

[54] X. Zhan and D. Zhu, “Conjugated polymers for high-efficiency organic photovoltaics,” *Polym. Chem.*, vol. 1, no. 4, pp. 409–419, 2010.

[55] M. B. Arvas, M. Gençten, and Y. Sahin, “A two-dimensional material for high capacity supercapacitors: S-doped graphene,” *Int. J. Energy Res.*, vol. 44, no. 3, pp. 1624–1635, Mar. 2020.

[56] A. Ç. Arslan and E. Hür, “Supercapacitor applications of polyaniline and poly(n-methylaniline) coated pencil graphite electrode,” *Int. J. Electrochem. Sci.*, vol. 7, no. 12, pp. 12558–12572, 2012.

[57] A. Eftekhari, L. Li, and Y. Yang, “Polyaniline supercapacitors,” *J. Power Sources*, vol. 347, pp. 86–107, 2017.

[58] S. B. Aziz, T. J. Woo, M. F. Z. Kadir, and H. M. Ahmed, “A conceptual review on polymer electrolytes and ion transport models,” *J. Sci. Adv. Mater. Devices*, vol. 3, no. 1, pp. 1–17, 2018.

[59] A. Abd-Elwahed and R. Holze, “Ion size and size memory effects with electropolymerized polyaniline,” *Synth. Met.*, vol. 131, no. 1–3, pp. 61–70, 2002.

[60] M. Kamran, H. Ullah, A.-H. A. Shah, S. Bilal, A. A. Tahir, and K. Ayub, “Combined experimental and theoretical study of poly(aniline-co-pyrrole) oligomer,” *Polymer (Guildf).*, vol. 72, pp. 30–39, 2015.

[61] H. Gholami, A. Shakeri, and V. Saadattalab, “Investigation of physical and mechanical properties of polyaniline/MMT nanocomposites,” *Curr. Chem. Lett.*, vol. 6, no. 4, 2017.

[62] N. Patterson, B. Xiao, and A. Ignaszak, “Polypyrrole decorated metal-organic frameworks for supercapacitor devices,” *RSC Adv.*, vol. 10, no. 34, pp. 20162–20172, 2020.

[63] Y. Ge *et al.*, “A facile approach for fabrication of mechanically strong graphene/polypyrrole films with large areal capacitance for supercapacitor applications,” *RSC Adv.*, vol. 5, no. 124, pp. 102643–102651, 2015.

[64] L. Zhang *et al.*, “Advanced Matrixes for Binder-Free Nanostructured Electrodes in Lithium-Ion Batteries,” *Adv. Mater.*, vol. 32, no. 24, 2020.

[65] F. Xu, X. Chen, Z. Tang, D. Wu, R. Fu, and D. Jiang, “Redox-active conjugated microporous polymers: A new organic platform for highly efficient energy storage,” *Chem. Commun.*, vol. 50, no. 37, pp. 4788–4790, 2014.

[66] R. Chen, M. Yu, R. P. Sahu, I. K. Puri, and I. Zhitomirsky, “The Development of Pseudocapacitor Electrodes and Devices with High Active Mass Loading,” *Adv. Energy Mater.*, vol. 10, no. 20, p. 1903848, May 2020.

[67] H. Jia *et al.*, “In situ anodic electrodeposition of two-dimensional conductive metal-organic framework@nickel foam for high-performance flexible

supercapacitor," *J. Power Sources*, vol. 526, no. January, p. 231163, 2022.

[68] H. Y. Kalyon, O. Yilmaz, M. Gencten, S. Gorduk, and Y. Sahin, "Ethylenediamine-Functionalized Metal-Organic Frameworks for Applications of Electrochemical Supercapacitors as an Additive," *Synth. Met.*, p. 117627, 2024.

[69] H. Yildirim Kalyon, M. Gencten, S. Gorduk, and Y. Sahin, "Novel composite materials consisting of polypyrrole and metal organic frameworks for supercapacitor applications," *J. Energy Storage*, p. 103699, 2021.

[70] Z. Neisi, Z. Ansari-Asl, S. Jafarinejad-Farsangi, M. E. Tarzi, T. Sedaghat, and V. Nobakht, "Synthesis, characterization and biocompatibility of polypyrrole/Cu(II) metal-organic framework nanocomposites," *Colloids Surfaces B Biointerfaces*, vol. 178, no. March, pp. 365–376, 2019.

[71] W. Kukulka, K. Cendrowski, and E. Mijowska, "Electrochemical performance of MOF-5 derived carbon nanocomposites with 1D, 2D and 3D carbon structures," *Electrochim. Acta*, vol. 307, pp. 582–594, 2019.

[72] R. C. K. Reddy, X. Lin, A. Zeb, and C. Y. Su, *Metal–Organic Frameworks and Their Derivatives as Cathodes for Lithium-Ion Battery Applications: A Review*, vol. 5, no. 2. Springer Singapore, 2022.

[73] Y. Kang *et al.*, "Binder-Free Electrodes and Their Application for Li-Ion Batteries," *Nanoscale Res. Lett.*, vol. 15, no. 1, 2020.

[74] M. Yu, L. Zhang, X. He, H. Yu, J. Han, and M. Wu, "3D interconnected porous carbons from MOF-5 for supercapacitors," *Mater. Lett.*, vol. 172, pp. 81–84, 2016.

[75] S. Kitagawa, R. Kitaura, and S. Noro, "Functional Porous Coordination Polymers," *Angew. Chemie Int. Ed.*, vol. 43, no. 18, pp. 2334–2375, Apr. 2004.

[76] A. Y. Robin and K. M. Fromm, "Coordination polymer networks with O- and N-donors: What they are, why and how they are made," *Coord. Chem. Rev.*, vol. 250, no. 15–16, pp. 2127–2157, Aug. 2006.

[77] N. Tahir, C. Krishnaraj, K. Leus, and P. Van Der Voort, "Development of covalent triazine frameworks as heterogeneous catalytic supports," *Polymers*

(Basel)., vol. 11, no. 8, 2019.

[78] O. M. Yaghi, “MOFs and their energy applications,” 2015.

[79] P. J. Waller, F. Gándara, and O. M. Yaghi, “Chemistry of Covalent Organic Frameworks,” *Acc. Chem. Res.*, vol. 48, no. 12, pp. 3053–3063, 2015.

[80] C. Vaitsis, G. Sourkouni, and C. Argirusis, “Metal Organic Frameworks (MOFs) and ultrasound: A review,” *Ultrason. Sonochem.*, vol. 52, no. November 2018, pp. 106–119, 2019.

[81] V. Sharma, D. K. Das, V. K. Vashistha, R. K. Gupta, G. Yasin, and A. Kumar, “Covalent Organic Frameworks-based Nanocomposites for Oxygen reduction reaction,” *J. Incl. Phenom. Macrocycl. Chem.*, vol. 102, no. 5–6, pp. 477–485, Jun. 2022.

[82] T. H. Yu, C. H. Ho, C. Y. Wu, C. H. Chien, C. H. Lin, and S. Lee, “Metal-organic frameworks: A novel SERS substrate,” *J. Raman Spectrosc.*, vol. 44, no. 11, pp. 1506–1511, 2013.

[83] N. Ashraf, M. Isa khan, A. Majid, M. Rafique, and M. B. Tahir, “A review of the interfacial properties of 2-D materials for energy storage and sensor applications,” *Chinese J. Phys.*, vol. 66, pp. 246–257, 2020.

[84] Z. Y. Gu, J. Q. Jiang, and X. P. Yan, “Fabrication of isoreticular metal-organic framework coated capillary columns for high-resolution gas chromatographic separation of persistent organic pollutants,” *Anal. Chem.*, vol. 83, no. 13, pp. 5093–5100, 2011.

[85] V. H. Nguyen *et al.*, “Synthesis and characterization of zinc-organic frameworks with 1,4-benzenedicarboxylic acid and azobenzene-4,40-dicarboxylic acid,” *Adv. Nat. Sci. Nanosci. Nanotechnol.*, vol. 2, no. 2, 2011.

[86] S. Xiong *et al.*, “A high-performance hybrid supercapacitor with NiO derived NiO@Ni-MOF composite electrodes,” *Electrochim. Acta*, vol. 340, p. 135956, 2020.

[87] H. Al-Kutubi, J. Gascon, E. J. R. Sudhölter, and L. Rassaei, “Electrosynthesis of Metal-Organic Frameworks: Challenges and Opportunities,” *ChemElectroChem*, vol. 2, no. 4, pp. 462–474, 2015.

[88] X. Shi, Y. Shan, M. Du, and H. Pang, “Synthesis and application of metal-organic framework films,” *Coord. Chem. Rev.*, vol. 444, p. 214060, 2021.

[89] F. Luo, “Stability Improvement Methods and Application Progress of Metal-Organic Frameworks,” *J. Phys. Conf. Ser.*, vol. 1939, no. 1, 2021.

[90] J. M. Rotter *et al.*, “Covalent Organic Framework Films through Electrophoretic Deposition - Creating Efficient Morphologies for Catalysis,” *Chem. Mater.*, vol. 31, no. 24, pp. 10008–10016, 2019.

[91] F. S. Ke, Y. S. Wu, and H. Deng, “Metal-organic frameworks for lithium ion batteries and supercapacitors,” *J. Solid State Chem.*, vol. 223, pp. 109–121, 2015.

[92] Y. Liu, N. Xu, W. Chen, X. Wang, C. Sun, and Z. Su, “Supercapacitor with high cycling stability through electrochemical deposition of metal-organic frameworks/polypyrrole positive electrode,” *Dalt. Trans.*, vol. 47, no. 38, pp. 13472–13478, 2018.

[93] Y. Liu, N. Xu, W. Chen, X. Wang, C. Sun, and Z. Su, “Supercapacitor with high cycling stability through electrochemical deposition of metal–organic frameworks/polypyrrole positive electrode,” *Dalt. Trans.*, vol. 47, no. 38, pp. 13472–13478, 2018.

[94] Y. Liu, N. Xu, W. Chen, X. Wang, C. Sun, and Z. Su, “Supercapacitor with high cycling stability through electrochemical deposition of metal-organic frameworks/polypyrrole positive electrode,” *Dalt. Trans.*, vol. 47, no. 38, pp. 13472–13478, 2018.

[95] S. Hug, M. E. Tauchert, S. Li, U. E. Pachmayr, and B. V. Lotsch, “A functional triazine framework based on N-heterocyclic building blocks,” *J. Mater. Chem.*, vol. 22, no. 28, pp. 13956–13964, 2012.

[96] L. Ronconi and P. J. Sadler, “Using coordination chemistry to design new medicines,” *Coord. Chem. Rev.*, vol. 251, no. 13–14, pp. 1633–1648, 2007.

[97] S. Gu, Z. Bai, S. Majumder, B. Huang, and G. Chen, “Conductive metal–organic framework with redox metal center as cathode for high rate performance lithium ion battery,” *J. Power Sources*, vol. 429, no. January, pp. 22–29, 2019.

[98] R. Díaz, M. G. Orcajo, J. A. Botas, G. Calleja, and J. Palma, “Co8-MOF-5 as electrode for supercapacitors,” *Mater. Lett.*, vol. 68, pp. 126–128, 2012.

[99] A. Martinez Joaristi, J. Juan-Alcañiz, P. Serra-Crespo, F. Kapteijn, and J. Gascon, “Electrochemical synthesis of some archetypical Zn 2+, Cu 2+, and Al 3+ metal organic frameworks,” *Cryst. Growth Des.*, vol. 12, no. 7, pp. 3489–3498, 2012.

[100] F. Ahmadijokani *et al.*, “Ethylenediamine-functionalized Zr-based MOF for efficient removal of heavy metal ions from water,” *Chemosphere*, vol. 264, p. 128466, 2021.

[101] X. Zhang, K. Wan, P. Subramanian, M. Xu, J. Luo, and J. Fransaer, “Electrochemical deposition of metal-organic framework films and their applications,” *J. Mater. Chem. A*, vol. 8, no. 16, pp. 7569–7587, 2020.

[102] Y. Liu *et al.*, “Electrochemical Synthesis of Large Area Two-Dimensional Metal–Organic Framework Films on Copper Anodes,” *Angew. Chemie - Int. Ed.*, vol. 60, no. 6, pp. 2887–2891, 2021.

[103] Z. Chen *et al.*, “A microporous metal-organic framework with immobilized -OH functional groups within the pore surfaces for selective gas sorption,” *Eur. J. Inorg. Chem.*, no. 24, pp. 3745–3749, 2010.

[104] T. M. McDonald, W. R. Lee, J. A. Mason, B. M. Wiers, C. S. Hong, and J. R. Long, “Capture of carbon dioxide from air and flue gas in the alkylamine-appended metal-organic framework mmen-Mg 2(dobpdc),” *J. Am. Chem. Soc.*, vol. 134, no. 16, pp. 7056–7065, 2012.

[105] A. Lieb *et al.*, “MIL-100(V) - A mesoporous vanadium metal organic framework with accessible metal sites,” *Microporous Mesoporous Mater.*, vol. 157, pp. 18–23, 2012.

[106] W. Xia, *Fabrication of Metal–Organic Framework Derived Nanomaterials and Their Electrochemical Applications*, vol. 53, no. 9. 2011.

[107] J. Gong, Z. Xu, Z. Tang, J. Zhong, and L. Zhang, “Highly compressible 3-D hierarchical porous carbon nanotube / metal organic framework / polyaniline hybrid sponges supercapacitors Highly compressible 3-D hierarchical porous carbon nanotube / metal organic framework / polyaniline hybrid

sponges supercapa," vol. 055032, 2019.

[108] D. Andirova, Y. Lei, X. Zhao, and S. Choi, "Functionalization of Metal-Organic Frameworks for Enhanced Stability under Humid Carbon Dioxide Capture Conditions.," *ChemSusChem*, vol. 8, no. 20, pp. 3405–3409, Oct. 2015.

[109] X. Chen *et al.*, "Facile synthesis of polypyrrole@metal-organic framework core-shell nanocomposites for dual-mode imaging and synergistic chemo-photothermal therapy of cancer cells," *J. Mater. Chem. B*, vol. 5, no. 9, pp. 1772–1778, 2017.

[110] E. A. Jafari, M. Moradi, S. Borhani, H. Bigdeli, and S. Hajati, "Fabrication of hybrid supercapacitor based on rod-like HKUST-1@polyaniline as cathode and reduced graphene oxide as anode," *Phys. E Low-dimensional Syst. Nanostructures*, vol. 99, pp. 16–23, 2018.

[111] M. Li, T. Chen, S. Song, Y. Li, and J. Bae, "Hkust-1@il-li solid-state electrolyte with 3d ionic channels and enhanced fast li+ transport for lithium metal batteries at high temperature," *Nanomaterials*, vol. 11, no. 3, pp. 1–14, 2021.

[112] I. Hod *et al.*, "Directed growth of electroactive metal-organic framework thin films using electrophoretic deposition," *Adv. Mater.*, vol. 26, no. 36, pp. 6295–6300, 2014.

[113] X. Su, L. Bromberg, V. Martis, F. Simeon, A. Huq, and T. A. Hatton, "Postsynthetic Functionalization of Mg-MOF-74 with Tetraethylenepentamine: Structural Characterization and Enhanced CO2 Adsorption," *ACS Appl. Mater. Interfaces*, vol. 9, no. 12, pp. 11299–11306, 2017.

[114] C. Chen, J. Kim, D. Park, and W. Ahn, "Ethylenediamine grafting on a zeolite-like metal organic framework (ZMOF) for CO 2 capture," *Mater. Lett.*, vol. 106, pp. 344–347, 2013.

[115] L. P. Zhu, G. H. Liao, N. C. Bing, X. Zhao, and Y. Y. Gu, "Synthesis of monodisperse shuttle-like α-Fe2O3 nanorods via the EDA-assisted method," *Mater. Lett.*, vol. 65, no. 9, pp. 1287–1290, 2011.

[116] A. Asghar *et al.*, “Ethylenediamine loading into a manganese-based metal-organic framework enhances water stability and carbon dioxide uptake of the framework,” *R. Soc. Open Sci.*, vol. 7, no. 3, 2020.

[117] M. L. Chen, Y. Y. Feng, S. Y. Wang, Y. H. Cheng, and Z. H. Zhou, “Metal-Organic Frameworks with Double Channels for Rapid and Reversible Adsorption of 1,2-Ethylenediamine and Gases,” *ACS Appl. Mater. Interfaces*, vol. 12, no. 1, pp. 1412–1418, 2020.

[118] L. Wang *et al.*, “Ethylenediamine-functionalized metal organic frameworks MIL-100(Cr) for efficient CO2/N2O separation,” *Sep. Purif. Technol.*, vol. 235, no. September 2019, p. 116219, 2020.

[119] A. Demessence, D. M. D’Alessandro, M. L. Foo, and J. R. Long, “Strong CO2 binding in a water-stable, triazolate-bridged metal-organic framework functionalized with ethylenediamine,” *J. Am. Chem. Soc.*, vol. 131, no. 25, pp. 8784–8786, 2009.

[120] C. Chen, J. Kim, D. W. Park, and W. S. Ahn, “Ethylenediamine grafting on a zeolite-like metal organic framework (ZMOF) for CO2 capture,” *Mater. Lett.*, vol. 106, pp. 344–347, 2013.

[121] C. G. Carson *et al.*, “Synthesis and structure characterization of copper terephthalate metal-organic frameworks,” *Eur. J. Inorg. Chem.*, no. 16, pp. 2338–2343, 2009.

[122] N. Vrtovec *et al.*, “Structural and CO2Capture Properties of Ethylenediamine-Modified HKUST-1 Metal-Organic Framework,” *Cryst. Growth Des.*, vol. 20, no. 8, pp. 5455–5465, 2020.

[123] R. Vaidhyanathan, S. S. Iremonger, G. K. H. Shimizu, P. G. Boyd, S. Alavi, and T. K. Woo, “Direct observation and quantification of CO2 binding within an amine-functionalized nanoporous solid,” *Science (80-.).*, vol. 330, no. 6004, pp. 650–653, 2010.

[124] L. Zu *et al.*, “Electrochemical prepared phosphorene as a cathode for supercapacitors,” *J. Alloys Compd.*, vol. 770, pp. 26–34, 2019.

[125] A. Cao, Y. Li, Z. Chen, Y. Wang, T. Li, and Y. Han, “Polymerization of polypyrrole nanospheres on carbon nanotubes with PMo12-xWx as oxidant

and redox dopant for supercapacitor," *Polymer (Guildf).*, vol. 204, p. 122829, 2020.

[126] M. B. Arvas, "Hydrothermal synthesis of polypyrrole/dye-functionalized carbon cloth electrode for wide potential window supercapacitor," *Synth. Met.*, vol. 293, no. October 2022, p. 117275, 2023.

[127] T. Basili, H. Yildirim Kalyon, M. Gencten, M. Macit, and Y. Sahin, "High performance supercapacitive behaviors of oximes in a poly(aniline- co -pyrrole) based conducting polymer structure," *New J. Chem.*, vol. 47, no. 2, pp. 691–707, 2023.

[128] O. Gorduk, S. Gorduk, M. Gencten, M. Sahin, and Y. Sahin, "One-step electrochemical preparation of ternary phthalocyanine/acid-activated multiwalled carbon nanotube/polypyrrole-based electrodes and their supercapacitor applications," *Int. J. Energy Res.*, vol. 44, no. 11, pp. 9093–9111, 2020.

[129] C. Karunakaran, R. Rajkumar, and K. Bhargava, "Introduction to Biosensors," *Biosens. Bioelectron.*, no. June, pp. 1–68, 2015.

[130] P. SIMON and Y. GOGOTSI, "Materials for electrochemical capacitors," in *Nanoscience and Technology*, Co-Published with Macmillan Publishers Ltd, UK, 2009, pp. 320–329.

[131] G. Wang, L. Zhang, and J. Zhang, "A review of electrode materials for electrochemical supercapacitors," *Chem. Soc. Rev.*, vol. 41, no. 2, pp. 797–828, 2012.

[132] G. Xu, P. Nie, H. Dou, B. Ding, L. Li, and X. Zhang, "Exploring metal organic frameworks for energy storage in batteries and supercapacitors," *Mater. Today*, vol. 20, no. 4, pp. 191–209, 2017.

[133] H. Yildirim Kalyon, M. Gencten, S. Gorduk, and Y. Sahin, "Novel composite materials consisting of polypyrrole and metal organic frameworks for supercapacitor applications," *Journal of Energy Storage*. p. 103699, 2021.

[134] C. Ma *et al.*, "Carbon nanofiber/graphene composite paper for flexible supercapacitors with high volumetric capacitance," *Mater. Lett.*, vol. 145,

pp. 197–200, 2015.

[135] S. C. Wechsler and F. Z. Amir, “Superior Electrochemical Performance of Pristine Nickel Hexaaminobenzene MOF Supercapacitors Fabricated by Electrophoretic Deposition,” *ChemSusChem*, vol. 13, no. 6, pp. 1491–1495, 2020.

[136] C. C. Lalau and C. T. J. Low, “Electrophoretic Deposition for Lithium-Ion Battery Electrode Manufacture,” *Batter. Supercaps*, vol. 2, no. 6, pp. 551–559, 2019.

[137] T. Kim *et al.*, “(How to read CV for batteries) Applications of voltammetry in lithium ion battery research,” *J. Electrochem. Sci. Technol.*, vol. 11, no. 1, pp. 14–25, 2020.

[138] E. M. Geniès, M. Lapkowski, and J. F. Penneau, “Cyclic voltammetry of polyaniline: interpretation of the middle peak,” *J. Electroanal. Chem. Interfacial Electrochem.*, vol. 249, no. 1–2, pp. 97–107, Jul. 1988.

[139] I. O. K’Owino and O. A. Sadik, “Impedance spectroscopy: A powerful tool for rapid biomolecular screening and cell culture monitoring,” *Electroanalysis*, vol. 17, no. 23, pp. 2101–2113, 2005.

[140] J.-P. Diard, B. Le Gorrec, and C. Montella, “Handbook of Electrochemical Impedance Spectroscopy - Diffusion Impedances,” *Diard, J.-P. Le Gorrec, B. Le Montella, C.*, no. July, p. 30, 2012.

[141] H. Lv, Q. Pan, Y. Song, X. X. Liu, and T. Liu, *A Review on Nano-/Microstructured Materials Constructed by Electrochemical Technologies for Supercapacitors*, vol. 12, no. 1. Springer Singapore, 2020.

[142] M. A. Neelakantan, F. Rusalraj, J. Dharmaraja, S. Johnsonraja, T. Jeyakumar, and M. S. Pillai, “Spectral characterization, cyclic voltammetry, morphology, biological activities and DNA cleaving studies of amino acid Schiff base metal(II) complexes,” *Spectrochim Acta A Mol Biomol Spectrosc*, vol. 71, no. 4, pp. 1599–1609, 2008.

[143] G. Cakmak, Z. Küçükyavuz, and S. Küçükyavuz, “Conductive copolymers of polyaniline, polypyrrole and poly(dimethylsiloxane),” *Synth. Met.*, vol. 151, no. 1, pp. 10–18, 2005.

[144] O. Gorduk, S. Gorduk, M. Gencten, M. Sahin, and Y. Sahin, “One-step electrochemical preparation of ternary phthalocyanine/acid-activated multiwalled carbon nanotube/polypyrrole-based electrodes and their supercapacitor applications,” *Int. J. Energy Res.*, vol. 44, no. 11, pp. 9093–9111, Sep. 2020.

[145] S. Yasa, O. Kumbasi, M. B. Arvas, M. Gencten, M. Sahin, and Y. Sahin, “S-Doped Graphene Oxide/N-Doped Graphene Oxide/PANI: A Triple Composite for High-Performance Supercapacitor Applications,” *ECS J. Solid State Sci. Technol.*, vol. 12, no. 5, p. 051002, May 2023.

[146] C. Carson *et al.*, “Synthesis and Structure Characterization of Copper Terephthalate MetalOrganic Frameworks,” *Eur. J. Inorg. Chem. - EUR J INORG CHEM*, vol. 2009, pp. 2338–2343, Jun. 2009.

[147] M. S. Biserčić, B. Marjanović, B. N. Vasiljević, S. Mentus, B. A. Zasońska, and G. Ćirić-Marjanović, “The quest for optimal water quantity in the synthesis of metal-organic framework MOF-5,” *Microporous Mesoporous Mater.*, vol. 278, pp. 23–29, 2019.

[148] N. Getachew, Y. Chebude, I. Diaz, and M. Sanchez-Sanchez, “Room temperature synthesis of metal organic framework MOF-2,” *J. Porous Mater.*, vol. 21, no. 5, pp. 769–773, 2014.

[149] S. N. Guo *et al.*, “(Metal-Organic Framework)-Polyaniline sandwich structure composites as novel hybrid electrode materials for high-performance supercapacitor,” *J. Power Sources*, vol. 316, pp. 176–182, 2016.

[150] T. Grant Glover, G. W. Peterson, B. J. Schindler, D. Britt, and O. Yaghi, “MOF-74 building unit has a direct impact on toxic gas adsorption,” *Chem. Eng. Sci.*, vol. 66, no. 2, pp. 163–170, 2011.

[151] S. G. Baca, Y. A. Simonov, N. V Gerbeleu, M. Gdaniec, P. N. Bourosh, and G. A. Timco, “Synthesis and X-ray diffraction study of Zn(II) complexes with o-phthalic acid and aromatic amines,” *Polyhedron*, vol. 20, no. 9, pp. 831–837, 2001.

[152] N. B. Colthup, L. H. Daly, and S. E. Wiberley, “Amines, C=N, and N=O

Compounds," *Introduction to Infrared and Raman Spectroscopy*. Academic Press, pp. 339–354, 1990.

[153] H. Y. Liu, K. P. Wang, and H. Teng, "A simplified preparation of mesoporous carbon and the examination of the carbon accessibility for electric double layer formation," *Carbon N. Y.*, vol. 43, no. 3, pp. 559–566, 2005.

[154] A. Hossain, S. K. Seth, A. Bauzá, S. Mukhopadhyay, and A. Frontera, "Coordination polymers based on phthalic acid and aminopyrazine ligands: On the importance of N-H.π interactions," *Polymers (Basel).*, vol. 10, no. 2, 2018.

[155] F. Fusalba and D. Bélanger, "Electropolymerization of Polypyrrole and Polyaniline-Polypyrrole from Organic Acidic Medium," *J. Phys. Chem. B*, vol. 103, no. 42, pp. 9044–9054, 1999.

[156] H. Zhu, H. Liu, I. Zhitomirsky, and S. Zhu, "Preparation of metal-organic framework films by electrophoretic deposition method," *Mater. Lett.*, vol. 142, pp. 19–22, 2015.

[157] L. H. Wu *et al.*, "A novel CdII-based metal-organic framework as a multi-responsive luminescent sensor for Fe3+, MnO4-, Cr2O72-, salicylaldehyde and ethylenediamine detection with high selectivity and sensitivity," *CrystEngComm*, vol. 23, no. 2, pp. 482–491, 2021.

[158] V. V. Matveevskaya *et al.*, "Arene-ruthenium(II) complexes with tetracyclic oxime derivatives: synthesis, structure and antiproliferative activity against human breast cancer cells," *Inorganica Chim. Acta*, vol. 535, p. 120879, May 2022.

[159] A. Alhafez, A. Savci, Y. Alan, R. Soylemez, and A. Kilic, "Preparation of Cu(II), Ni(II), Ti(IV), VO(IV), and Zn(II) Metal Complexes Derived from Novel vic-Dioxime and Investigation of Their Antioxidant and Antibacterial Activities," *Chem Biodivers*, vol. 19, no. 3, p. e202100768, 2022.

[160] S. Kuecken, J. Schmidt, L. Zhi, and A. Thomas, "Conversion of amorphous polymer networks to covalent organic frameworks under ionothermal conditions: A facile synthesis route for covalent triazine frameworks," *J.*

Mater. Chem. A, vol. 3, no. 48, pp. 24422–24427, 2015.

[161] D. W. Jung, D. A. Yang, J. Kim, J. Kim, and W. S. Ahn, "Facile synthesis of MOF-177 by a sonochemical method using 1-methyl-2-pyrrolidinone as a solvent," *Dalt. Trans.*, vol. 39, no. 11, pp. 2883–2887, 2010.

[162] Q. xing Luo, B. wen An, M. Ji, S. E. Park, C. Hao, and Y. qin Li, "Metal–organic frameworks HKUST-1 as porous matrix for encapsulation of basic ionic liquid catalyst: effect of chemical behaviour of ionic liquid in solvent," *J. Porous Mater.*, vol. 22, no. 1, pp. 247–259, 2015.

[163] S. Meijs, C. SØrensen, S. SØrensen, K. Rechendorff, M. Fjorback, and N. J. M. Rijkhoff, "Influence of implantation on the electrochemical properties of smooth and porous TiN coatings for stimulation electrodes," *J. Neural Eng.*, vol. 13, no. 2, p. 26011, 2016.

[164] M. B. Arvas, H. Gürsu, M. Gencten, and Y. Sahin, "New Approach Synthesis of S, N Co-Doped Graphenes for High-Performance Supercapacitors," *ChemistrySelect*, vol. 7, no. 21, p. e202200360, Jun. 2022.

[165] B. Ok, M. Gencten, M. B. Arvas, and Y. Sahin, "Preparation of Copper Doped Conducting Polymers and Their Supercapacitor Applications," *ECS J. Solid State Sci. Technol.*, vol. 11, no. 3, p. 033004, Mar. 2022.

[166] O. Gorduk, M. Gencten, S. Gorduk, M. Sahin, and Y. Sahin, "Electrochemical fabrication and supercapacitor performances of metallo phthalocyanine/functionalized-multiwalled carbon nanotube/polyaniline modified hybrid electrode materials," *J. Energy Storage*, vol. 33, no. October, p. 102049, Jan. 2021.

[167] H. Gürsu, M. Gençten, and Y. Şahin, "One-step electrochemical preparation of graphene-coated pencil graphite electrodes by cyclic voltammetry and their application in vanadium redox batteries," *Electrochim. Acta*, vol. 243, pp. 239–249, 2017.

[168] B. Liang *et al.*, "Poly(aniline-co-pyrrole) on the surface of reduced graphene oxide as high-performance electrode materials for supercapacitors," *Electrochim. Acta*, vol. 177, pp. 335–342, 2015.

[169] T. Basili, H. Yildirim Kalyon, M. Gencten, M. Macit, and Y. Sahin, "High

performance supercapacitive behaviors of oximes in a poly(aniline-co-pyrrole) based conducting polymer structure," *New J. Chem.*, vol. 47, no. 2, pp. 691–707, 2023.

[170] and M. J. K. H. Tian, S. G. Corcoran, C. E. Reece, "An Introduction to Electrochemical Impedance Measurement An Introduction to Electrochemical Impedance Measurement," *J. Electrochem. Soc.*, vol. 155, no. 9, pp. D563–D568, 2008.

[171] H. Yamashita and H. Li, *Nanostructured photocatalysts : advanced functional materials*. 2016.

[172] R. Turczyn, K. Krukiewicz, A. Katunin, J. Sroka, and P. Sul, "Fabrication and application of electrically conducting composites for electromagnetic interference shielding of remotely piloted aircraft systems," *Compos. Struct.*, vol. 232, p. 111498, 2020.

[173] E. Roduner, "Size matters: why nanomaterials are different," *Chem. Soc. Rev.*, vol. 35, no. 7, pp. 583–592, 2006.

PUBLICATIONS FROM THE THESIS

Conference Papers

1. H. Yildirim Kalyon, S. Gördük, M. Gençten, and Y. Şahin, "Production of composite electrodes containing carbon materials and coordination complex for supercapacitors applications," in Proc. 3rd National Carbon Conf., Carbon Association, 2021
2. H. Yildirim Kalyon, "Production of composite materials containing poly(aniline-co-pyrrole) and metal oxide and investigation of supercapacitor properties," in Proc. 34th National Chemistry Congr., Yalova, 2022.
3. Y. F. Karasan and H. Yildirim Kalyon, "Electrochemical production of cerium doped PANI and investigation of its supercapacitive properties," in Proc. 34th National Chemistry Congr., Yalova, 2022.
4. O. Yılmaz and H. Yildirim Kalyon, "Electrochemical production of PANI with phosphorus containing additives and electrochemical properties," in Proc. 34th National Chemistry Congr., Yalova, 2022.
5. H. Yildirim Kalyon, S. Gördük, M. Gençten, and Y. Şahin, "Metal organic frameworks with ethylenediamine additives for electrochemical supercapacitors," in Proc. 4th National Carbon Conf., Sabanci University, 2024.

Papers

1. H. Yildirim. Kalyon, M. Gençten, S. Gördük, and Y. Şahin, "Novel composite materials consisting of polypyrrole and metal organic frameworks for supercapacitor applications," J. Electrochem. Soc., vol. 2021, no. 103699, 2021.
2. T. Basılı, H. Yildirim Kalyon, M. Macıt, M. Gençten, and Y. Şahin, "High-performance supercapacitive behaviors of oximes in a poly(aniline-co-pyrrole) based conducting polymer structure," New J. Chem., vol. 47, pp. 691–707, 2023.
3. O. Yılmaz, H. Yildirim Kalyon, and M. Gençten, "One-step production of phosphorene from red phosphorus and investigation of their supercapacitor

applications with conducting polymers," J. Energy Storage, vol. 79, 2024, Art. no. 11013.

4. H. Yildirim Kalyon, O. Yılmaz, M. Gençten, and Y. Şahin, "Ethylenediamine-functionalized metal organic frameworks for applications of electrochemical supercapacitors as an additive," Synth. Met., vol. 306, 2024, Art. no. 117627.

Projects

1. Scientific Research Project Researcher: “Production of Composite Electrodes Containing Coordination Compound and Conductive Polymer and Supercapacitor Applications” Higher Education Institutions Supported Project, 2021.
2. Scientific Research Project Researcher: “Production of Sulfur Doped Graphene-Molybdenum Disulfide Powders and Investigation of Their Use as Li-Ion Battery Anode Material” TÜBİTAK 3501 Career Development Fund (123M274).
3. Yildiz Technical University Scientific Research Council (BAP) for FBA-2021-4125.
4. Yildiz Technical University Scientific Research Council (BAP) for FDK-2023-5233 Doctoral Project code.

Awards

1. Higher Education Institution Priority Areas Scholarship: Energy Storage Critical Area, 2020.-2025.
2. Scientific and Technological Research Council of Turkey (TUBITAK) 2211-C National PhD Scholarship Program in the Priority Fields in Science and Technology. 2021-2024
3. TUBITAK 2224-B - Grant Program for Participation in Scientific Meetings within the Country, 2023.
4. TUBITAK 2214-A International Research Programme Scholarship: Warwick University, UK. 2022-2023.
5. TUBITAK 2250 - Performance-Based Scholarships Programme for PhD and Post-Doc Scholars, 2024.